A GENERALIZED PHASE-FIELD APPROACH FOR THE FAILURE OF
RUBBER-LIKE MATERIALS

A THESIS SUBMITTED TO
THE GRADUATE SCHOOL OF NATURAL AND APPLIED SCIENCES
OF
MIDDLE EAST TECHNICAL UNIVERSITY

BY

KEMAL AÇIKGÖZ

IN PARTIAL FULFILLMENT OF THE REQUIREMENTS
FOR
THE DEGREE OF DOCTOR OF PHILOSOPHY
IN
MECHANICAL ENGINEERING

FEBRUARY 2023

Approval of the thesis:

A GENERALIZED PHASE-FIELD APPROACH FOR THE FAILURE OF RUBBER-LIKE MATERIALS

submitted by **KEMAL AÇIKGÖZ** in partial fulfillment of the requirements for the degree of **Doctor of Philosophy in Mechanical Engineering Department, Middle East Technical University** by,

Prof. Dr. Halil Kalıpçılar
Dean, Graduate School of **Natural and Applied Sciences**

Prof. Dr. M. A. Sahir Arıkan
Head of Department, **Mechanical Engineering**

Assoc. Prof. Dr. Hüsnü Dal
Supervisor, **Mechanical Engineering, METU**

Examining Committee Members:

Prof. Dr. Suha Oral
Mechanical Engineering, METU

Assoc. Prof. Dr. Hüsnü Dal
Mechanical Engineering, METU

Assoc. Prof. Dr. Cihan Tekoğlu
Mechanical Engineering, TOBB-ETU

Prof. Dr. Recep Güneş
Mechanical Engineering, Erciyes University

Assoc. Prof. Dr. Sezer Özerinç
Mechanical Engineering, METU

Date:

I hereby declare that all information in this document has been obtained and presented in accordance with academic rules and ethical conduct. I also declare that, as required by these rules and conduct, I have fully cited and referenced all material and results that are not original to this work.

Name, Surname: Kemal Açıkgöz

Signature   :

ABSTRACT

**A GENERALIZED PHASE-FIELD APPROACH FOR THE FAILURE OF
RUBBER-LIKE MATERIALS**

Açıkgöz, Kemal

Ph.D., Department of Mechanical Engineering

Supervisor: Assoc. Prof. Dr. Hüsnü Dal

February 2023, 128 pages

Dilatational failure in terms of cavity formation and distortional failure guided by shear-type deformations are the two main failure modes of rubbery polymers. These modes correspond to deformations associated with the energetic/volumetric and entropic/shear responses under general loading conditions. This work proposes an energy-based failure criterion with a unique split of the free-energy function in terms of the first three invariants. Such an ansatz allows various failure modes under volumetric and shear deformations. The baseline hyperelasticity is described by the extended eight-chain model. As a novel aspect, we introduce distinct degradation mechanisms for shear and dilatational deformations that account for the transition from quasi-incompressible hyperelastic behavior to a porous compressible solid state prior to macro-crack formation. Herein, separate forms of a tunable Hermitian polynomial-based degradation function are applied to the free energy function's dilatational and distortional parts. The tunable nature of the Hermitian polynomials allow adjustment of the degradation of each term separately. Utilizing two distinct degradation functions for the volumetric and the entropic parts, the proposed generalized phase-field approach is shown to allow such transition and the degradation of the Poisson's ratio

is captured. Furthermore, the proposed degradation function recovers the quadratic, cubic, and quadric degradation functions from the literature as its special cases. The aspects of the proposed energetic failure surface are discussed, and its predictive capability is demonstrated by comparing it to existing data from the literature. Apart from separate degradations of the volumetric and entropic parts, a finitely nonlinear viscoelastic theory is utilized to investigate the rate effects to the fracture. An adjustable contribution of the viscoelastic part to the history field is adopted. Finally, experimental investigations are performed on unfilled styrene-butadiene rubber to obtain the base material response, rate effects, and fracture behavior. The fracture behavior is investigated with special v-shape notched specimens. Various boundary value problems are solved and the results are compared to the experiments.

Keywords: phase-field fracture, distortional and dilatational failure, rate effects on the fracture, multi-axial failure surface for rubber-like materials

ÖZ

KAUÇUK TİPİ MALZEMELERİN HASARINDA GENELLEŞTİRİLMİŞ FAZ-ALANI YAKLAŞIMI

Açıkgöz, Kemal

Doktora, Makina Mühendisliği Bölümü

Tez Yöneticisi: Doç. Dr. Hüsnü Dal

Şubat 2023 , 128 sayfa

Kavite oluşumuna dayalı hacimsel hasar ve kesme gerilmeleri sebebiyle oluşan şekil değiştirme tipi hasar kauçuk tipi polimerler için ana hasar mekanizmalarıdır. Genel yükleme koşullarında bu hasar modları enerjisel/hacim ve entropik/kesme davranışları ile ilişkilidir. Bu çalışma ilk üç invaryantla ilişkilendirilebilir şekilde ayrılmış serbest-enerji fonksiyonu kullanarak enerji-tabanlı bir dayanım kriteri sunmaktadır. Bu serbest enerji fonksiyonu ayrıştırma şekli hacimsel ve kesme tipi deformasyonlarda farklı hasar modlarına izin vermektedir. Burada, temel hiperelastik/mekanik davranış için genişletilmiş sekiz zincir modeli kullanılmıştır. Özgün katkı olarak, bu çalışmada kesme ve hacimsel deformasyonlar için farklı bozunum fonksiyonları kullanılmış olup, bu sayede çatlak oluşumu öncesinde sıkıştırılamaz hiperelastik davranıştan boşluklu sıkıştırılabilir katı davranışına geçiş sağlanmıştır. Burada, ayarlanabilir Hermitsel polinom tabanlı bozunum fonksiyonları türetilmiş olup serbest enerji fonksiyonunun hacimsel ve entropik kısımlarına uygulanmıştır, böylelikle önerilen genelleştirilmiş faz-alanı yaklaşımı Poisson oranının bozunumunu yakalayabilmektedir. Dahası, Hermitsel bozunum fonksiyonu literatürde geçen ikinci derece-

den, üçüncü dereceden ve dördüncü dereceden bozunum fonksiyonlarına özel durum olarak indirgenebilmektedir. Önerilen enerjisel ve entropik hasar yüzeyi incelenmiş olup, literatürde varolan verilerle kıyaslanarak modelin tahmin özellikleri irdelenmiştir. Ayrı bozunum fonksiyonlarının dışında, sonlu ve doğrusal olmayan bir viskoelastik model kurama entegre edilmiş ve hızın yırtılmaya olan etkisi incelenmiştir. Burada faz-alanının deformasyon geçmişine bağlı fonksiyonuna viskoz branşların elastik kısmı ayarlanabilir bir şekilde eklenmiştir. Son olarak, dolgusuz styrene-butadiene kauçuk için baz malzeme ve yırtılma davranışını elde etmek adına deneyler yapılmıştır. Farklı sınır değer problemleri çözülerek deneylerle kıyaslanmıştır.

Anahtar Kelimeler: faz-alanı yırtılma modeli, hacimsel ve şekil değiştirme tipi hasar, yırtılmada hız etkileri, kauçuk tipi malzemeler için çok eksenli hasar yüzeyi

I dedicate my dissertation work to my wife and parents, then specially to my newborn daughter Azra Zümra; may she have a beautiful life.

ACKNOWLEDGMENTS

TABLE OF CONTENTS

LIST OF TABLES

LIST OF FIGURES

FIGURES

xxii

LIST OF ABBREVIATIONS

Multi-word terms:

SBR	Styrene-butadiene rubber
NBR	Nitrile-butadiene rubber
UT	Uniaxial tension
ET	Equibiaxial tension
PS	Pure shear
BT	Biaxial tension
PT	Pancake tension
VC	Volumetric compression
SENT	Single edge straight notched tensile fracture test specimen
DENT	Double edge straight notched tensile fracture test specimen
vDENT	V-shape double edge notched fracture test specimen
DIC	Digital image correlation
PBP	Podgorski-Bigoni-Piccolroaz failure surface
Fig.	Figure

Operators:

$\text{Arg}[\bullet]$	Argument of a function
$\text{cof}[\bullet]$	Cofactor
$\text{det}[\bullet]$	Determinant
$\text{div}[\bullet]$	Divergence operator in Eulerian coordinates
$\text{Div}[\bullet]$	Divergence operator in Lagrangian coordinates
$\text{grad}[\bullet]$	Gradient operator in Eulerian coordinates
$\text{Grad}[\bullet]$	Gradient operator in Lagrangian coordinates

$\nabla_{\boldsymbol{x}}[\bullet]$	Gradient operator in Eulerian coordinates
$\nabla_{\boldsymbol{X}}[\bullet]$	Gradient operator in Lagrangian coordinates
$\Delta[\bullet]$	Laplacian
$\inf[\bullet]$	Infinum over a set
$\sup[\bullet]$	Supremum over a set
$\text{sym}[\bullet]$	Symmetric part of a tensor
$\text{skew}[\bullet]$	Skew part of a tensor
$\text{tr}[\bullet]$	Trace of a tensor
$[\bullet]^T$	Transpose operator
$[\bullet]^{-1}$	Inverse operator
$\mathcal{L}(\bullet)$	Lie derivative
$\delta_{[\bullet]}$	Variation with respect to $\bullet$
$\partial_{[\bullet]}$	Partial derivative with respect to $\bullet$
$\boldsymbol{\chi}^*[\bullet]$	Pull-back operator
$\boldsymbol{\chi}_*[\bullet]$	Push-forward operator
$\cdot$	Dot product
$:$	Double contraction
$\times$	Cross product
$\otimes$	Dyadic product

Continuum mechanics, and viscoelasticity:

$\mathcal{B}$	Denotes the body
$\partial\mathcal{B}$	Denotes the boundary of the body
$\mathcal{P}$	Particle $\mathcal{P}$ in body $\mathcal{B}$
$\{\boldsymbol{e}_1, \boldsymbol{e}_2, \boldsymbol{e}_3\}$	Reference frame for spatial coordinates
$\{\boldsymbol{E}_1, \boldsymbol{E}_2, \boldsymbol{E}_3\}$	Reference frame for material coordinates
χ_0	Reference configuration

χ_t	A configuration at time t
$\boldsymbol{X}$	Coordinates of a point in material representation
$\boldsymbol{x}$	Coordinates of a point in spatial representation
$\boldsymbol{\chi}$	Motion
$\boldsymbol{U}$	Displacement vector in material representation
$\boldsymbol{u}$	Displacement vector in spatial representation
$\boldsymbol{V}$	Velocity vector in material representation
$\boldsymbol{v}$	Velocity vector in spatial representation
$\boldsymbol{A}$	Acceleration vector in material representation
$\boldsymbol{a}$	Acceleration vector in spatial representation
$\dot{\overline{[\bullet]}}$	Material time derivative of $[\bullet]$
$\frac{D[\bullet]}{Dt}$	Another representation of material time derivative
$\boldsymbol{F}$	Deformation gradient
$\boldsymbol{R}$	Deformation gradient
$\boldsymbol{U}$	Right stretch tensor
$\boldsymbol{v}$	Left stretch tensor
J	Determinant of deformation gradient
$d\boldsymbol{X}$	Lagrangian infinitesimal line element
$d\boldsymbol{x}$	Eulerian infinitesimal line element
$d\boldsymbol{S}$	Lagrangian infinitesimal area element
$d\boldsymbol{s}$	Eulerian infinitesimal area element
dV	Lagrangian infinitesimal volume element
dv	Eulerian infinitesimal volume element
λ_a	Principle stretches
$\boldsymbol{N}_a$	Eigenvectors in Lagrangian coordinates
$\boldsymbol{n}_a$	Eigenvectors in Eulerian coordinates
$\boldsymbol{C}$	Right Cauchy-Green tensor

$\boldsymbol{b}$	Left Cauchy-Green tensor (or Finger tensor)
I_a	Principal invariants (of $\boldsymbol{C}$ or $\boldsymbol{b}$)
$\boldsymbol{l}$	Spatial velocity gradient
$\dot{\boldsymbol{F}}$	Material velocity gradient
$\boldsymbol{d}$	Rate of deformation tensor
$\boldsymbol{w}$	Spin tensor
$(\bullet)^\flat$	A covariant object
$(\bullet)^\sharp$	A contravariant object
$\mathcal{S}$	A cut region
$\partial\mathcal{S}$	Boundary of a cut region
$\boldsymbol{t}(\boldsymbol{x},\boldsymbol{n})$	Traction vector at $\boldsymbol{x}$ with normal $\boldsymbol{n}$
$\boldsymbol{\sigma}$	Cauchy stress tensor
$\tilde{\boldsymbol{P}}$	First Piola-Kirchhoff stress tensor
$\boldsymbol{\tau}$	Kirchhoff stress tensor
$\boldsymbol{S}$	Symmetric second Piola-Kirchhoff stress tensor
M	Total mass of a closed system
dm	Infinitesimal mass
ρ_0	Referencial mass density
ρ	Spatial mass density
$\mathcal{I}$	Linear momentum vector
$\mathcal{D}_\mathcal{O}$	Angular momentum vector about $\mathcal{O}$
$h(\boldsymbol{x},t;\boldsymbol{n})$	Heat flux on $\boldsymbol{x}$ at t with normal $\boldsymbol{n}$
$q(\boldsymbol{x},t)$	Heat flux vector in Eulerian coordinates
$\boldsymbol{Q}$	Heat flux vector in Lagrangian coordinates
$\mathcal{T}$	Total energy
$\mathcal{K}$	Kinetic energy
$\mathcal{E}$	Internal energy

$\mathcal{P}$	External mechanical power
$\mathcal{Q}$	External thermal power
$e(\boldsymbol{x}, t)$	Internal energy density per unit volume
$e_0(\boldsymbol{X})$	Internal energy density per unit volume in material representation
$r(\boldsymbol{x}, t)$	Internal heat source in spatial representation
$r_0(\boldsymbol{X})$	Material representation of internal heat source
$\mathfrak{S}$	Entropy production
S	Total entropy of a system
H	Quantity of heat per unit temperature
γ	Local entropy production per unit current volume
γ	Local entropy production per unit referencial volume
η	Local entropy per unit current volume
η_0	Local entropy per unit referencial volume
θ	Temperature in Kelvin
Ψ	Helmholtz free energy
$\boldsymbol{F}^e$	Elastic part of the deformation gradient
$\boldsymbol{F}^v$	Viscous part of the deformation gradient
$\boldsymbol{C}^e$	Elastic right Cauchy-Green tensor
$\boldsymbol{C}^e$	Viscous right Cauchy-Green tensor
$\boldsymbol{c}^e$	Inverse elastic right Cauchy-Green tensor
$\boldsymbol{g}$	Eulerian metric tensor
$\boldsymbol{G}$	Lagrangian metric tensor
$\tilde{\boldsymbol{G}}$	Lagrangian metric tensor for intermediate configuration
$\boldsymbol{l}^e$	Elastic spatial velocity gradient
$\boldsymbol{l}^v$	Viscous spatial velocity gradient
$\tilde{\boldsymbol{l}}^v$	Viscous part of the spatial velocity gradient when $\boldsymbol{l}$ additively split

$\boldsymbol{d}^e$	Elastic rate of deformation tensor
$\tilde{\boldsymbol{d}}^v$	Viscous part of the rate of deformation tensor when $\boldsymbol{d}$ additively split
$\boldsymbol{F}_k^e$	Elastic part of deformation gradient for k^{th} Maxwell branch
$\boldsymbol{F}_k^v$	Viscous part of deformation gradient for k^{th} Maxwell branch
$\boldsymbol{\tau}^e$	Equilibrium part Kirchhoff stress
$\boldsymbol{\tau}^{ne}$	Non-equilibrium part Kirchhoff stress
$\boldsymbol{S}^e$	Equilibrium part second Piola-Kirchhoff stress
$\boldsymbol{S}^{ne}$	Non-equilibrium part second Piola-Kirchoff stress
μ	Shear modulus
N	Number of segments
μ_c	Tube constraint part shear modulus
κ	Bulk modulus
χ	First Lame constant
$\mathcal{L}^{-1}(\bullet)$	Inverse Langevin function
λ_n	Network stretch
λ_r	Relative network stretch
ν_n	Network aerial contraction
μ^v	Shear modulus for a viscous branch
N^v	Number of segments for a viscous branch
χ	1st Lame constant for a viscous branch
κ	Bulk modulus for a viscous branch
$\dot{\gamma}_0$	Creep rate constant for a viscous branch
τ^{ne}	Norm of the non-equilibrium Kirchhoff stress
$\hat{\tau}$	Normalization for dimensionless ratio $\frac{\tau^{ne}}{\hat{\tau}}$
$\dot{\gamma}$	Effective creep rate function
λ_n^e	Network stretch elastic part

m	Energy activation exponent
$\mathbb{C}^e$	Equilibrium part of the tangent modulus
$\mathbb{C}^{ne}$	Non-equilibrium part of the tangent modulus
$\mathbb{C}^{ne}_{algo}$	Algorithmic non-equilibrium moduli

Generalized phase-field approach:

d	Crack phase field
$\mathcal{G}_c$	Critical fracture energy (Griffith-type critical energy release rate)
Γ	Sharp crack surface topology
Γ_l	Regularized crack surface topology
$\gamma(d, \nabla d)$	Isotropic crack surface density function
l	Length-scale parameter
$g_v(d)$	Volumetric degradation function
$g_f(d)$	Entropic free-chain part degradation function
$g_c(d)$	Entropic constraint part degradation function
k	Artificial stiffness parameter for stability
η	Viscous over-force for the evolution of $dotd$
$\psi_0(\boldsymbol{F})$	Reference energy
ψ^v_{cr}	Volumetric critical energy per unit volume
ψ^f_{cr}	Free-chain critical energy per unit volume
ψ^c_{cr}	Constraint part critical energy per unit volume
$\overline{\mathcal{H}}_v$	History field for volumetric deformations (volumetric crack driving force)
$\overline{\mathcal{H}}_f$	History field for free-chain part related deformations (free-chain part's crack driving force)
$\overline{\mathcal{H}}_c$	History field for constraint part related deformations (constraint part's crack driving force)

$\overline{\mathcal{H}}_e$	History field for entropic deformations (entropic part's crack driving force)
α_c	Constraint critical energy ratio
ε_i	Logarithmic principal strains where $i = 1, 2, 3$
ξ_i	Modified logarithmic principal strains where $i = 1, 2, 3$
ρ	Radius of a deformation point on Π_0 plane in Haigh-Westegaard coordinates
θ	Angular coordinate of a deformation on Π_0 plane in Haigh-Westegaard coordinates
$\boldsymbol{H}$	Hencky strain tensor
$I_{1,\boldsymbol{H}}$	1st principal invariant of Hencky tensor
$I_{2,\boldsymbol{H}}$	2nd principal invariant of Hencky tensor
$I_{3,\boldsymbol{H}}$	3rd principal invariant of Hencky tensor

CHAPTER 1

INTRODUCTION, MOTIVATION, AND SCOPE

Hyperelasticity and viscoelasticity: Rubberlike materials exhibit strong rate dependent response that earns rubber excellent mechanical properties highly sought in applications such as automotive, aerospace and soft robotics, just to name but a few. Viscoelasticity improves the fracture toughness and energy absorption capacity rendering rubber very suitable as shock absorbers and vibration decouplers. The backbone of finite viscoelastictiy of rubberlike materials is an accurate description of ground state equilibrium elastic response. In this context, the hyperelastic constitutive models for rubber can either be represented by (i) phenomenological, or (ii) micromechanically based free energy functions. The *phenomenological models* are based on invariant or principal stretch-based expressions for the free energy function that successfully fit the experimental stress-strain curves. The invariant based models usually consist of polynomial combinations [1, 2, 3, 4] or more sophisticated mathematical functionals [5, 6, 7, 8, 9, 10, 11, 12, 13, 14] of the first and second invariants of the right/left Cauchy-Green deformation tensor. Various functional forms of free energy have been proposed in terms of principal stretches e.g. [15, 16, 17, 18, 19, 20, 21]. Some material models have a mixed mathematical representation in terms of principal stretches and invariants e.g. [22, 23]. *Micromechanical models*, on the other hand, are physically-based models, considering the material microstructure by linking the macroscopic mechanical behaviour to molecular structure of rubberlike materials through statistical mechanics. Herein, the force-displacement relation of a single free-chain is obtained from a distribution function for the end-to-end distance of the chain by making use of the concept of *entropic elasticity*. In this context, a Gaussian distribution function for a free chain with infinite length was derived by KUHN [24, 25]. MOONEY [2] investigated the form of free energy function in a purely math-

1

ematical context applicable for ideal rubber behaviour. Later on TRELOAR [1], using the WALL's assumptions [26], and following Kuhn and Grün's and Mooney's form, derived the neo-Hooke model. Note that neo-Hooke model is the simplest constitutive model that extends the concept of linear elasticity to the geometrically nonlinear setting. Gaussian distribution, lacks the ability to predict stress-strain behaviour at large deformations, especially around the chain extensibility limit [27]. In order to circumvent these drawbacks, non-Gaussian distribution functions based on Langevin statistics are utilized in the sense of KUHN AND GRÜN [28]. Within this context, WANG & GUTH [29] proposed the three-chain model, FLORY & REHNER [30] the four-chain model, TRELOAR & RIDING [31] the full network model and ARRUDA & BOYCE [32] the eight-chain model. All these models make use of a fixed relation between micro-scale and macro-scale deformations. MIEHE ET AL. [33] proposed the non-affine micro-sphere model which extends the full-network model of TRELOAR & RIDING [31] by introducing a non-affine average network stretch and an additional tube-constraint which accounts for the topological constraints. The notion of tube model or tube-constraints is based on the fact that polymer chains are not free. In three dimensional network chains not lying in the same plane causes topological constraints on one another. For this reason, the network models that rely on the free motion of the chains usually underestimate the stress response under biaxial deformation upto moderately large stretches. The tube and the extended tube model of KALISKE & HEINRICH [22, 23, 34], the constraint-junction model of FLORY & ERMAN [35, 36] and the non-affine micro-sphere model of MIEHE ET AL. [33] take into account the topological constraints on the free motion of the polymer chains by introducing a tube-like constraint. For an extensive overview of the aforementioned models, we refer to the review papers [37, 38, 39, 40]. The micro-sphere model shows an excellent fitting performance to uniaxial and (equi)biaxial tests. However, its computational cost is considerably higher than classical invariant-based formulations. The eight-chain model succesfully captures the uniaxial tensile behavior but it lacks the ability of simultanous fitting of uniaxial and (equi)biaxial tests. It is a common practive to improve the biaxial performance of the first invariant based models by incorporation of a second invariant term [41]. In this respect, micromechanically motivated models based on the first invariant can be either improved by a second invariant based term [34] or a principal stretch based term [42, 23, 12]. The extended

2

tube model of KALISKE & HEINRICH [23] and the review paper of BOYCE & AR-RUDA [40] utilize a principle stretch based expression as a tube constraint, where the former uses a Ogden-type term with negative power and the latter uses a constraint term proposed by FLORY & ERMAN [36]. Moreover, the second invariant based models lack the convenient functional form. A rigorous analysis which establishes the relation between the tube-constraints and the second invariant has not been treated in the literature yet. In order to resolve this issue, in this contribution, we propose an extended eight-chain model by reinforcing the free energy function in terms of a tube constraint part. *Within this context, micro-macro transition between the micro-kinematic tube constraint and the second invariant is established and a simple yet instrumental second invariant based term for the free energy function, which significantly improves the biaxial response of the eight-chain model, is derived [43].*

Experimental investigations of viscoelasticity in rubberlike materials are reported in, e.g., references [44, 45, 46, 47]. The fundamentals of linear and nonlinear viscoelasticity theory of polymers are reviewed in, e.g., [48, 49]. The early treatment of rubber viscoelasticity is based on the *finite linear viscoelasticity* of COLEMAN AND NOLL [50] as an extension of *linear viscoelasticity*. Most theories of finite viscoelasticity exploit the general axiom of *a fading memory* introduced by COLEMAN [51], see also TRUESDELL & NOLL [52]. Recent models of finite linear viscoelasticity use a stress-type internal variables [45, 53, 54, 55]. For an excellent review, we refer to HAUPT & LION [56] and MIEHE AND GÖKTEPE [47]. Internal variable type formulations of finite viscoelasticity based on the multiplicative decomposition of deformation gradient are outlined in [57, 58, 59, 60, 61]. An alternative kinematic representation of finite viscoelasticity based on a Lagrangian viscous metric tensor is proposed by MIEHE AND KECK [46]. The algorithmic implementation of internal variable type formulations of finite viscoelasticity is shown in REESE AND GOVINDJEE [60] and DAL & KALISKE [62] in the sense of SIMO & MIEHE [63] (for finite elastoplasticity) and SIMO [64] (for viscoplasticity). Therein, a predictor-corrector algorithm along with exponential mapping is employed for the integration and solution of the evolution equation in a time-discrete setting, see [65, 66]. These approaches use the unconditionally stable backward Euler scheme for the integration of the evolution equation in a time-discrete setting. EIDEL ET AL. [67] reported a considerable speed

up in convergence by replacing backward Euler integration scheme with higher order Runge-Kutta methods. Another approach for finite viscoelasticity of rubberlike materials is the utilization of the micro-sphere kinematics where the three-dimensional viscoelasticity is obtained by integration of one-dimensional rheological constructions via numerical quadrature over unit sphere. Within this context, MIEHE & GÖKTEPE [47] proposed a finite viscoelasticity model depending on two micro-kinematic scalar internal variables on discrete space orientations of the micro-sphere. In fact, two micro-mechanisms for the relaxation process of polymer chains are introduced: The relaxation of superimposed entanglements and the release of topological constraints are taken into account by a spectrum of nonlinear evolution laws in the logarithmic space of the discrete space orientations. Extension of this approach to the viscoplastic response of uncured green rubber is achieved by DAL ET AL. [68].

Two molecular approaches for the description of the time-dependent behavior of polymer chains exist. *Transient network theory* explains the stress relaxation phenomenon as a consequence of breakage and reformation of the cross-links continuously. The theory was firstly proposed by GREEN & TOBOLSKY [69] and further developed by LODGE [70], PHAN-THIEN [71] and TANAKA AND EDWARDS [72, 73]. This approach was also adopted to the microsphere model by LINDER ET AL. [74]. *Reptation-type tube models* were developed for the definition of the motion of a single chain in a polymer gel. The constraints on the free motion of a single chain are qualitatively modeled as a tube-like constraint and the motion of the chain is described as a combination of Brownian motion within and reptational motion along the tube. The model is proposed by DE GENNES [75] and DOI & EDWARDS [76]. The reptational motion is successfully adopted to finite viscoelasticity by BERGSTRÖM & BOYCE [59]. Two drawbacks of their approach can be observed in the evolution equation. That is, the creep rate function $\dot{\gamma}$ is singular at the onset of loading leading to an initial asymptotic behavior in the relaxation curves which is not a characteristic behavior of the rubberlike viscoelastic behavior. Incorporation of a perturbation parameter to the kinetic term helps to overcome the singularity in the evolution law. However, the model becomes very sensitive to the perturbation parameter leading to an extra material parameter in the evolution equation. Moreover, incorporation of a fictitious viscous network stretch λ_n^i to the evolution equation is not physically conceivable and

4

causes problems in the derivation of the consistent tangent necessary for the finite element implementation. Recently, a rate and amplitude dependent finite viscoelastic model based on the *dynamic flocculation model* for filled rubber has been proposed by RAGHUNATH ET AL. [77].

Historical remarks, path to phase-field approach, and the state of the art: The design and reliability of rubber components heavily depend on the prediction of failure in such materials. The crack initiation as well as propagation have to be incorporated as computational models into the design process. The historical development of the classical treatment of brittle fracture starts with the works of GRIFFITH [78] and IRWIN [79]. The kickstarting idea was to define a crack propagation criterion based on the energy release rate. That is, the decrease of the potential energy has to be spent on the formation of new crack surfaces, linking the existence of cracks to surface energy. Later on, the theory has been solidified by LIEBOWITZ AND SIH [80]. This particular approach fails to determine curvilinear crack paths, angles of crack branching, and other complex propogation patterns. Especially, the idea has a dramatic failure on predicting the crack initiation. There has to be an already present crack for this approach to work [81, 82]. The field of fracture mechanics later on flourished and literature expanded exponentially. During the late 90s, a variational take on of the problem has been studied by FRANCFORT AND MARIGO [83] to mitigate the shortcomings of the classical theory. This idea, based on the energy minimization, effectively allows prediction of crack initiation. Following Γ-convergence argument for a free discontinuity problem in image segmentation context from MUMFORD & SHAH [84], BOURDIN ET AL. [85, 86] came up with a regularization for the variational approach of [83]. The resulting regularization diffuses the sharp crack topologies with the use of an auxiliary variable. This variable can be termed phase-field, takes on continuous values within $[0, 1]$ range, and describes a state of fracture between the fully intact to fully broken ranges. Later on MIEHE ET AL. [81] casted this approach to a thermodynamically consistent framework, and presented a two-field (rate-independent) and three-field (rate-dependent with an additional dual driving force field) implementations that take only the tensile part of the energies to drive the crack. The resulting field equations ushered a new era in fracture mechanics where the phase-field approach becomes a solid alternative path. Furthermore, MIEHE ET

AL. [87] implemented an operator-split based staggered algorithm with an additional field, coined as history field. It provides a compact staggered scheme for modular applications as we also pursued in this study. The advantage of the phase-field approach is its obvious circumvention of the necessity to track the newly formed crack surfaces. Instead of dealing with sharp crack discontinuities, phase-field approach casts everything into continuously defined field PDEs, which makes it extremely easy to implement in a finite element setting. It introduces a length-scale parameter reminiscent of the gradient-type materials or materials with microstructure, see [88]. Apart from the classical treatment of phase-field approach, the implementation for rubber-like materials came later by SCHÄNZEL ET AL. [89, 90], MIEHE & SCHÄNZEL [91], and SCHÄNZEL [92]. The mostly rate-independent theories so far provide a transition from classical treatment of fracture and the implementability of the phase-field approach. However, artificially viscous (or rate-dependent) settings also appear in [81, 89, 91, 90]. The introduced viscous regularizations merely provide numerical stability after crack initiation.

Rate-effects on fracture and rate-dependent theories regarding phase-field approach: Rubber-like materials are strongly rate-dependent in both their mechanical response and fracture properties. The most fundamental characteristics, relevant to the phase-field theory, is the fracture toughness or the critical energy release rate $\mathcal{G}_c$, as a material parameter. Therefore, one can, naturally, start with a phenomenological expression for a rate dependent critical energy release rate. In [93], YIN ET AL proposed a rate-dependent fracture toughness with a degradation characteristic given in the context of phase-field fracture in terms of small-strain rates. This is an excellent modification for the critical energy release rate $\mathcal{G}_c$ for varying strain-rates. However, the theory is in small-strains setting and focuses on the evolution of fracture. Resulting behavior observed on simulations where increased loads appears on fracture for simulated load-displacement curves. [93] attributed this to the difference in chain strength and strength of entanglements and cross-links. For the loads applied in high strain-rates, the relaxation kinetics transfers the loads towards equilibrium, however the chains' relaxation is not infinitely fast and the chains become the main carriers of the load, which require more energy to break. This theory does not require tracking the crack propagation velocity $\dot{a}$ (as in the case of [94]), since it utilizes a phase-

field framework. LOEW ET AL. [95] directly extended the numerical stabilization parameter (also present in our theory) of MIEHE & SCHAENZEL [96] and gave a viscoelastic response to the bulk, and obtained the first finite theory. The damage growth is regularized and a rate-dependent driving force expression is obtained. This theory incorporates the finite strains linearly viscous theory of HOLZAPFEL [97] and avoids local history field (of [81]) altoghether. With the history variable expression, they observed an unbounded growth of phase-field even though $\mathcal{H}$ stays constant. Therefore, they used an active set method to stop the growth of d. The provided experiments on EPDM rubber for SENT as well as DENT specimens validates their theory. Since the degradation functions are an integral part of the phase-field approach, they discussed the several known degradation functions and their effects as well. Also, the calibration of the phase-field length scale parameter l through DIC renders physically accurate results. In [98], YIN & KALISKE proposed another approach, where they tracked the intact total free energy consisting of the summation of equilibrium and non-equilibrium responses as the history variable in the phase-field expressions. Their viscoelastic expressions are based on REESE & GOVINDJEE's nonlinearly viscous theory [60], and utilize neo-Hookean Maxwell branches for equilibrium as well as non-equilibrium responses. This theory correctly captures the increase in reaction force at fracture on a load-displacement curve at increasing rates for the SENT (single edge notched) and DENT (double edge notched) experiments on EPDM rubber of LOEW ET AL. [95]. SHEN ET AL. [99] used another approach to take rate-dependent effects into the fracture process by incorporating a portion of the dissipated energy into the dissipation inequality expression and derived the rate-dependent PDEs of the multi-field problem. The amount of contribution is controlled with a parameter. The postulation regards the Fig. 1.1 as mental picture where an inner highly non-linear region (region III) and a mainly viscous driven dissipative region (region II) constitute the fracture process zone. In our work, the region III is also of main concern, where we obtained a degrading incompressibility of the bulk. However, SHEN ET AL. considered region II as the main effect that ties the phase-field fracture and viscous response at the bulk. Accordingly, this dissipative region is a source of self heating which promotes the nucleation as well as propagation (altering the evolution of crack growth rate) of fracture. Although the temperature increase is evident, a further study is needed to quantify this increase with a thermo-mechanical coupling in

the phase-field approach. Finally, note that the theory [99] is linear in elastic as well as viscous branches.
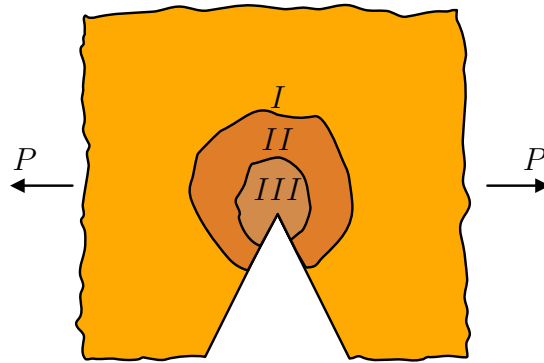
Figure 1.1: A representative schematic view of the process zone around the crack tip [99]. I denotes the uneffected (and undamaged) region, II represents the region where viscoelastic dissipative effects take place, finally, III shows the region where nonlinear inelastic and irreversible processes occur, these can be counted as cavity formation, bond or cross-link rupture.

Cavity formation, multi-axial failure surface for rubber-like materials, and the loss of incompressibility: GENT & LINDLEY [100]'s experiments on a pancake-type arrangement (also known as poker-chip experiments, see Fig. 1.2) showed rather unexpected behavior of rubber-like materials, where under sufficiently large volumetric tensile deformations *cavitation* occurs. This instability-like failure mode observed to be intrinsically tied to the shear modulus, where a critical load in pancake-type experiments appear to be a function of the shear modulus only. A new and elaborate analysis of GENT & LINDLEY [100]'s poker-chip experiments appear in the work of KUMAR & LOPEZ-PAMIES [101], where a careful discussion is put forth on whether it can be considered as an elastic-instability or a fracture process. The elastic-instability is mathematically shown to be the case by BALL [102] for the initiation of the *cavities*, whereas continuum damage based theories considered it as a fracture process [103, 104] and there appeared successful computational implementations for both initiation and growth, see DAL ET AL. [68]. Under multi-axial deformations, the failure surface for rubber-like materials must also predict the initiation of the cavities. This mode of failure is named as *dilatational* in this thesis. The failure mode related

to shear-type deformations is called *distortional*. The failure surfaces for solids are generalized over the years, phenomenologically, and there appears quite successful mathematical forms within this context. In metals and other energetic solids, stress-driven failure surfaces (see KOLUPAEV [105] for an excellent review) sufficely define the behavior. However, the rubber-like or other entropic materials favor energy based failure surfaces, see GÜLTEKIN ET AL. [106].
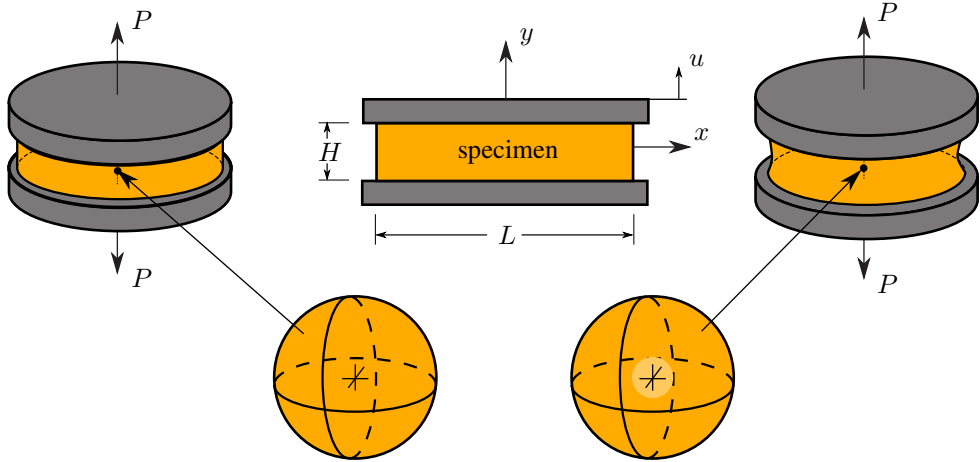
Figure 1.2: Poker-chip experiments (or pancake-type loading) of GENT & LINDLEY [100]. Due to the aspect ratio of the cylindrical specimen, the deformation in the load-application direction changes the volume of the cylinder, causing *cavitation*.

Within the context of multi-axial failure surfaces for rubber-like materials, ROSENDAHL ET AL. [107] recently put forward an equivalent strain based failure criterion. Within this excellent work, we can see direct equivalent-strain based counterparts of the classical equivalent-stress failure surface definitions, e.g., von-Mises, Tresca, and more advanced ones as in *Podgorski-Bigoni-Piccolroaz*. The idea of equivalent-strain based failure criterion allows the definition of complex failure criteria for rubber-like materials. On the other hand, direct energy based failure criterion (the energy-limiters approach) of VOLOKH [108], depending on the complexity of the underlying hyper-elastic model, could predict the failure under biaxial as well as the hydrostatic loads. However, this theory follows a separate path apart from phase-field approach for the failure. A separate considerations of free-chain response and the constraint response would allow prediction of biaxial failure more precisely. In this regard, the extended

eight-chain model of DAL ET AL. [43], can be considered superior as it micromechanically quantify free-chain, and constraint part responses, as functions of I_1, I_2. Therefore, we pursued a failure surface definition considering these separate terms in this thesis.

Motivation of the thesis and the problem definition: The understanding of the process zone for the fracture of rubber-like materials stands equally important to the metals. Albeit, a complete picture of the process zone is lacking, also the understanding of the formation and propagation of cracks in rubber-like materials stay incomplete. Much efforts have been devoted in literature to the separate investigations regarding hyperelasticity, finite viscoelasticity, fracture, and cavity formation throughout the years. Considering the current understanding of the process zone, depicted in Fig. 1.1, an experimentally evident (see LE CAM ET AL. [109]) phenomenon takes place, that yet to be modeled. This phenomenon can be described as follows. For the Mode-I type fracture depicted in Fig. 1.1, in region III, small cavities appear just before the propagation at the notch tip, or on the crack front. In Fig. 1.3, the process of formation of cavities and the onset of propagation of crack is portrayed. Note that, for all intensive purposes, rubbery materials are considered incompressible or at least quasi incompressible. However, this phenomenon suggests the loss of the incompressibility of the base rubber specimen. In this work, we tackled the problem of degradation of incompressibility and its adaptation within the phase-field fracture formulation. To this end, ANG ET AL. [110] and LI & BOUKLAS [111] proposed separate degradation of volumetric and isochoric parts in their associated element formulations for stability purposes. Here, in this thesis, the extended eight-chain model provides a stronger split called *the volumetric-entropic separation*, and its micro-mechanically motivated terms can be extended to provide a multi-axial failure surface as well as a physically motivated degradation of the incompressibility.

Furthermore, a lack of definitive micro-mechanically motivated multi-axial failure surface for rubber-like materials hinders painting a complete picture of fracture. Furthermore, regarding zone II in Fig. 1.1, rate effects are needed to be considered for a complete picture as well. In this context, incorporation of a finite viscoelasticity theory within the phase-field framework for the rate effects is still not mature in literature. In summary, a nonlinear inelastic (due to cavity formation at the crack tip),

10
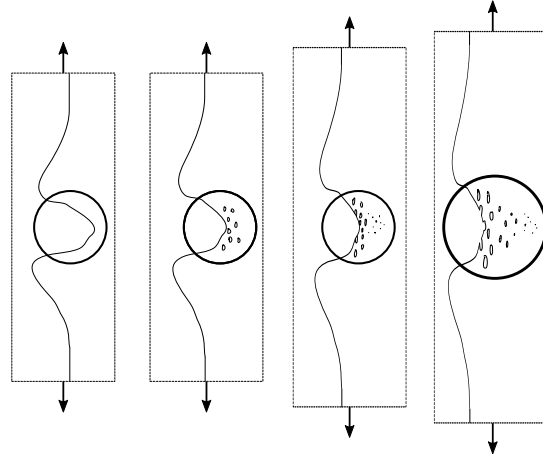
Figure 1.3: Snapshots of deformation around a notch tip (by LE CAM ET AL. [109]) portraying the formation of cavities as precursor to the propagation of cracks.

and the nonlinear rate-effects play crucial roles in the fracture process. The goals of the thesis are as follows,

- definition of a failure surface for rubber-like materials that can take into account (equi)biaxial or fully multi-axial loadings,

- derivation of a phase-field formulation that can presently allow multiple degradation functions for the modeling of the crack tip incompressibility loss,

- incorporation of a finite viscoelasticity theory with a nonlinear evolution law into the phase-field formalism,

- experimental validation of the theory.

Scope of the thesis: We have investigated the aforementioned aspects of failure in rubber-like materials. The ongoing state of mind during the development up to the finish of this work was to incorporate these aspects as consistently as possible. We restricted ourselves to single type of material, that is, the unfilled SBR, for experimental validation. The stochastic nature of the fracture of rubber-like materials is disregarded altogether to be able to confine ourselves to the investigation of the possibilities of the current study. In the results section, we restricted ourselves to entropic failure and kept the implied aspects of the volumetric failure to the future studies.

Outline of the thesis: The overall structure of the thesis is as follows: In Chapter 2 we expressed the prerequisites in terms of notation and theory, and briefly summarized the continuum mechanics. Next, a nonlinearly viscous theory based on the extended eight-chain model is introduced in Chapter 3. The multiphysics problem is described in Chapter 4, where the phase-field approach, tunable degradation functions based on Hermitian polynomials, and the degradation of incompressibility are formalized. Based on a special transformation, in Chapter 5, generalized phase-field model's implied failure criteria is investigated, comparison with equivalent strain failure criteria and experimental data is pursued. Next, in Chapter 6, the nonlinearly viscous theory is incorporated into the generalized phase-field formulation in a modular sense, its merits and comparison to literature are reported. Later on, the procedures and the results of the experimental work on unfilled SBR are given in Chapter 7. Finally, the results of the theory are presented on several boundary value problems in Chapter 8 and compared to both literature and in-house experimental work. Finally, the overall conclusions on this work are given in Chapter 9.

CHAPTER 2

FUNDAMENTALS OF CONTINUUM MECHANICS

In this chapter we briefly outline the continuum concepts and the notation related to this work. The finite deformation requires kinematical definitions of several deformation measures, such as the *right Cauchy-Green* tensor. The concept of stress and *Cauchy's stress theorem* then explained. Next, we discussed the principles of balance of mass, balance of linear and angular momentum, and balance of energy. The second law of thermodynamics, the *Clasius-Duhem inequality* and the concept of *Coleman-Noll procedure* are then explained. The chapter closes with a discussion of hyperelasticity and constitutive equations.

In this part, we kept the definitions as compact as possible, thus, of course we refer the interested reader to the monumental works of MARSDEN & HUGHES [112], MALVERN [113], TRUESDELL & NOLL [52], HAUPT [114], and HOLZAPFEL [115].

2.1 Kinematics

Let $\mathcal{B}$ denote a continuum body at time t with particles $\mathcal{P} \in \mathcal{B}$. Consider an Euclidean resolution of the coordinates of the particles, where a reference right-handed rectangular coordinate system at origin $\mathcal{O}$ with orthonormal basis vectors $\{e_a\} = \{e_1, e_2, e_3\}$ can be introduced. As the body moves across time, the occupied region in space changes. Let an occupied region of space at time t be called a configuration χ_t. The overall motion of the body defines a continuous set of configurations $\chi_0...\chi_t$. With this notion at hand, one can define χ_0 as an undeformed configuration at $t = 0$, or the reference configuration (it doesn't have to be undeformed). The configuration at $t = 0$ is called the initial configuration, and we assume reference and initial con-

figurations coincide. A point in the body $\mathcal{P} \in \mathcal{B}$ can be represented by $\boldsymbol{X}$ in the reference configuration. We can define a separate coordinate system for the reference configuration with bases $\{\boldsymbol{E}_A\}$, however, here, we take this coordinate system coincident with $\{\boldsymbol{e}_a\}$. A configuration at any time t other than $t = 0$, is called the current or deformed configuration. The position of the point $\mathcal{P}$ at t can be identified with $\boldsymbol{x}$. We refer the coordinates $\boldsymbol{X}$ and $\boldsymbol{x}$ as material (reference) and spatial (current) coordinates of the material particle $\mathcal{P}$. Let a one-to-one mapping of the particles to the coordinates in reference frame be denoted by $\boldsymbol{X} = \hat{\chi}(\mathcal{P})$. Furthermore, let $\boldsymbol{x} = \bar{\chi}(\mathcal{P}, t)$ denote a one-to-one mapping of particles to their position in the current configuration. Then, we can define

$$\boldsymbol{x} = \bar{\chi}\left[\hat{\chi}^{-1}(\boldsymbol{X}, t)\right] = \chi(\boldsymbol{X}, t) \tag{2.1}$$

where χ denotes the vector field for the motion of the body $\mathcal{B}$. Its inverse (the inverse motion) is assumed to be defined uniquely, $\boldsymbol{X} = \chi^{-1}(\boldsymbol{x}, t)$. Note that we adopt the Einsteins's summation convention, where a vector can be represented by $\boldsymbol{a} = a_i \boldsymbol{e}_i$ for $i = 1, 2, 3$. A second order tensor, then can be represented by $\boldsymbol{A} = A_{ij} \boldsymbol{e}_i \otimes \boldsymbol{e}_j$ for $i = \{1, 2, 3\}$ and $j = \{1, 2, 3\}$, where $\otimes$ is the dyadic product and A_{ij} are components of the tensor $\boldsymbol{A}$ in the right-handed orthonormal bases $\{\boldsymbol{e}_a\}$. We can denote $\boldsymbol{A}$ as A_{ij} in indicial notation, as shorthand. Next we outline some basic definitions,

displacement:

$$\boldsymbol{U}(\boldsymbol{X}, t) = \boldsymbol{x}(\boldsymbol{X}, t) - \boldsymbol{X} \quad \text{and} \quad \boldsymbol{u}(\boldsymbol{x}, t) = \boldsymbol{x} - \boldsymbol{X}(\boldsymbol{x}, t) \tag{2.2}$$

velocity:

$$\boldsymbol{V}(\boldsymbol{X}, t) = \partial_t \chi(\boldsymbol{X}, t) \quad \text{and} \quad \boldsymbol{v}(\boldsymbol{x}, t) = \boldsymbol{V}[\chi^{-1}(\boldsymbol{x}, t), t] \tag{2.3}$$

acceleration:

$$\boldsymbol{A}(\boldsymbol{X}, t) = \partial_t^2 \chi(\boldsymbol{X}, t) \quad \text{and} \quad \boldsymbol{a}(\boldsymbol{x}, t) = \boldsymbol{A}[\chi^{-1}(\boldsymbol{x}, t), t] \tag{2.4}$$

in material and spatial coordinates, respectively.

material and spatial derivatives: Material time derivative (or the *total derivative*) of a material field $W(\boldsymbol{X}, t)$, is the derivative of W with respect to time, keeping $\boldsymbol{X}$ constant. It is shown by $\dot{W}(\boldsymbol{X}, t) = D(W(\boldsymbol{X}, t)/Dt$. Similarly, the material time

14

derivative of a spatial field $w(\boldsymbol{x}, t)$ is the time derivative of w while keeping $\boldsymbol{X}$ fixed. It can be written as

$$\dot{w}(\boldsymbol{x}, t) = \frac{D(w(\boldsymbol{x}, t))}{Dt} = \frac{\partial w(\boldsymbol{x}, t)}{\partial t} + \text{grad}(w(\boldsymbol{x}, t)) \cdot \boldsymbol{v} \qquad (2.5)$$

where, $\text{grad}(\bullet) = \partial(\bullet)/\partial \boldsymbol{x}$ is the spatial gradient operator, the first part of the equation is the local time derivative of the spatial field w, while the second part is the *convective rate of change* of w.

deformation gradient: As the body $\mathcal{B}$ moves, the position of a particle $\mathcal{P} \in \mathcal{B}$ defines a trajectory. The tangent in material coordinates to this trajectory at any point define a local deformation measure, called the deformation gradient, which we intensely use, that is,

$$\boldsymbol{F}(\boldsymbol{X}, t) = \frac{\partial \boldsymbol{\chi}(\boldsymbol{X}, t)}{\partial \boldsymbol{X}} = \text{Grad}\, \boldsymbol{x}(\boldsymbol{X}, t) \qquad (2.6)$$

where $\text{Grad}(\bullet) = \partial(\bullet)/\partial \boldsymbol{X}$ is the material gradient operator. The deformation gradient defines a mapping between infinitesimal line elements $d\boldsymbol{X}$ and $d\boldsymbol{x}$. For the parameterization of the trajectories of the particles $\mathcal{P} \in \mathcal{B}$ and a more elaborate definition of the deformation gradient, see HAUPT [114] and HOLZAPFEL [115].

Nanson's formula, area map, and volume map: The volume map, between material volume (dV) and spatial volume (dv) elements can be defined as

$$dv = J dV \qquad (2.7)$$

where $J(\boldsymbol{X}, t) = \det \boldsymbol{F}(\boldsymbol{X}, t)$. Let the area $d\boldsymbol{S}$ in reference configuration with unit vector $\boldsymbol{N}$ be mapped to $d\boldsymbol{s}$ in current configuration with unit vector $\boldsymbol{n}$ during the motion. The infinitesimal volume element in current configuration can be written as,

$$dv = d\boldsymbol{s} \cdot d\boldsymbol{x} = J d\boldsymbol{S} \cdot d\boldsymbol{X} = J dV \qquad (2.8)$$

from where we can use $d\boldsymbol{x} = \boldsymbol{F} d\boldsymbol{X}$, and obtain,

$$d\boldsymbol{s} \cdot \boldsymbol{F} d\boldsymbol{X} = J d\boldsymbol{S} \cdot d\boldsymbol{X} \implies d\boldsymbol{s} = J \boldsymbol{F}^{-T} d\boldsymbol{S} \qquad (2.9)$$

which relates the vectorial areas $d\boldsymbol{S}$ and $d\boldsymbol{s}$. This relationship is known as *Nanson's formula*.

2.1.1 Deformation measures

Mapping a unit vector $\boldsymbol{A}$ in reference configuration to $\boldsymbol{a}$ in current configuration can be defined as

$$\boldsymbol{a} = \boldsymbol{F}\boldsymbol{A} \tag{2.10}$$

From this definition, we can define $\lambda = |\boldsymbol{a}|$ as the *stretch* of the vector $\boldsymbol{A}$ due to the deformation. Let us take the square of the stretch,

$$\lambda^2 = \boldsymbol{a} \cdot \boldsymbol{a} = \boldsymbol{F}\boldsymbol{A} \cdot \boldsymbol{F}\boldsymbol{A} = \boldsymbol{A} \cdot \boldsymbol{F}^T \boldsymbol{F}\boldsymbol{A} = \boldsymbol{A} \cdot \boldsymbol{C}\boldsymbol{A} \tag{2.11}$$

where $\boldsymbol{C} = \boldsymbol{F}^T \boldsymbol{F}$ is called the *right Cauchy-Green tensor*. It is a second order symmetric positive definite tensor and extremely common measure of deformation in material coordinates. Its counterpart in spatial coordinates, $\boldsymbol{b}$, is called the *Finger tensor* or the *left Cauchy-Green tensor*, comes from the definition of λ^{-2}, square of the inverse stretch, that is,

$$\lambda^{-2} = \boldsymbol{A} \cdot \boldsymbol{A} = \boldsymbol{F}^{-1}\boldsymbol{a} \cdot \boldsymbol{F}^{-1}\boldsymbol{a} = \boldsymbol{a} \cdot \boldsymbol{F}^{-T}\boldsymbol{F}^{-1}\boldsymbol{a} = \boldsymbol{a} \cdot \boldsymbol{b}^{-1}\boldsymbol{a}. \tag{2.12}$$

$\boldsymbol{b} = \boldsymbol{F}\boldsymbol{F}^T$ is also symmetric and positive definite. If no deformation occurs, we can see that $\boldsymbol{F} = \boldsymbol{I}$ implying $\boldsymbol{b} = \boldsymbol{I}$ and $\boldsymbol{C} = \boldsymbol{I}$, here $\boldsymbol{I} = \delta_{ij}\boldsymbol{e}_i \otimes \boldsymbol{e}_j$ is the second order identity tensor, with *Kronecker delta* $\delta_{ij} = 1$ for $i = j$ and $\delta_{ij} = 0$ for $i \neq j$.

rotation and stretch: The polar decomposition of the deformation gradient $\boldsymbol{F}$ reads

$$\boldsymbol{F} = \boldsymbol{R}\boldsymbol{U} = \boldsymbol{v}\boldsymbol{R}. \tag{2.13}$$

This relationship defines a decomposition of $\boldsymbol{F}$ into a pure rotation and pure stretch parts. $\boldsymbol{U}$ and $\boldsymbol{v}$ are right- and left-stretch tensors, respectively, and have the following properties,

$$\boldsymbol{U}^2 = \boldsymbol{U}\boldsymbol{U} = \boldsymbol{C}, \quad \text{and} \quad \boldsymbol{v}^2 = \boldsymbol{v}\boldsymbol{v} = \boldsymbol{b}. \tag{2.14}$$

The tensor $\boldsymbol{R}$ is a proper orthogonal tensor ($\det \boldsymbol{R} = 1$), and measures the local rotation. Furthermore, $\det \boldsymbol{U} = \det \boldsymbol{v} = J > 0$.

2.1.1.1 Spectral decomposition, eigenvalues, and eigenvectors of deformation measures

The right stretch tensor U has the relationship

$$U N_a = \lambda_a N_a, \text{ where } |N_a| = 1, \text{ and } a = 1, 2, 3. \tag{2.15}$$

The set $\{N_a\}$ defines the eigenvectors of U, while λ_a are the eigenvalues. From 2.14,

$$C N_a = U^2 N_a = \lambda_a^2 N_a, \ a = 1, 2, 3. \tag{2.16}$$

Since both U and C are purely Lagrangian measures, their eigenvectors are the same, which are called the principal axes. A similar relationship can be obtained for b using 2.14, i.e.,

$$b n_a = v^2 n_a = \lambda_a^2 n_a \tag{2.17}$$

where $n_a = R N_a$ for $a = 1, 2, 3$. This relationship shows the fact that v and b are colinear in spatial coordinates. For $\lambda_1 \neq \lambda_2 \neq \lambda_3$, the symmetric tensors U, v, C, b can be written in their so called spectral decomposition forms

$$U^2 = C = \sum_{a=1}^{3} \lambda_a^2 N_a \otimes N_a, \tag{2.18}$$

$$v^2 = b = \sum_{a=1}^{3} \lambda_a^2 n_a \otimes n_a, \tag{2.19}$$

Finally, the deformation gradient can also be written as

$$F = \sum_{a=1}^{3} \lambda_a n_a \otimes N_a, \tag{2.20}$$

which is a two-point tensor. Since F may not be symmetric λ_as cannot be considered as the eigenvalues of F directly. Similarly, $R = \sum_{a=1}^{3} n_a \otimes N_a$ is also a two-point tensor.

Since both C and b are symmetric and positive definite, they admit 3 uniquely defined invariants. The scalar invariants of C can be summarized as,

$$I_1(C) = \lambda_1^2 + \lambda_2^2 + \lambda_3^2, \tag{2.21}$$

$$I_2(C) = \lambda_1^2 \lambda_2^2 + \lambda_1^2 \lambda_3^2 + \lambda_2^2 \lambda_3^2, \tag{2.22}$$

$$I_3(C) = \lambda_1^2 \lambda_2^2 \lambda_3^2 = J^2. \tag{2.23}$$

2.1.1.2 Rates of the deformation measures

The spatial velocity gradient,

$$l(x, t) = \frac{\partial v(x, t)}{\partial x} = \text{grad}(v(x, t)) \tag{2.24}$$

and the material velocity gradient,

$$\dot{F}(x, t) = \text{Grad}(V(X, t)) \tag{2.25}$$

are two major deformation rate measures. l has the property,

$$l = \text{grad}(v(x, t)) = \dot{F} F^{-1}. \tag{2.26}$$

Other valueable deformation metrics

$$d = \frac{1}{2} \left(l + l^T \right) = \text{sym}(gl), \text{ and } \quad w = \frac{1}{2} \left(l - l^T \right) = \text{skew}(gl) \tag{2.27}$$

are the rate of deformation and spin tensors, respectively. They are the symmetric and skew-symmetric parts of the l.

2.1.1.3 Push-forward, pull-back, and Lie time derivative

If we assume separate reference frames for the reference and current configurations, the vectorial and tensorial quantities can be resolved in one of them, by choice. Transformation between material and spatial coordinates is achieved by *push-forward* and *pull-back* operations. These are denoted as $\chi_*(\bullet)$ and $\chi^*(\bullet)$, respectively. We define the push-forward of covariant $(\bullet)^\flat$ and contravariant $(\bullet)^\sharp$ objects

$$\chi_* (\bullet)^\flat = F^{-T} (\bullet)^\flat F^{-1} \quad \text{and} \quad \chi_* (\bullet)^\sharp = F (\bullet)^\sharp F^T. \tag{2.28}$$

Similarly, the pull-back of covariant $(\bullet)^\flat$ and contravariant $(\bullet)^\sharp$ objects read

$$\chi^* (\bullet)^\flat = F^T (\bullet)^\flat F \quad \text{and} \quad \chi^* (\bullet)^\sharp = F^{-1} (\bullet)^\sharp F^{-T}. \tag{2.29}$$

Lie derivative of an Eulerian object is the push-forward of the material time derivative of the corresponding Lagrangian object, i.e., $\mathcal{L}(\bullet) := \chi_* \left(\overline{\dot{\chi^* (\bullet)}} \right)$, which is utilized to obtain objective time derivatives of Eulerian objects.

2.2 Concept of stress
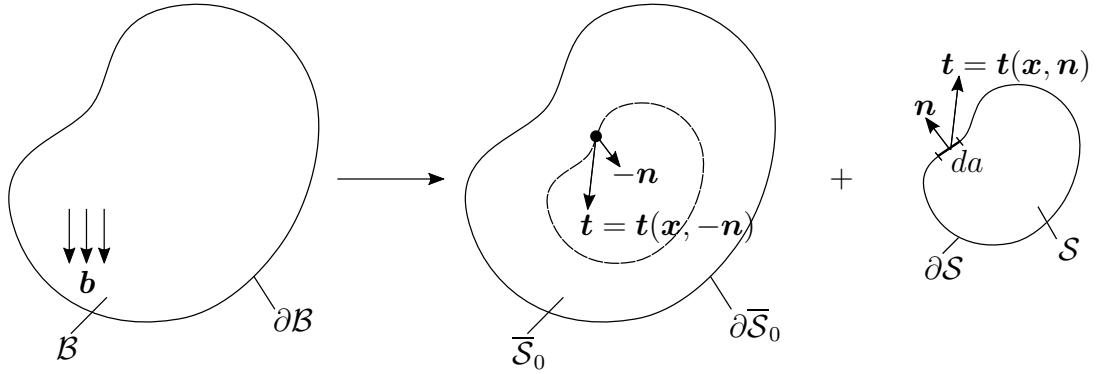
Figure 2.1: Removal of a slice $\mathcal{S}$ from the body $\mathcal{B}$, illustrating the tractions and the normals for the slice $\mathcal{S}$ and the remaining part $\overline{\mathcal{S}}$.

Let the body $\mathcal{B}$ have some boundary conditions over $\partial\mathcal{B}$ and body forces acting on it. Assume a slice of $\partial\mathcal{S}$ has been carved out as shown in Fig. 2.1. The slice $\mathcal{S}$ is then subjected to the traction $\boldsymbol{t}$ and body force $\boldsymbol{b}$ in current configuration. The net forces on slice $\mathcal{S}$ of body $\mathcal{B}$ and the remaining part $\overline{\mathcal{S}}$ are as follows

$$\boldsymbol{\mathcal{F}}_1 = \int_{\mathcal{S}} \boldsymbol{b}dv + \int_{\partial\mathcal{S}} \boldsymbol{t}(\boldsymbol{x},\boldsymbol{n})ds, \tag{2.30}$$

$$\boldsymbol{\mathcal{F}}_2 = \int_{\overline{\mathcal{S}}} \boldsymbol{b}dv + \int_{\partial\overline{\mathcal{S}}} \boldsymbol{t}(\boldsymbol{x},-\boldsymbol{n})ds. \tag{2.31}$$

The net force acting on the body is $\boldsymbol{\mathcal{F}} = \boldsymbol{\mathcal{F}}_1 + \boldsymbol{\mathcal{F}}_2$, and note that $\int_{\mathcal{B}} \boldsymbol{b}dv = \int_{\mathcal{S}} \boldsymbol{b}dv + \int_{\overline{\mathcal{S}}} \boldsymbol{b}dv$. These relationships yield the important equality,

$$\int_{\partial\mathcal{S}} \boldsymbol{t}(\boldsymbol{x},\boldsymbol{n})ds + \int_{\partial\overline{\mathcal{S}}} \boldsymbol{t}(\boldsymbol{x},-\boldsymbol{n})ds = 0 \tag{2.32}$$

which can be rewritten in local form as

$$\boldsymbol{t}(\boldsymbol{x},\boldsymbol{n}) = -\boldsymbol{t}(\boldsymbol{x},-\boldsymbol{n}). \tag{2.33}$$

This relation is known as the *Cauchy's fundamental lemma*, and corresponds to the Newton's third law of motion. If we define a tensorial quantity $\boldsymbol{\sigma}$ on a point, then the traction $\boldsymbol{t}$ at that point can be stated as

$$\boldsymbol{t} = \boldsymbol{\sigma} \cdot \boldsymbol{n} \tag{2.34}$$

where $\boldsymbol{n}$ is the normal to the cut surface. This relationship is known as the *Cauchy's stress theorem*. And the tensor $\boldsymbol{\sigma}$ is also called the *Cauchy stress*. Using the Nanson's formula 2.9, we may arrive to an important alternative stress measure,

$$\tilde{\boldsymbol{P}} = J\boldsymbol{\sigma}\boldsymbol{F}^{-T} = \boldsymbol{\tau}\boldsymbol{F}^{-T} \tag{2.35}$$

where $\tilde{\boldsymbol{P}}$ is the first Piola-Kirchhoff stress and $\boldsymbol{\tau} = J\boldsymbol{\sigma}$ is the Kirchhoff stress tensors. The symmetric second Piola-Kirchhoff stress ($\boldsymbol{S}$) is defined as the semi-pull-back of the first Piola-Kirchhoff stress

$$\boldsymbol{S} = \boldsymbol{F}^{-1}\tilde{\boldsymbol{P}} = \boldsymbol{F}^{-1}\boldsymbol{\tau}\boldsymbol{F}^{-T}. \tag{2.36}$$

2.3 Balance laws

The motion or the state of a body is not arbitrary and must obey the rules of physics. These rules can be stated as concise balance laws, where at the end, we can come up with field equations (or governing equations). We will briefly touch the basic definitions of the balance laws.

2.3.1 Balance of mass

For a closed system, as in the body $\mathcal{B}$, the mass per unit volume is a fundamental quantity which measures the amount of material within the system. Let $\rho_0(\boldsymbol{X})$ denote the mass density in reference configuration, while $\rho(\boldsymbol{x}, t)$ denote its spatial counterpart. Furthermore, let the total mass of the body be defined as,

$$M = \int_{\Omega} \rho(\boldsymbol{x}, t) dv = \int_{\Omega_0} \rho_0(\boldsymbol{X}) dV \tag{2.37}$$

where Ω_0 and Ω denote the region of space occupied by the body $\mathcal{B}$ in reference and current configurations, respectively. The conservation of mass states that over the time, for a closed system, the total mass stays constant, that is, the material time derivative of the total mass

$$\dot{M} = 0 \implies \dot{\rho}_0 = 0. \tag{2.38}$$

This simple equation represents the balance of mass in Lagrangian description. On equation 2.37, from the volume map, we can see,

$$\rho_0(\mathbf{X}) = J(\mathbf{X}, t)\rho(\mathbf{x}, t) \tag{2.39}$$

One can apply equation 2.38 to 2.37, also using 2.39 and observe the property,

$$\dot{M} = \frac{D}{Dt}\int_{\mathcal{B}_0}\rho_0(\mathbf{X})dV = \int_{\mathcal{B}_0}\frac{D(J\rho)}{Dt}dV = 0. \tag{2.40}$$

The last part of this equation, when localized, boils down to

$$\frac{D(J\rho)}{Dt} = \overline{\dot{J\rho}} = 0. \tag{2.41}$$

We can resolve the last part as,

$$\overline{\dot{J\rho}} = \dot{J}\rho + J\dot{\rho} = 0. \tag{2.42}$$

One can derive $\dot{J} = \overline{\det \mathbf{F}} = J\mathrm{div}\,\mathbf{v}$. Using this relationship,

$$J\dot{\rho} + \rho J\mathrm{div}\,\mathbf{v} = 0 \implies \boxed{\dot{\rho} + \rho\mathrm{div}\,\mathbf{v} = 0} \tag{2.43}$$

is obtained. Which states the balance of mass in spatial (Eulerian) description. $\dot{\rho} = 0$ implies an important kinematical constraint on the motion, that is $\mathrm{div}\,\mathbf{v} = 0$. This type of motion is called isochoric, or volume-preserving, and has intrinsic ties to the history of the hyperelasticity for rubber-like materials, which are considered quasi-incompressible.

2.3.2 Balance of linear momentum
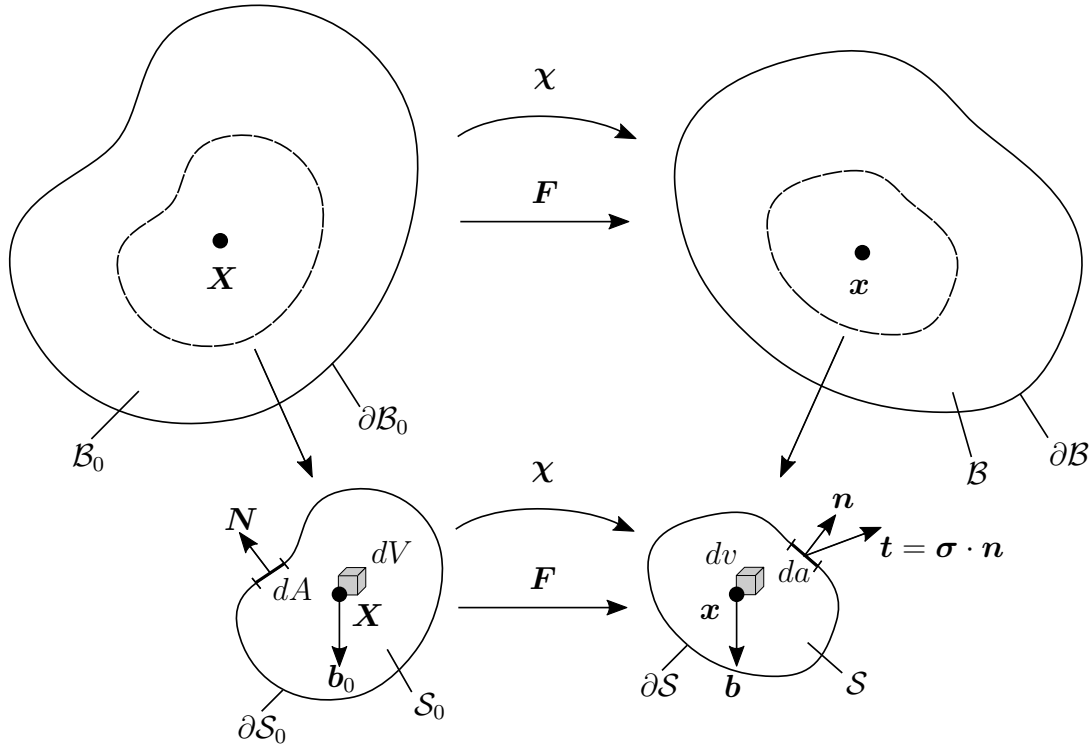
Figure 2.2: Deformation as felt by a slice of region cut from the body, the traction t, and body force b are shown as reference for the text.

Let the body $\mathcal{B}$ have some boundary conditions over $\partial\mathcal{B}$ and body forces acting on it. Assume a slice of $\partial\mathcal{S}$ has been carved out as shown in Fig. 2.2. The slice $\mathcal{S}$ is then subjected to the traction t and body force b in current configuration. Let the total force acting on the slice be represented by $\mathcal{F}$, that is

$$\mathcal{F} = \int_{\mathcal{S}} b\,dv + \int_{\partial\mathcal{S}} t\,ds. \tag{2.44}$$

The linear momentum $\mathcal{I} = \int_{\mathcal{S}} \rho v\,dv$ of the slice $\mathcal{S}$ is conserved, that can be written mathematically as

$$\frac{D(\mathcal{I})}{Dt} = \mathcal{F}, \tag{2.45}$$

which states that the rate of change of the linear momentum is equal to the net force acting on the slice. We can apply the Cauchy's theorem $t = \sigma \cdot n$, thus, equation 2.44

can be rewritten in Lagrangian setting as

$$\boldsymbol{\mathcal{F}} = \int_{\mathcal{S}} \boldsymbol{b} dv + \int_{\partial \mathcal{S}} \boldsymbol{\sigma} \cdot \boldsymbol{n} ds. \tag{2.46}$$

We can apply the Gauss theorem to convert the area integral on tractions to volume integral,

$$\int_{\partial \mathcal{S}} \boldsymbol{t} ds = \int_{\mathcal{S}} \mathrm{div}\,(\boldsymbol{\sigma})\, dv = \int_{\mathcal{S}_0} \mathrm{Div}\left(\tilde{\boldsymbol{P}}\right) dV \tag{2.47}$$

Using $\boldsymbol{V} = \boldsymbol{V}[\boldsymbol{X}, t]$ and the conservation of mass statement $\rho_0 = J\rho$, the rate of the linear momentum can be written in Lagrangian configuration,

$$\boldsymbol{\mathcal{I}} = \int_{\mathcal{S}} \rho \boldsymbol{v} dv = \int_{\mathcal{S}_0} \rho_0 \boldsymbol{V} dV \implies \frac{D(\boldsymbol{\mathcal{I}})}{Dt} = \int_{\mathcal{S}_0} \rho_0 \dot{\boldsymbol{V}} dV \tag{2.48}$$

Now, the balance of linear momentum can be written as,

$$\int_{\mathcal{S}_0} \rho_0 \dot{\boldsymbol{V}} dV = \int_{\mathcal{S}_0} \boldsymbol{b}_0 dV + \int_{\mathcal{S}_0} \mathrm{Div}\left(\tilde{\boldsymbol{P}}\right) dV \tag{2.49}$$

where $\boldsymbol{b}_0$ is the body forces in the Lagrangian configuration. When the global form 2.49 is localized as $\mathcal{S}_0 \to dV$, one obtains

$$\rho_0 \dot{\boldsymbol{V}} = \mathrm{Div}\left(\tilde{\boldsymbol{P}}\right) + \boldsymbol{b}_0. \tag{2.50}$$

In Eulerian coordinates, with the Piola identity and Reynold's transport theorem,

$$\rho \dot{\boldsymbol{v}} = \mathrm{div}\,(\boldsymbol{\sigma}) + \boldsymbol{b} \tag{2.51}$$

is obtained.

2.3.3 Balance of angular momentum
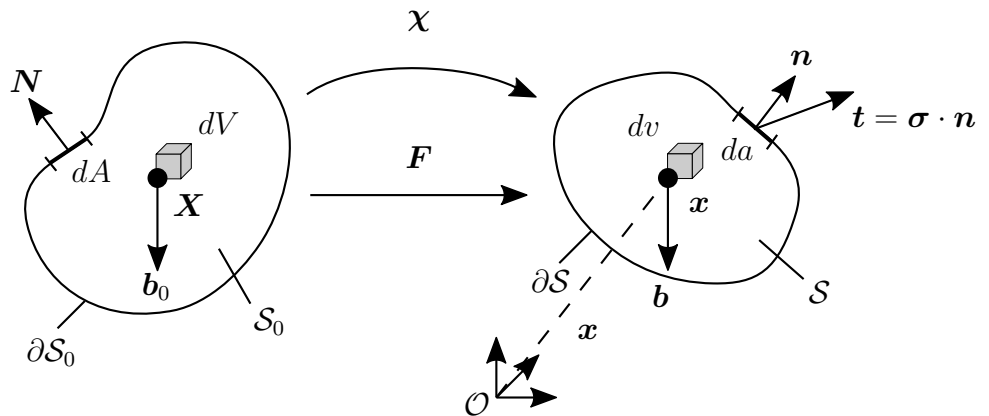
Figure 2.3: Deformation as felt by a slice of region cut from the body, the traction $\boldsymbol{t}$, and body force $\boldsymbol{b}$, as well as the moment arm $\boldsymbol{x}$ are shown for reference.

Consider the slice in Fig. 2.2 be zoomed in and shown in Fig. 2.3. The angular momentum of the slice $\mathcal{S}$ can be defined as $\boldsymbol{\mathcal{D}}_{\mathcal{O}} = \int_{\mathcal{S}} \boldsymbol{x} \times \rho \boldsymbol{v} dv$, with respect to a fixed point $\mathcal{O}$. And let $\boldsymbol{\mathcal{M}}_{\mathcal{O}} = \int_{\partial \mathcal{S}} \boldsymbol{x} \times \boldsymbol{t} ds + \int_{\mathcal{S}} \boldsymbol{x} \times \boldsymbol{b} dv$ be the net moment acting on the slice $\mathcal{S}$. The balance of angular momentum reads

$$\frac{D(\boldsymbol{\mathcal{D}}_{\mathcal{O}})}{Dt} = \boldsymbol{\mathcal{M}}_{\mathcal{O}} \tag{2.52}$$

which states that the rate of change of the angular momentum with respect to $\mathcal{O}$ must be equal to the net moment acting on the slice $\mathcal{S}$ with respect to $\mathcal{O}$. Using the local form of the mass balance $\rho_0 = J\rho$, and the volume transformation $dv = JdV$,

$$\frac{D(\boldsymbol{\mathcal{D}}_{\mathcal{O}})}{Dt} = \frac{D}{Dt} \int_{\mathcal{S}} \boldsymbol{x} \times \rho \boldsymbol{v} dv = \int_{\mathcal{S}_0} \boldsymbol{x} \times \rho_0 \dot{\boldsymbol{V}} dV \tag{2.53}$$

can be written. The moments can be transformed to the fixed domain $\mathcal{S}_0$ through the Cauchy's theorem $\boldsymbol{t} = \boldsymbol{\sigma} \cdot \boldsymbol{n}$, Gauss theorem, the definition of the cross-product, and the Piola identity as

$$\boldsymbol{\mathcal{M}}_{\mathcal{O}} = \int_{\mathcal{S}_0} \boldsymbol{x} \times \mathrm{Div}\left(\tilde{\boldsymbol{P}}\right) dV + \int_{\mathcal{S}_0} \frac{1}{2} \epsilon_{ijk} \left(\sigma_{ji} - \sigma_{ij}\right) JdV + \int_{\mathcal{S}_0} \boldsymbol{x} \times \boldsymbol{b}_0 dV. \tag{2.54}$$

The conservation of angular momentum statement can be rewritten with the above transformations in the form,

$$\int_{\mathcal{S}_0} \boldsymbol{x} \times \left[\rho_0 \dot{\boldsymbol{V}} - \mathrm{Div}\left(\tilde{\boldsymbol{P}}\right) - \boldsymbol{b}_0\right] dV = \int_{\mathcal{S}_0} \frac{1}{2} \epsilon_{ijk} \left(\sigma_{ji} - \sigma_{ij}\right) JdV. \tag{2.55}$$

Notice that the left hand side of this equation becomes 0 from the conversation of linear momentum equation 2.50. Which yields,

$$\sigma_{ji} = \sigma_{ij} \implies \boldsymbol{\sigma}^T = \boldsymbol{\sigma} \tag{2.56}$$

that is, the Cauchy stress is symmetric. With some simple manipulations, we can show that the second Piola-Kirchhoff stress is also symmetric,

$$\boldsymbol{S}^T = \boldsymbol{S}. \tag{2.57}$$

However, we can not make the same statement, in general, for $\tilde{\boldsymbol{P}} = \boldsymbol{F}\boldsymbol{S}$, i.e., $\boldsymbol{F}\boldsymbol{S} \neq \boldsymbol{S}\boldsymbol{F}^T$ in general.

24

2.3.4 Balance of energy
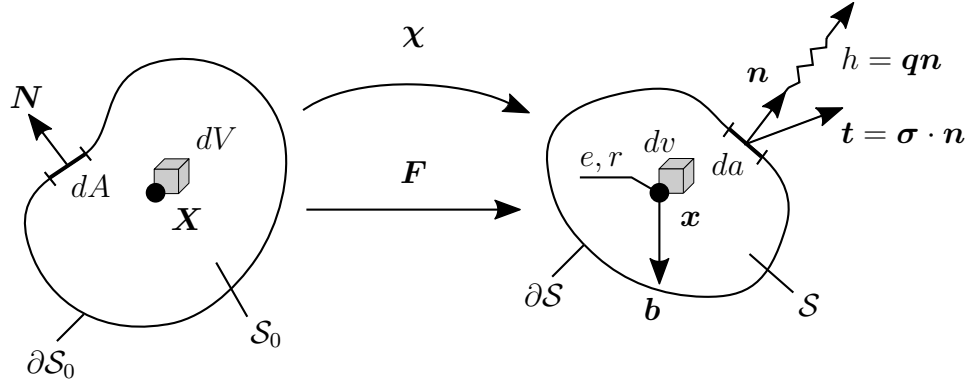
Figure 2.4: Deformation as felt by a slice of region cut from the body, the heat flux h, and the local thermodynamical state e and r are illustrated for reference.

The heat flux $h(\boldsymbol{x}, t; \boldsymbol{n})$ describes the thermal influence of the rest of the body to the slice $\mathcal{S}$ as shown in Fig. 2.4. It can be phenomenologically written as,

$$h(\boldsymbol{x}, t; \boldsymbol{n}) = \boldsymbol{q}(\boldsymbol{x}, t) \cdot \boldsymbol{n} \tag{2.58}$$

using the Eulerian heat flux vector $\boldsymbol{q}(\boldsymbol{x}, t)$. In the Lagrangian configuration, the heat flux vector reads

$$\boldsymbol{Q} = J\boldsymbol{q}\boldsymbol{F}^{-T}. \tag{2.59}$$

The first axiom of the thermodynamics, also known as the balance of energy, describes the evolution of internal energy in a system, measuring the capacity to do work. This balance law states that the conservation of energy is achieved by equilibrating the rate of total energy to the sum of external mechanical and thermal power. The total energy is the sum of kinetic energy $\mathcal{K}$ and internal energy $\mathcal{E}$,

$$\mathcal{T} = \mathcal{K} + \mathcal{E} \tag{2.60}$$

where,

$$\mathcal{K} = \int_{\mathcal{S}} \frac{1}{2} \rho \boldsymbol{v} \cdot \boldsymbol{g} \boldsymbol{v} dv, \quad \text{and} \quad \mathcal{E} = \int_{\mathcal{S}} e \, dv \tag{2.61}$$

in the specific form. In these definitions, $e = e(\boldsymbol{x}, t)$ denotes the internal energy density per unit volume with the material representation $e_0[\boldsymbol{X}, t]$. The Eulerian metric

g is necessary to be able to multiply two vs in tangent space. The external mechanical and thermal powers are

$$\mathcal{P} = \int_{\mathcal{S}} \boldsymbol{b} \cdot \boldsymbol{g}\boldsymbol{v}dv + \int_{\partial\mathcal{S}} \boldsymbol{t} \cdot \boldsymbol{g}\boldsymbol{v}ds, \quad \text{and} \quad \mathcal{Q} = \int_{\mathcal{S}} rdv - \int_{\partial\mathcal{S}} \boldsymbol{q}\boldsymbol{n}ds \qquad (2.62)$$

respectively. In these definitions, similarly metric tensor g is utilized. Note that $r = r(\boldsymbol{x}, t)$ is a given heat source per unit volume. Then, the balance of energy statement reads

$$\frac{D[\mathcal{K} + \mathcal{E}]}{Dt} = \mathcal{P} + \mathcal{Q}. \qquad (2.63)$$

The surface integral in 2.62 can be rewritten using the spatial velocity gradient $\boldsymbol{l} = \nabla_{\boldsymbol{x}}\boldsymbol{v}$ and Cauchy's theorem and reads

$$\int_{\partial\mathcal{S}} \boldsymbol{t} \cdot \boldsymbol{g}\boldsymbol{v}ds = \int_{\mathcal{S}} \text{div}\left(\boldsymbol{\sigma}\right) \cdot \boldsymbol{g}\boldsymbol{v}dv + \int_{\mathcal{S}} \boldsymbol{\sigma} : \boldsymbol{g}\boldsymbol{l}dv. \qquad (2.64)$$

Utilizing volume map J, the Piola identity and $J\boldsymbol{\sigma} : \boldsymbol{g}\boldsymbol{l} = J\boldsymbol{\sigma}\boldsymbol{F}^{-T} : \boldsymbol{g}\dot{\boldsymbol{F}} = \boldsymbol{g}\tilde{\boldsymbol{P}} : \dot{\boldsymbol{F}} = \boldsymbol{P} : \dot{\boldsymbol{F}}$ we can convert the Eulerian representation given in 2.64 to the Lagrangian representation

$$\int_{\mathcal{S}} \boldsymbol{t} \cdot \boldsymbol{g}\boldsymbol{v}ds = \int_{\mathcal{S}_0} \text{Div}\left(\tilde{\boldsymbol{P}}\right) \cdot \boldsymbol{g}\boldsymbol{V}dV + \int_{\mathcal{S}_0} \boldsymbol{P} : \dot{\boldsymbol{F}}dV \qquad (2.65)$$

Substitution to the balance of energy statement 2.63 yields

$$\dot{e}_0 = \boldsymbol{P} : \dot{\boldsymbol{F}} + r_0 - \text{Div}\left(\boldsymbol{Q}\right) \qquad (2.66)$$

where $r_0 = r_0[\boldsymbol{X}, t]$ is the material representation of the local heat source. The Eulerian counterpart of the balance of energy reads

$$\dot{e} = \boldsymbol{\sigma} : \boldsymbol{g}\boldsymbol{l} + r - \text{div}\left(\boldsymbol{q}\right). \qquad (2.67)$$

26

2.3.5 Second law of thermodynamics
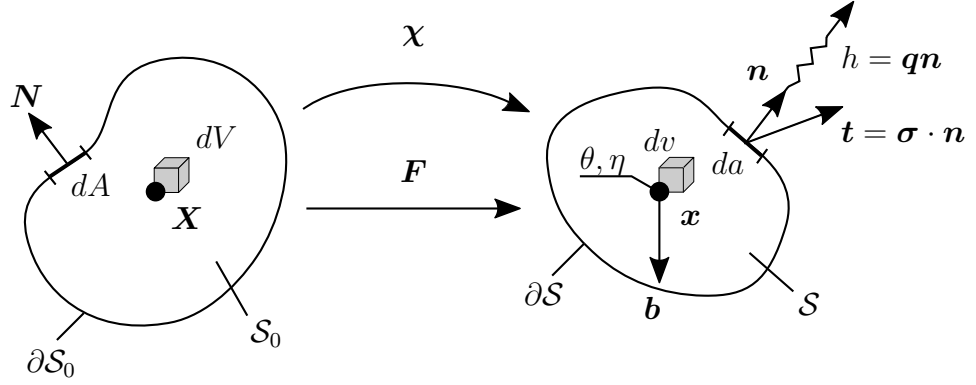
Figure 2.5: Deformation as felt by a slice of region cut from the body, the heat flux h, and the local thermodynamical state θ and η are illustrated for reference.

If a thermodynamical system is perturbed, the second law of thermodynamics provides a direction of energy transfer by setting a major restriction on the constitutive equations governing the material behavior. Let $\mathfrak{S} = \int_{\mathcal{S}} \rho\gamma dv$ be the entropy production for the slice $\mathcal{S}$, where γ is the local entropy production per unit current volume. The total entropy of the system is $\mathrm{S} = \int_{\mathcal{S}} \eta dv$, where η is the local entropy per unit current volume. The received quantity of heat H per unit temperature is $\mathrm{H} = \int_{\mathcal{S}} \frac{r}{\theta} dv - \int_{\partial \mathcal{S}} \frac{1}{\theta} \boldsymbol{q} \boldsymbol{n} ds$. The second law of thermodynamics restricts the entropy production to be positive,

$$\mathfrak{S} := \frac{D}{Dt}\mathrm{S} - \mathrm{H} \geq 0. \tag{2.68}$$

Utilizing $\gamma_0 = \gamma_0[\boldsymbol{X}, t]$, and $\eta_0 = \eta_0[\boldsymbol{X}, t]$ as the Lagrangian counterparts of γ and η, and the volume map J, the Lagrangian and Eulerian representations of the second axiom of thermodynamics become

$$\rho_0\gamma_0 = \dot{\eta}_0 - \frac{1}{\theta}\left(r_0 - \mathrm{Div}\left(\boldsymbol{Q}\right)\right) - \frac{1}{\theta^2}\boldsymbol{Q}\mathrm{Grad}(\theta) \geq 0 \tag{2.69}$$

and

$$\rho\gamma = \dot{\eta} - \frac{1}{\theta}\left(r - \mathrm{div}\left(\boldsymbol{q}\right)\right) - \frac{1}{\theta^2}\boldsymbol{q}\mathrm{grad}(\theta) \geq 0 \tag{2.70}$$

respectively. These two local forms restricts the direction of heat transfer from higher to lower temperature. These inequalities are known as the *Clasius-Duhem inequalities* in Lagrangian and Eulerian representations, respectively. Noting θ in these equa-

tions are non-negative (measured in Kelvin), we can show an alternative more restrictive forms,

$$\mathcal{D}_{int} = \boldsymbol{P} : \dot{\boldsymbol{F}} - \dot{e}_0 + \theta\dot{\eta}_0 \geq 0 \qquad (2.71)$$

and

$$\mathcal{D}_{int} = \boldsymbol{\sigma} : \boldsymbol{gl} - \dot{e} + \theta\dot{\eta} \geq 0 \qquad (2.72)$$

in Lagrangian and Eulerian representations, where $\mathcal{D}_{int}$ is the internal dissipation or the local production of entropy. These stronger forms of the second axiom of thermodynamics are known as *Clasius-Planck inequalities* in Lagrangian and Eulerian representations. Utilizing the Legendre transformation $\Psi = e_0 - \theta\eta_0$, where Ψ is the free energy per unit reference volume, then the *Clasius-Planck inequality* in Lagrangian representation reads

$$\mathcal{D}_{int} = \boldsymbol{P} : \dot{\boldsymbol{F}} - \dot{\Psi} - \eta_0\dot{\theta} \geq 0. \qquad (2.73)$$

For a purely mechanical process where θ and η are omitted,

$$\mathcal{D}_{int} = \boldsymbol{P} : \dot{\boldsymbol{F}} - \dot{\Psi} \geq 0. \qquad (2.74)$$

For a perfectly elastic process (where no local entropy production happens) or a at local equilibrium, $\mathcal{D}_{int} = 0$, we can find $\dot{\psi} = \boldsymbol{P} : \dot{\boldsymbol{F}}$, which leads to the *Coleman-Noll procedure* [116] as will be explained in hyperelasticity section.

2.4 Hyperelasticity and constitutive relations

A hyperelastic material assumes the existence of a Helmholtz free-energy function Ψ. It is also known as strain-energy density if $\Psi = \Psi(\boldsymbol{F})$, i.e., it is only a function of deformation $\boldsymbol{F}$. If we take the rate of Ψ,

$$\frac{D}{Dt}\Psi(\boldsymbol{F}) = \partial_{\boldsymbol{F}}\Psi(\boldsymbol{F}) : \dot{\boldsymbol{F}} \qquad (2.75)$$

is obtained. Using 2.74 here, for a perfectly elastic material ($\mathcal{D}_{int} = 0$),

$$\mathcal{D}_{int} = \boldsymbol{P} : \dot{\boldsymbol{F}} - \dot{\Psi} = \left(\boldsymbol{P} - \frac{\partial\Psi(\boldsymbol{F})}{\partial\boldsymbol{F}}\right) : \dot{\boldsymbol{F}} = 0, \qquad (2.76)$$

is found. From this relationship, $\boldsymbol{P} = \partial\Psi(\boldsymbol{F})/\partial\boldsymbol{F}$ can be obtained. This set of manipulations is known as the *Coleman-Noll procedure*.

Rubber-like materials are modeled with a Helmholtz free-energy function, in general. The underlying theories of the rubber elasticity come from the thermodynamical considerations and the statistical mechanics. We can see three types of constitutive relations for rubber-like materials in literature, namely the micro-mechanical, phenomenological, and hybrid models. These has been reviewed in one of our studies [37] and 44 hyperelastic models are compared. Among established models from literature, a specific form has been proposed in [43], which is called the compressible extended eight-chain model. This model will be explained in detail in Chapter 3 and the micro-mechanical derivations are provided for the second invariant term. For details of the hyperelasticty, we refer the interested reader to DAL ET AL. [37], HAUPT [114], and HOLZAPFEL [115].

CHAPTER 3

FINITE VISCOELASTICITY AND THE EXTENDED EIGHT-CHAIN MODEL

Elastomers or rubber-like materials demonstrate strong rate dependent effects in their mechanical behavior. The basic hyperelasticity (and thus, existence of a Helmholtz free energy function) assumes fully recoverable deformations, i.e. purely elastic deformations. This enables working with large (or finite) deformations possible in theory and simulations. However, rubber-like materials and polymers in general, exhibit strong inelastic/dissipative behavior as well. This corresponds to perturbations around thermodynamic equilibrium, the intensity of which dictate the small or finite viscoelastic considerations, i.e., linear or non-linear evolution equations. Here, we consider a naming convention from REESE & GOVINDJEE [60] for the class of theories in the literature,

- **linear viscoelasticity:** linear elastic + small perturbations away from thermodynamic equilibrium,

- **hyper viscoelasticity:** hyperelastic + small perturbations away from thermodynamic equilibrium,

- **finite viscoelasticity:** hyperelastic + large perturbations away from thermodynamic equilibrium.

The last type of formalism listed above is of concern in this thesis, i.e. the theory presented in this thesis is applicable to large strain rates and encompasses a non-linear evolution law. The layout of this part is as follows, first we will introduce a multiplicative decomposition and its geometrical implications for deformation gradient and define a fictitious intermediate configuration. Next a generalized Maxwell-Wiechert

31

model, consistent with the multiplicative split is given for the rheology of the material. A physically based evolution form for the relaxation kinetics of a single chain is derived and linked to the network average stretch of eight chain model. The algorithmic treatment based on elastic predictor and inelastic corrector steps for the calculation of elastic left Cauchy-Green tensor are then established. Finally, the spatial consistent tangent moduli is derived explicitly.

3.1 A multiplicative decomposition for deformation gradient and its geometrical implications

The internal variable formulations for finite viscoelasticity concern with the definition of internal state variables to distinguish viscous deformations and focus primarily on the evolution equations related to these variables. A particularly successfuly approach is to decompose the total deformation gradient $\boldsymbol{F}$ multiplicatively into viscous ($\boldsymbol{F}^v$) and elastic ($\boldsymbol{F}^e$) parts in the sense of KRÖNER [117] and LEE [118], i.e.,

$$\boldsymbol{F} = \boldsymbol{F}^e \boldsymbol{F}^v \qquad (3.1)$$

Such a decomposition defines a two step transformation between reference and current configurations. In the first step the viscous part brings the undeformed configuration to a fictitious intermediate configuration. Then, in the second step, the elastic part transforms the intermediate configuration to the current configuration. The decomposition requires the definition of the fictitious tangent $\bar{T}_{\bar{X}}\mathscr{B}$ and co-tangent $\bar{T}_{\bar{X}}^*\mathscr{B}$ spaces. These two spaces are connected by the fictitious metric $\tilde{\boldsymbol{G}}$ with the definition $\tilde{\boldsymbol{G}} : \bar{T}_{\bar{X}}\mathscr{B} \to \bar{T}_{\bar{X}}^*\mathscr{B}$. The associated transformations between Lagrangian and Eulerian manifolds are summarized in Figure 3.1 in terms of pull-back and push-forward relationships for the intermediate configuration. By the help of the intermediate configuration we can define *elastic right Cauchy Green tensor* and *elastic inverse left Cauchy Green tensor*

$$\boldsymbol{C}^e = \boldsymbol{F}^{eT}\boldsymbol{g}\boldsymbol{F}^e \qquad \text{and} \qquad \boldsymbol{c}^e = \boldsymbol{F}^{e-T}\tilde{\boldsymbol{G}}\boldsymbol{F}^{e-1} \qquad (3.2)$$

as the pull-back of the metric tensor $\boldsymbol{g}$ into intermediate configuration and push-forward of the intermediate metric $\tilde{\boldsymbol{G}}$ to the current configuration, respectively. More-

over, it can be shown that the viscous metric $\boldsymbol{C}^v = \boldsymbol{F}^T \boldsymbol{c}^e \boldsymbol{F}$ is the pull-back of the inverse of left Cauchy-Green tensor to the reference configuration.
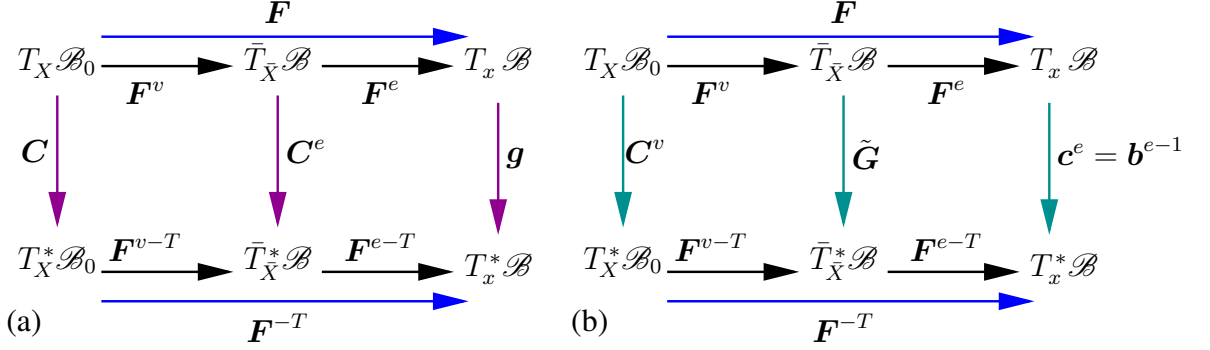
Figure 3.1: Push-forward and pull-back relations of the current and intermediate metric tensors. (a) Pull-back of the *current metric* $\boldsymbol{g}$ to the Lagrangian $\boldsymbol{C} = \boldsymbol{F}^T \boldsymbol{g} \boldsymbol{F}$ and the intermediate $\boldsymbol{C}^e = \boldsymbol{F}^{eT} \boldsymbol{g} \boldsymbol{F}^e$ configurations. (b) Pull-back of the *intermediate metric* $\tilde{\boldsymbol{G}}$ to the Lagrangian $\boldsymbol{C}^v = \boldsymbol{F}^{vT} \tilde{\boldsymbol{G}} \boldsymbol{F}^v$ and its push-forward to the Eulerian configuration $\boldsymbol{c}^e = \boldsymbol{F}^{e-T} \tilde{\boldsymbol{G}} \boldsymbol{F}^{-1}$.

3.1.1 Rates of deformation and stress measures

Based on the aforementioned setting and using the notation $\nabla_{\boldsymbol{X}}$ and $\nabla_{\boldsymbol{x}}$ for gradients with respect to reference and spatial coordinates, we can establish the material and spatial velocity gradients as

$$\dot{\boldsymbol{F}} = \nabla_{\boldsymbol{X}} \dot{\boldsymbol{x}} \qquad \text{and} \qquad \boldsymbol{l} = \nabla_{\boldsymbol{x}} \dot{\boldsymbol{x}} = \dot{\boldsymbol{F}} \boldsymbol{F}^{-1}, \tag{3.3}$$

respectively. The multiplicative decomposition (3.1) renders us the ability to define

$$\text{elastic}: \quad \boldsymbol{l}^e = \dot{\boldsymbol{F}}^e \boldsymbol{F}^{e-1}, \tag{3.4a}$$

$$\text{viscous}: \quad \boldsymbol{l}^v = \dot{\boldsymbol{F}}^v \boldsymbol{F}^{v-1} \tag{3.4b}$$

spatial gradient parts. The total spatial velocity gradient ($\boldsymbol{l}$) can be stated in an additive format

$$\boldsymbol{l} = \boldsymbol{l}^e + \tilde{\boldsymbol{l}}^v, \text{ using } \quad \tilde{\boldsymbol{l}}^v := \boldsymbol{F}^e \boldsymbol{l}^v \boldsymbol{F}^{e-1}. \tag{3.5}$$

Moreover, the spatial velocity gradient $\boldsymbol{l}$ can also be decomposed into two covariant tensors

$$\boldsymbol{l} = \boldsymbol{d} + \boldsymbol{w}, \text{ where} \quad \boldsymbol{d} = \text{sym}(\boldsymbol{g} \boldsymbol{l}) \quad \text{and} \quad \boldsymbol{w} = \text{skew}(\boldsymbol{g} \boldsymbol{l}) \tag{3.6}$$

33
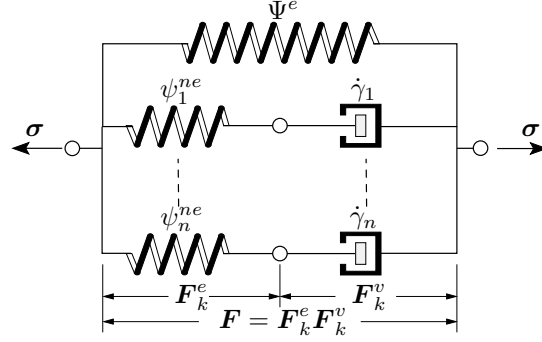
Figure 3.2: The generalized Maxwell-Wiechert viscoelastic solid with n elements in total for $k \in \{1 \dots n\}$ represented in a geometrically nonlinear setting. The nonlinear spring Ψ^e accounts for the ground state elastic response, while the nonlinear spring ψ_k^{ne} and the dashpot with the associated creep rate $\dot{\gamma}_k$ in each Maxwell element reflect the non-equilibrium (viscous) response of the material considered.

are rate of deformation and vorticity tensors, respectively. Much like the approach in (3.5), the rate of deformation tensor can also be written as

$$\boldsymbol{d} = \boldsymbol{d}^e + \tilde{\boldsymbol{d}}^v, \quad \text{where} \quad \tilde{\boldsymbol{d}}^v := \text{sym}(\tilde{\boldsymbol{l}}^v). \tag{3.7}$$

Next, we emphasize the push-forward of covariant $(\bullet)^\flat$ and contravariant $(\bullet)^\sharp$ objects

$$\boldsymbol{\chi}_* (\bullet)^\flat = \boldsymbol{F}^{-T} (\bullet)^\flat \boldsymbol{F}^{-1} \quad \text{and} \quad \boldsymbol{\chi}_* (\bullet)^\sharp = \boldsymbol{F} (\bullet)^\sharp \boldsymbol{F}^T. \tag{3.8}$$

Similarly, the pull-back of covariant $(\bullet)^\flat$ and contravariant $(\bullet)^\sharp$ objects read

$$\boldsymbol{\chi}^* (\bullet)^\flat = \boldsymbol{F}^T (\bullet)^\flat \boldsymbol{F} \quad \text{and} \quad \boldsymbol{\chi}^* (\bullet)^\sharp = \boldsymbol{F}^{-1} (\bullet)^\sharp \boldsymbol{F}^{-T}. \tag{3.9}$$

Lie derivative of an Eulerian object is the push-forward of the material time derivative of the corresponding Lagrangian object, i.e., $\mathcal{L}(\bullet) := \boldsymbol{\chi}_* \left(\overline{\boldsymbol{\chi}^* (\bullet)} \right)$. Accordingly, the objective Lie derivative of the Kirchhoff stress reads

$$\mathcal{L}_v \boldsymbol{\tau} = \dot{\boldsymbol{\tau}} - \boldsymbol{l}\boldsymbol{\tau} - \boldsymbol{\tau}\boldsymbol{l}^T, \tag{3.10}$$

where $\dot{\boldsymbol{\tau}}$ is the material time derivative of the Kirchhoff stress tensor.

3.2 A compressible finite viscoelastic constitutive model for rubberlike materials

The emphasis is placed upon the formulation of constitutive relations with regard to the equilibrium and non-equilibrium response of rubberlike materials in the sense of generalized Maxwell-Wiechert model under finite deformations. Besides, a new evolution equation for the creep/relaxation rate based on the relaxation kinetics of a single polymer chain is the subject matter of this section. Unlike the classical treatment for rubberlike materials, where volumetric and isochoric response are strictly decoupled, in what follows, we adopt a specific form of free energy density function

$$\Psi(\boldsymbol{g}, \boldsymbol{F}, \boldsymbol{F}^e) = \Psi^e(\boldsymbol{g}, \boldsymbol{F}) + \Psi^{ne}(\boldsymbol{g}, \boldsymbol{F}^e) = \Psi^e(\boldsymbol{C}) + \Psi^{ne}(\boldsymbol{C}^e) \,, \qquad (3.11)$$

which reflects the standard viscoelastic solid, i.e. Maxwell elements are established parallel to the non-linear spring characterizing the ground state elastic response. Hence, the non-equilibrium part of the free energy in (3.11) follows from the rheological structure presented in Fig. 3.2 that describes the generalized Maxwell-Wiechert model with n elements,

$$\Psi^{ne}(\boldsymbol{g}, \boldsymbol{F}^e) = \sum_{k=1}^{n} \psi_k^{ne}(\boldsymbol{g}, \boldsymbol{F}_k^e) \quad \text{or} \quad \Psi^{ne}(\boldsymbol{C}^e) = \sum_{k=1}^{n} \psi_k^{ne}(\boldsymbol{C}_k^e) \,, \qquad (3.12)$$

where the index k indicates nothing but the Maxwell elements, i.e. $k \in \{1 \ldots n\}$ incorporated into the system. Recalling (3.1), the multiplicative split of the deformation gradient for the non-equilibrium part now assumes distinct deformation process, thereby being recast in the following form

$$\boldsymbol{F} = \boldsymbol{F}_k^e \boldsymbol{F}_k^v \,. \qquad (3.13)$$

Accordingly, the total Kirchhoff and second Piola-Kirchhoff stress experienced by the viscoelastic material are given by

$$\boldsymbol{\tau} := 2\partial_{\boldsymbol{g}} \Psi(\boldsymbol{g}, \boldsymbol{F}, \boldsymbol{F}^e) = \boldsymbol{\tau}^e + \boldsymbol{\tau}^{ne} \quad \text{and} \quad \boldsymbol{S} := 2\partial_{\boldsymbol{C}} \Psi(\boldsymbol{C}, \boldsymbol{C}^e) = \boldsymbol{S}^e + \boldsymbol{S}^{ne} \,, \ (3.14)$$

with the Kirchhoff stress terms $\boldsymbol{\tau}^e$ and $\boldsymbol{\tau}^{ne}$ characterizing the equilibrium (elastic) and the non-equilibrium (viscous) stresses, respectively. By the same token, the second Piola-Kirchhoff stress terms $\boldsymbol{S}^e$ and $\boldsymbol{S}^{ne}$ indicate the equilibrium (elastic) and the non-equilibrium (viscous) stresses, respectively.

3.2.1 Equilibrium part of the constitutive model: Extended eight-chain model

In view of (3.14), the equilibrium part of the constitutive response can be defined as follows

$$\boldsymbol{\tau}^e := 2\partial_{\boldsymbol{g}}\Psi^e(\boldsymbol{g}, \boldsymbol{F}) \quad \text{and} \quad \boldsymbol{S}^e := 2\partial_{\boldsymbol{C}}\Psi^e(\boldsymbol{C}) . \tag{3.15}$$

In the following sub-section, we will elaborate on the specific form of the constitutive response in the sense of Kirchhoff stress $\boldsymbol{\tau}^e$.

3.2.1.1 Micro-molecular motivation for the extended eight-chain model

The entropy describes the available conformations of a single polymer chain. Following MIEHE ET AL. [33], the joint probability density of a single chain in a tube-like constraint environment can be multiplicatively split into two independent events, i.e. $p(\lambda, \nu) = p_f(\lambda)p_c(\nu)$, where p_f and p_c represent the probability densities due to free chain response and tube-constraint parts, respectively. The entropic elasticity postulates

$$\psi(\lambda, \nu) = -\theta\eta(\lambda, \nu) \quad \text{with} \quad \eta = k_B \ln p(\lambda, \nu) \quad \rightsquigarrow \quad \eta(\lambda, \nu) = \eta_f(\lambda) + \eta_c(\nu) , \tag{3.16}$$

where θ and η stand for the temperature and the entropy, respectively, while k_B denotes the Boltzmann constant. The entropy in (3.16) additively decomposes into free and constraint parts, i.e. $\eta_f = k_B \ln p_f$ and $\eta_c = k_B \ln p_c$, respectively. Consequently, the free energy function of a single chain in a tube-like constraint environment reads

$$\psi(\lambda, \nu) = \psi_f(\lambda) + \psi_c(\nu) . \tag{3.17}$$

The non-Gaussian probability density function for the free chain response by KUHN & GRÜN [28] reads

$$p_f(\lambda) = p_0 \exp\left[-N\left(\lambda_r \mathcal{L}^{-1}(\lambda_r) + \ln\frac{\mathcal{L}^{-1}(\lambda_r)}{\sinh\mathcal{L}^{-1}(\lambda_r)}\right)\right], \tag{3.18}$$

where $\mathcal{L}^{-1}(\lambda_r)$ is the inverse Langevin function of the relative stretch $\lambda_r = \frac{\lambda}{\sqrt{N}} \in [0, 1)$ normalized with respect to the extensibility limit $\sqrt{N}$ characterized by the number of segments N. The probability density function for the tube-like constraint in the

sense of [33, 76] is given as

$$p_c(\nu) = p_0 \exp\left[-\alpha \left(\frac{r_0}{d_0}\right)^2 \nu^{-1}\right], \tag{3.19}$$

where $r_0 = \sqrt{N}l$ is the mean end-to-end distance of the chain, d_0 is the tube diameter, α is a shape constant and $\nu^{-1} = (d_0/d)^2$ is the tube areal contraction and $\nu = (d/d_0)^2$ is the tube areal stretch. Incorporation of (3.18) and (3.19) into (3.16) leads to the free energy functions corresponding to the free-chain

$$\psi_f(\lambda) = Nk_B\theta\left(\lambda_r\mathcal{L}^{-1}(\lambda_r) + \ln\frac{\mathcal{L}^{-1}(\lambda_r)}{\sinh\mathcal{L}^{-1}(\lambda_r)}\right) + \psi_0 \tag{3.20}$$

and the tube-like constraint

$$\psi_c(\nu) = \alpha k_B\theta N\left(\frac{l}{d_0}\right)^2 \nu^{-1} + \psi_0, \tag{3.21}$$

respectively. The key issue in the modeling of macroscopic response of a polymer network lies in the non-affine mean-kinematic variables with the affine macro-kinematic variables. Within this context, the macroscopic free energy functions can be additively split into

$$\Psi^e(\boldsymbol{g}, \boldsymbol{F}) := \Psi_f^e(\boldsymbol{g}, \boldsymbol{F}) + \Psi_c^e(\boldsymbol{g}, \boldsymbol{F}) \tag{3.22}$$

the free-chain and tube constraint parts read

$$\Psi_f^e(\boldsymbol{g}, \boldsymbol{F}) = \langle n\psi_f(\bar{\lambda})\rangle \quad \text{and} \quad \Psi_c^e(\boldsymbol{g}, \boldsymbol{F}) = \langle n\psi_c(\bar{\nu}^{-1})\rangle \quad \text{with} \tag{3.23}$$

with

$$\langle(\bullet)\rangle = \frac{1}{|\mathcal{V}|}\int_{\mathcal{V}}(\bullet)dV, \tag{3.24}$$

where n is the volume-specific chain density and the $\bar{\lambda}$ and $\bar{\nu}^{-1}$ are the micro-stretch and the micro-tube areal contraction, respectively. The homogenized response of the free energy of the macro-continuum can be assumed to have the following simple form

$$\langle n\psi_f(\bar{\lambda})\rangle = n\psi_f(\lambda_n) \quad \text{and} \quad \langle n\psi_c(\bar{\nu}^{-1})\rangle = n\psi_c(\nu_n) \tag{3.25}$$

in terms of the average kinematic quantities λ_n and ν_n, see Fig. 3.3. At this point, the average network stretch and the tube areal stretch are assumed as

$$\lambda_n = \sqrt[2]{\frac{\lambda_1^2 + \lambda_2^2 + \lambda_3^2}{3}} = \sqrt[2]{\frac{I_1}{3}} \quad \text{and} \quad \nu_n = \sqrt[3]{\frac{\nu_1^2 + \nu_2^2 + \nu_3^2}{3}} = \sqrt[3]{\frac{I_2}{3}}. \tag{3.26}$$

Herein, the network stretch is the mean-square root average of the principal stretches λ_i in the sense of [32]. The mean non-affine tube areal contraction ν_n of the polymer network in constraint environment is linked to the macroscopic areal stretches in terms of $(3.26)_2$. As a result, the free-chain and the tube-constraint part of the macroscopic free energy function for the extended eight-chain model read

$$\Psi_f^e(\boldsymbol{g}, \boldsymbol{F}) = \mu N \left(\lambda_r \mathcal{L}^{-1}(\lambda_r) + \ln \frac{\mathcal{L}^{-1}(\lambda_r)}{\sinh \mathcal{L}^{-1}(\lambda_r)} \right), \text{ and} \qquad (3.27)$$

$$\Psi_c^e(\boldsymbol{g}, \boldsymbol{F}) = \mu_c(\nu_n - 1), \qquad (3.28)$$

where $\lambda_r = \lambda_n/\sqrt{N}$ represents the relative average network stretch. The shear modulus $\mu = nk_B\theta$ is associated with the free-chain response and the $\mu_c = \alpha(l/d_0)^2 nk_B\theta$ is associated with the tube constraint part.
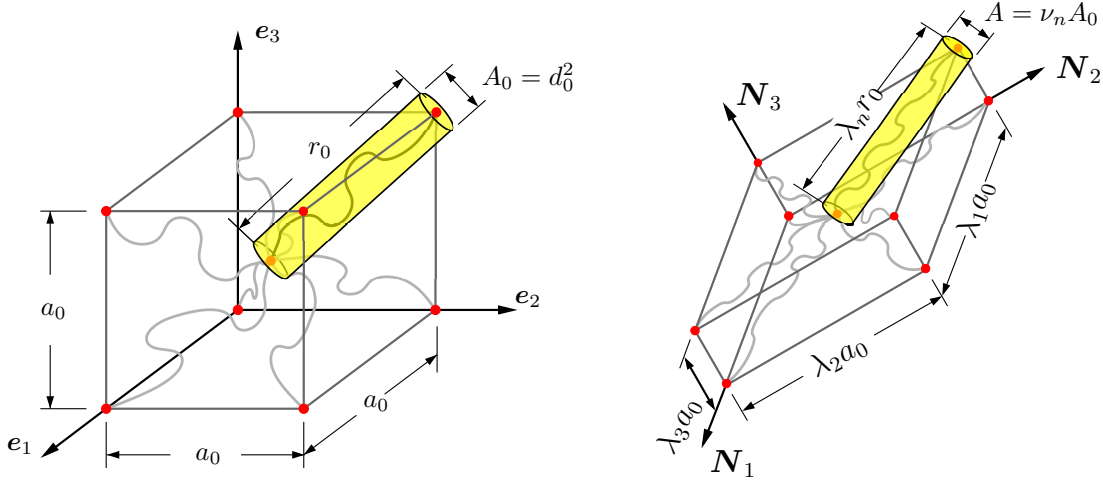
Figure 3.3: Idealization of the rubber network by eight-chain model and the linkage between macroscopic stretches with mean streches of the representative chain, respectively. $\boldsymbol{N}_i$ for $i = \{1, 2, 3\}$ represent the eigenvectors of the right Cauchy-Green tensor, whereas λ_i are the principle stretches, i.e. $\boldsymbol{C} = \sum_{i=1}^3 \lambda_i^2 \boldsymbol{N}_i \otimes \boldsymbol{N}_i$.

3.2.1.2 Compressible extended eight-chain model

The specific form of the compressible eight-chain model can be descibed as follows

$$\Psi^e(J, I_1) = \frac{\chi}{4}[(\ln J)^2 + (J-1)^2] - \frac{\mu}{3}\frac{3N-1}{N-1}\ln J$$

$$+ \mu N \left(\lambda_r \mathcal{L}^{-1}(\lambda_r) + \ln \frac{\mathcal{L}^{-1}(\lambda_r)}{\sinh \mathcal{L}^{-1}(\lambda_r)} \right), \qquad (3.29)$$

where $\chi = \kappa - \frac{2}{3}\mu$ and μ are the first Lamé constant and the shear modulus, respectively. The second expression in the free energy function is the normalization term that enforces $\boldsymbol{\tau}^e = \mathbf{0}$ at undeformed state. The stress expression for the compressible eight-chain model reads

$$\boldsymbol{\tau}^e = 2\partial_{\boldsymbol{g}}\Psi^e(J, I_1) = \left[\frac{\chi}{2}\left(\ln J + J(J-1)\right) - \tilde{\mu}\right]\boldsymbol{g}^{-1} + \hat{\mu}(\lambda_n)\boldsymbol{b}\,, \qquad (3.30)$$

where the two terms related to the shear modulus are given as

$$\tilde{\mu} = \frac{\mu}{3}\frac{3N-1}{N-1} \qquad \text{and} \qquad \hat{\mu}(\lambda_n) = \frac{\mu}{3}\frac{3N-\lambda_n^2}{N-\lambda_n^2}\,. \qquad (3.31)$$

For a Gaussian network where the number of segments approaches infinity, i.e. $N \to \infty$, the parameters simplify to $\hat{\mu} \to \mu$ and $\tilde{\mu} \to \mu$ in (3.31) so that one recovers the compressible neo-Hookean model. Advancing a step forward from (3.29), an extension to compressible eight-chain model can be achieved

$$\Psi^e(\boldsymbol{g}, \boldsymbol{F}) = \Psi_v^e(\boldsymbol{g}, \boldsymbol{F}) + \Psi_f^e(\boldsymbol{g}, \boldsymbol{F}) + \Psi_c^e(\boldsymbol{g}, \boldsymbol{F}) = \tilde{\Psi}_v^e(J) + \tilde{\Psi}_f^e(\lambda_r) + \tilde{\Psi}_c^e(\nu)\,, \quad (3.32)$$

in conjunction with (3.28). Therein, the purely volumetric expression for the extended eight-chain model reads

$$\Psi_v^e(\boldsymbol{g}, \boldsymbol{F}) = \tilde{\Psi}_v^e(J) = \frac{\chi}{4}[(\ln J)^2 + (J-1)^2] - \frac{\mu}{3}\frac{3N-1}{N-1}\ln J - \frac{4}{9}\mu_c \ln J\,, \quad (3.33)$$

in which the second and the third expressions are added in order to normalize the stresses at undeformed configuration. Then, the stress expression for the compressible extended eight-chain model is recast into the following form,

$$\boldsymbol{\tau}^e = 2\partial_{\boldsymbol{g}}\Psi^e(\boldsymbol{g}, \boldsymbol{F}) = \hat{\kappa}(J)\boldsymbol{g}^{-1} + \hat{\mu}(\lambda_n)\boldsymbol{b} + \frac{2}{9}\frac{\mu_c}{\nu_n^2}(I_1\boldsymbol{b} - \boldsymbol{b}^2)\,, \qquad (3.34)$$

where

$$\hat{\kappa}(J) = \frac{\chi}{2}\left(\ln J + J(J-1)\right) - \tilde{\mu}, \qquad (3.35)$$

$$\tilde{\mu} = \frac{\mu}{3}\frac{3N-1}{N-1} + \frac{4}{9}\mu_c\,, \quad \text{and} \qquad (3.36)$$

$$\hat{\mu}(\lambda_n) = \frac{\mu}{3}\frac{3N-\lambda_n^2}{N-\lambda_n^2}\,. \qquad (3.37)$$

The first expression in the stress equation (3.34) is the purely volumetric part, whereas the latter two expressions are due to free chain response and the tube constraint, respectively. For various volumetric free energy functions and their implementation into fnite element method in the quasi-incompressible setting, we refer to KADAPA & HOSSAIN [119].

3.2.2 Non-equilibrium part of the constitutive model

In view of (3.14), the non-equilibrium part of the constitutive response can be described as follows

$$\boldsymbol{\tau}^{ne} := 2\partial_{\boldsymbol{g}}\Psi(\boldsymbol{g}, \boldsymbol{F}^e) = \sum_{k=1}^{n} \hat{\boldsymbol{\tau}}_k^{ne} \quad \text{and} \quad \boldsymbol{S}^{ne} := 2\partial_{\boldsymbol{C}^e}\Psi^{ne}(\boldsymbol{C}^e) = \sum_{k=1}^{n} \hat{\boldsymbol{S}}_k^{ne}. \quad (3.38)$$

Therein, the individual overstress expression for each Maxwell element is given by

$$\hat{\boldsymbol{\tau}}_k^{ne} = 2\partial_{\boldsymbol{g}}\psi_k^{ne}(\boldsymbol{g}, \boldsymbol{F}_k^e) \quad \text{and} \quad \hat{\boldsymbol{S}}_k^{ne} = 2\partial_{\boldsymbol{C}^e}\psi_k^{ne}(\boldsymbol{C}_k^e), \quad (3.39)$$

according to the rheology illustrated in Fig 3.2. In the following sub-section, we will elucidate the individual contributions arisen from the particular selection of the free energy function $\psi_k^{ne}(\boldsymbol{g}, \boldsymbol{F}_k^e)$ in the sense of the Kirchhoff stress $\hat{\boldsymbol{\tau}}_k^{ne}$. Before giving an account of the constitutive modeling of the non-equilibrium response, we underline that the subscript k reflecting the particular Maxwell branch in the rheological structure hereafter drops out of the relevant equations, e.g., $\psi_k^{ne}(\boldsymbol{g}, \boldsymbol{F}_k^e)$, in order not to make the expressions too complicated. In the sequel, the effect of the tube constraint effect on the non-equilibrium response of the rubber network is neglected. The compressible eight-chain model for a single nonlinear elastic spring part of the Maxwell branch as follows,

$$\begin{aligned}
\Psi^{ne}(J^e, I_1^e) &= \frac{\chi^v}{4}\left[\ln J^e + (J^e - 1)^2\right] - \frac{\mu^v}{3}\frac{3N^v - 1}{N^v - 1}\ln J^e \\
&\quad + \mu^v N^v \left(\lambda_r^e \beta(\lambda_r^e) + \ln\frac{\beta(\lambda_r^e)}{\sinh\beta(\lambda_r^e)}\right).
\end{aligned} \quad (3.40)$$

Therein, $\lambda_n^e = \sqrt{I_1^e/3}$ and $\lambda_r^e = \sqrt{I_1^e/3N^v}$ denote the network and the relative network stretches for the non-equilibrium deformations, respectively. $\beta = \mathcal{L}^{-1}(\lambda_r^e)$ is the inverse Langevin function, μ^v is the shear modulus of the non-equilibrium network, N^v is the number of segments of the chains entangled around obstacles. Accordingly, the Kirchhoff stress expression for the compressible eight-chain model is

$$\hat{\boldsymbol{\tau}}^{ne} = 2\partial_{\boldsymbol{g}}\psi^{ne}(J^e, I_1^e) = \left[\frac{\chi^v}{2}\left(\ln J^e + J^e(J^e - 1)\right) - \tilde{\mu}^v\right]\boldsymbol{g}^{-1} + \hat{\mu}^v(\lambda_n^e)\boldsymbol{b}^e, \quad (3.41)$$

where the two terms related to the shear modulus read

$$\tilde{\mu}^v = \frac{\mu^v}{3}\frac{3N^v - 1}{N^v - 1} \quad \text{and} \quad \hat{\mu}^v(\lambda_n^e) = \frac{\mu^v}{3}\frac{3N^v - \lambda_n^{e2}}{N^v - \lambda_n^{e2}}. \quad (3.42)$$

3.2.3 Thermodynamical consistency

The second axiom of thermodynamics restricts the proposed model by the so-called dissipation inequality

$$\mathscr{D} := \mathscr{P} - \dot{\Psi} \geq 0 \quad \text{with} \quad \mathscr{P} := \boldsymbol{S} : \frac{1}{2}\dot{\boldsymbol{C}} = \boldsymbol{\tau} : \boldsymbol{d} , \tag{3.43}$$

being the stress power term. The reduced form of the dissipation inequality reads

$$\mathscr{D}_{red} = \hat{\boldsymbol{\tau}}^{ne} : \tilde{\boldsymbol{d}}^{v} \geq 0 . \tag{3.44}$$

The thermodynamical consistency is satisfied for the non-negative dissipation $\mathscr{D}_{red}$. The evolution equation for the viscous rate of deformation tensor $\tilde{\boldsymbol{d}}^{v}$ must *a priori* satisfy the inequality (3.44).

3.2.4 Relaxation kinetics of a single chain
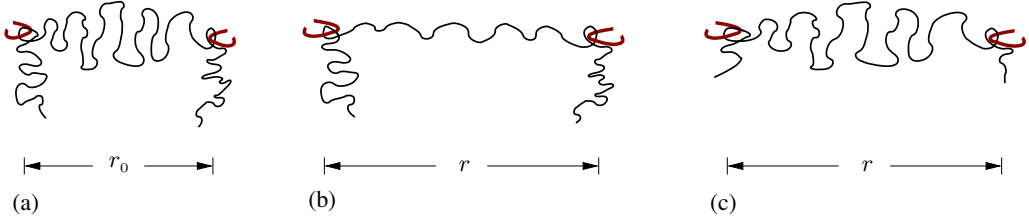
Figure 3.4: Stretch and relaxation of a single chain entangled around an obstacle: (a) undeformed equilibrium state, (b) non-equilibrium deformed state after rapid stretch, (c) deformed and fully relaxed state.

In this part, we elucidate the relaxation kinetics of a single free chain [120]. To this end, we revisit the relaxation kinetics of a single chain entangled around an obstacle at both sides as depicted in Fig. 3.4. In Fig. 3.4(a), a single chain entangled around obstacles at both ends is shown at rest. The end-to-end distance is given by $r_0 = \sqrt{N_0}\hat{l}$ where N_0 is the number of segments between the two obstacles and $\hat{l}$ denotes the length of a monomer unit. If the polymer chain is instantaneously stretched, see Fig. 3.4(b), it elongates and attains a more ordered conformation decreasing its entropy and increasing the free energy, while the internal energy of the chain is kept

41

constant, see TRELOAR [27] (p. 25). The stretching of the chain triggers the movement of the free ends of the chains and they retract in combination of reptational and Brownian motion. Hence, the length of the polymer chain portion lying between the obstacles elongates until the most favorable state, i.e. $r = \sqrt{N_\infty}\hat{l}$, is reached. Fig. 3.4(c) shows not only the deformed but also the fully relaxed state in this case with the same end-to-end distance r. Then, the number of segments at the fully relaxed state reads

$$N_\infty = \bar{\lambda}^2 N_0 \quad \text{where} \quad \bar{\lambda} = \frac{r}{r_0} . \tag{3.45}$$

Recall that unlike N_0, which is a material constant, N_∞ is variable dependent on the instantaneous stretch level $\bar{\lambda}$. Let us consider an intermediate step between rapid deformation as seen in Fig. 3.4(b) and fully relaxed state as indicated in Fig. 3.4(c). We define an end-to-end distance $\bar{r}(t) = \sqrt{N(t)}\hat{l}$ which is probabilistically the most preferred state upon removal of the load maintaining the end-to-end distance r at time t. In a deformation driven state, $\bar{\lambda}$ is given and can be decomposed into elastic and inelastic (viscous) parts as follows

$$\bar{\lambda} = \frac{r}{r_0} = \frac{r}{\bar{r}(t)} \frac{\bar{r}(t)}{r_0} = \lambda^e(t)\lambda^v(t) \tag{3.46}$$

where

$$\lambda^e(t) := \frac{r}{\bar{r}(t)} \quad \text{and} \quad \lambda^v(t) := \frac{\bar{r}(t)}{r_0} . \tag{3.47}$$

Initially at time $t = 0$, the end-to-end distance reads $\bar{r}(0) = r_0$, leading to $\lambda_e(0) = \bar{\lambda}$ and $\lambda_v(0) = 1$. However, at the fully relaxed state at time $t = \infty$, the end-to-end distance reads $\bar{r}(\infty) = r$, leading to $\lambda_e(\infty) = 1$ and $\lambda_v(\infty) = \bar{\lambda}$. For the evolution of the chain length in-between the two obstacles, we adopt a generic ordinary differential equation (ODE), i.e.

$$\dot{N}(t) = \frac{1}{\tau} [N_\infty - N(t)] , \tag{3.48}$$

where τ designates the relaxation time. Then, the solution of the ODE reads

$$N(t) = (N_\infty - N_0) \left[1 - \exp\left(\frac{-t}{\tau}\right)\right] + N_0 . \tag{3.49}$$

Next, we substitute (3.49) into $(3.46)_3$ and consider the rate of the viscous stretch $\lambda^v(t)$ with respect to time. This, upon some simple mathematical manipulations, lead to the following

$$\dot{\lambda}^v(t) = \frac{d}{dt}\left(\frac{\bar{r}(t)}{r_0}\right) = \frac{d}{dt}\left(\frac{\sqrt{N(t)}\hat{l}}{\sqrt{N_0}\hat{l}}\right) = \frac{1}{2\tau}\frac{1}{\sqrt{N_0}}\left(\frac{N_\infty}{\sqrt{N(t)}} - \sqrt{N(t)}\right) . \tag{3.50}$$

Substitution of the relations stated below

$$\lambda^e = \frac{r}{\bar{r}(t)} = \frac{\sqrt{N_\infty}}{\sqrt{N(t)}} \quad \text{and} \quad \sqrt{N_\infty} = \bar{\lambda}\sqrt{N_0} \tag{3.51}$$

into (3.50), we readily obtain the rate equation

$$\dot{\lambda}^v = \frac{1}{2\tau}\bar{\lambda}\left(\lambda^e - \frac{1}{\lambda^e}\right) = \frac{1}{2\tau}\lambda^v\left(\lambda^{e2} - 1\right) . \tag{3.52}$$

In order to comply with the large-strain kinematics in the Eulerian setting, the one-dimensional logarithmic counterpart of the rate of deformation tensor is derived as follows,

$$\boxed{\dot{\epsilon}^v = \frac{\dot{\lambda}^v}{\lambda^v} = \dot{\gamma}_0\left(\lambda^{e2} - 1\right) .} \tag{3.53}$$

3.2.5 Evolution equation

Consistent with the reduced dissipation postulate (3.44), we propose an evolution for the inelastic rate of the deformation tensor in the current configuration

$$\tilde{\boldsymbol{d}}^v := \dot{\gamma}\mathbf{N} , \tag{3.54}$$

where $\dot{\gamma}$ denotes the effective creep rate. Note that the thermodynamical consistency (3.44) is satisfied for $\dot{\gamma} \geq 0$. The flow direction is determined by the non-equilibrium Kirchhoff stress

$$\mathbf{N} = \frac{\boldsymbol{\tau}^{ne}}{\|\boldsymbol{\tau}^{ne}\|} \quad \text{with} \quad \|\boldsymbol{\tau}^{ne}\| := \sqrt{\boldsymbol{\tau}^{ne} : \boldsymbol{\tau}^{ne}} . \tag{3.55}$$

Nonlinear viscoelasticity is an energy activated process. In order to take this fact into account and to reconcile the finite viscoelasticity with the relaxation kinetics derived above, an additional term $(\tau^{ne}/\hat{\tau})^m$ is added to the expression in (3.53). Therein, the specific norm of the non-equilibrium stress τ^{ne} is described as follows

$$\tau^{ne} = \frac{\|\boldsymbol{\tau}^{ne}\|}{\sqrt{2}}. \tag{3.56}$$

In what follows, we also replace the λ^e expression for a single chain by the network stretch $\lambda_n^e = \sqrt{I_1^e/3}$ of the eight-chain model where $I_1^e = \operatorname{tr}\boldsymbol{C}^e$. Finally, we end up with the following function for the effective creep rate

$$\boxed{\dot{\gamma} := \dot{\gamma}_0[\lambda_n^{e2} - 1]\left(\frac{\tau^{ne}}{\hat{\tau}}\right)^m .} \tag{3.57}$$

In the above expression the relaxation time $1/2\tau$ is replaced by the creep rate constant $\dot{\gamma}_0 > 0$ for the sake of convenience. Note that the term $m \geq 1$ controls the energy-activated relaxation and leads to viscoplastic material response for high values. The expression $\hat{\tau}$ is used merely for normalization purposes and assumed to be $\hat{\tau} = 1$ [MPa] in the subsequent treatments. In the end, we emphasize that the nonlinear viscous flow stated in (3.57) is governed by one more additional material parameter in comparison to the that of the finite linear viscoelasticity and reflects from the continuum point of view the behavior of a single dashpot in the Maxwell element as depicted in Fig. 3.2. Recall that replacing the term $\dot{\gamma}_0[\lambda_n^{e2} - 1] \rightarrow \dot{\gamma}_0$ and taking $m = 1$, we obtain the classical multiplicative finite viscoelasticity in the sense of REESE & GOVINDJEE [60]. Moreover, taking $N \rightarrow \infty$, one obtains the simplest finite viscoelasticity formulation in the geometrically nonlinear setting based on multiplicative decomposition of the deformation gradient into elastic and viscous parts.

REMARK: The proper prediction of viscous flow direction requires $\dot{\gamma}_0[\lambda_n^{e2} - 1] \geq 0$. In incompressible rubber viscoelasticity, the condition is always satisfied since the network stretch λ_n^e is always greater than unity $\lambda_n^{e2} \geq 1$. However, for slightly compressible elastomers, under purely hydrostatic pressure loading, it is possible to have $\lambda_n^{e2} \leq 1$. To resolve this issue, the term $[\lambda_n^{e2} - 1]$ must be replaced by $|\lambda_n^{e2} - 1|$ in the evolution equation (3.57) for the analysis of compressible elastomers.

3.3   Algorithmic setting for the constitutive model

In this section, the algorithmic setting of the model suitable for a finite element implementation will be discussed. In particular, the algorithmic framework for the Eulerian stresses and moduli terms of the equilibrium and non-equilibrium responses will be established. Furthermore, we will propose an efficient implicit update for the principle elastic stretches of the non-equilibrium Maxwell branches, conceptually following the references [120, 60, 62].

In a time-discrete interval, i.e. $\Delta t = t^{n+1} - t^n$, the current stresses and the tangent expressions need to be obtained where Δt stands for the time-increment. The time-

discrete counterpart of the continuous expression in (3.10) reads

$$\Delta\boldsymbol{\tau} = \mathbb{C}_{\text{algo}} : \frac{1}{2}\pounds_{\Delta\boldsymbol{\varphi}}\boldsymbol{g} + \nabla_x(\Delta\boldsymbol{\varphi})\,\boldsymbol{\tau} + \boldsymbol{\tau}\,\nabla_x^T(\Delta\boldsymbol{\varphi}) \tag{3.58}$$

where $\nabla_x(\cdot)$ represents the spatial gradient of the term considered. Therein, $\mathbb{C}_{\text{algo}}$ is the total algorithmic moduli and must be consistently derived for the accurate and quadratically convergent nonlinear finite element analysis based on global iterative solution algorithms, e.g., the Newton-Raphson method. Subsequently, the total algorithmic moduli term is also additively decomposed into equilibrium and non-equilibrium parts as follows

$$\mathbb{C}_{\text{algo}} := \mathbb{C}^e + \mathbb{C}_{\text{algo}}^{ne}. \tag{3.59}$$

3.3.1 Stress and moduli terms for the elastic part

The computation of the equilibrium Kirchhoff stress in (3.34) requires the current value of $\boldsymbol{b}$ at time $t = t_{n+1}$ which is readily obtained at each iteration in the global iterative solution algorithm. In the subsequent treatment, we focus on the elasticity moduli $\mathbb{C}^e$ in (3.59) and define

$$\mathbb{C}^e := 4\partial_{\boldsymbol{gg}}^2\Psi^e(J, I_1, I_2) \tag{3.60}$$

which gives rise to the following explicit form of the equilibrium tangent moduli through the particular form of the free energy (3.32),

$$\begin{aligned}
\mathbb{C}^e &= (\hat{s}^e + \hat{p}^e)\boldsymbol{g}^{-1} \otimes \boldsymbol{g}^{-1} - 2\hat{p}^e\mathbb{I} + \hat{n}^e\boldsymbol{b} \otimes \boldsymbol{b} \\
&+ \hat{f}^e(I_1\boldsymbol{b} - \boldsymbol{b}^2) \otimes (I_1\boldsymbol{b} - \boldsymbol{b}^2) + \hat{g}^e(\boldsymbol{b} \otimes \boldsymbol{b} - \mathbb{I}_{\boldsymbol{b}}).
\end{aligned} \tag{3.61}$$

Therein, the terms in regard to the Jacobian J reads

$$\begin{aligned}
\hat{p}^e &:= J\frac{\partial^2\Psi^e}{\partial J^2} = \frac{\chi}{2}\left[\ln J + J(J-1)\right] - \tilde{\mu}, \text{ and} \\
\hat{s}^e &:= J^2\frac{\partial^2\Psi^e}{\partial J^2} = \frac{\chi}{2}\left[J^2 - \ln J + 1)\right] + \tilde{\mu}\,,
\end{aligned} \tag{3.62}$$

while the terms associated with I_1 and I_2 are written as

$$\hat{n}^e = \frac{4\mu}{9N}\frac{1}{(1-\lambda_r^2)^2}\,, \qquad \hat{f}^e = -\frac{8\mu_c}{81}\frac{1}{\nu_n^5} \quad \text{and} \quad \hat{g}^e = \frac{4\mu_c}{9}\frac{1}{\nu_n^2}\,. \tag{3.63}$$

45

The fourth-order tensor $\mathbb{I}_b$ is simply the push-forward of the fourth-order identity tensor $\mathbb{I}$ such that

$$\mathbb{I}^{ijkl} = \frac{1}{2}\left(\delta^{ik}\delta^{jl} + \delta^{il}\delta^{jk}\right) \quad \text{and} \quad \mathbb{I}_b{}^{ijkl} = \frac{1}{2}\left(b^{ik}b^{jl} + b^{il}b^{jk}\right) . \tag{3.64}$$

In the above equation, the inverse Langevin function is computed by Padé approximation $\mathcal{L}^{-1}(\lambda_r) \approx \lambda_r(3 - \lambda_r^2)/(1 - \lambda_r^2)$ proposed by COHEN [121].

3.3.2 Stresses and moduli terms for the viscous part

Before we start our discussion, it needs to be mentioned that the non-equilibrium stress and moduli terms will be calculated for a single Maxwell element, see Fig. 3.2, in order to rid the mathematical expressions of extra subscript k. The computation of the non-equilibrium Kirchhoff stress in (3.41) requires the current value of $\boldsymbol{b}^e$ at time $t = t_{n+1}$. The computation of $\boldsymbol{b}^e$ is contingent on the algorithmic treatment of the evolution equation (3.54) which will be elucidated in the upcoming sub-sections.

3.3.2.1 Integration of the evolution equation:

In this sub-section, we begin with the introduction of the identity forming the basis of the subsequent development, that is

$$-\frac{1}{2}\pounds_\nu \boldsymbol{b}^e \cdot \boldsymbol{b}^{e-1} = \tilde{\boldsymbol{d}}^v . \tag{3.65}$$

The integration of the evolution equation (3.54) is based on the operator split of the material time derivative of $\boldsymbol{b}_e$ into an elastic predictor ($\mathcal{E}$) and an inelastic corrector step ($\mathcal{I}$) such that

$$\dot{\boldsymbol{b}}^e := \underbrace{\boldsymbol{l}\boldsymbol{b}^e + \boldsymbol{b}^e\boldsymbol{l}^T}_{\mathcal{E}} + \underbrace{\pounds_\nu \boldsymbol{b}^e}_{\mathcal{I}} . \tag{3.66}$$

Both in (3.65) and (3.66) the Lie derivative of the elastic Finger tensor $\boldsymbol{b}^e$ is given which can be defined as follows

$$\pounds_\nu \boldsymbol{b}^e := \boldsymbol{F}\frac{d}{dt}\left(\boldsymbol{C}^{v-1}\right)\boldsymbol{F}^T . \tag{3.67}$$

During the elastic predictor step $\mathcal{E}$ (elastic trial step), $d(\boldsymbol{C}^{v-1})/dt$ is equal to zero. Therefore,

$$\text{Elastic predictor (trial step)} \quad \mathcal{E}: \quad \boldsymbol{C}_{tr}^{v-1} = \boldsymbol{C}_{t_n}^{v-1} \longrightarrow \boldsymbol{b}_{tr}^e = \boldsymbol{F}\boldsymbol{C}_{t_n}^{v-1}\boldsymbol{F}^T. \tag{3.68}$$

It should be highlighted that the subscript denoting the current time step t_{n+1} hereinafter drops out of the expressions for convenience. The merit of this proposal is to circumvent the rate of inelastic metric in computation of the consistent tangent moduli. Afterwards, we focus on the inelastic corrector step $\mathcal{I}$. Here, the spatial velocity gradient $\boldsymbol{l}$ is set to zero yielding $\dot{\boldsymbol{b}}^e = \mathcal{L}_\nu \boldsymbol{b}^e$. Inserting this result into (3.65) and substituting the evolution equation proposed in (3.54) for $\tilde{\boldsymbol{d}}^v$, we obtain the following expression,

$$\text{Inelastic corrector step } \mathcal{I}: \quad \dot{\boldsymbol{b}}^e = -2\dot{\gamma}\mathbf{N}\boldsymbol{b}^e_{tr} \,, \tag{3.69}$$

for the evolution equation for the inelastic corrector step. The interested reader is referred to references [120, 62], regarding integration of the equations [3.68,3.69] in a time-discrete setting.

3.3.2.2 Algorithmic moduli for the non-equilibrium part:

In this part, we will set up a closed-form expression for the consistent tangent moduli for the non-equilibrium (viscous) part. The spectral decomposition of the trial elastic deformation yields

$$\boldsymbol{F}^e_{tr} = \sum_{a=1}^{3} \lambda^e_{a,\,tr} \, \boldsymbol{n}_a \otimes \boldsymbol{N}^a \,. \tag{3.70}$$

Subsequently, we introduce a fictitious second Piola-Kirchhoff stress tensor

$$\tilde{\boldsymbol{S}}^{ne} := \boldsymbol{F}^{e-1}_{tr} \boldsymbol{\tau}^{ne} \boldsymbol{F}^{e-T}_{tr} \quad \text{where} \quad \tilde{\boldsymbol{S}}^{ne} = \sum_{a=1}^{3} \tilde{s}_a \boldsymbol{N}^a \otimes \boldsymbol{N}^a \,, \tag{3.71}$$

in the intermediate configuration. In $(3.71)_2$, the principal value of the fictitious second Piola-Kirchhoff stress reads $\tilde{s}_a = \tau_a / \lambda^{e2}_{a,\,tr}$. With the definition $(3.71)_1$ at hand, the incremental rate equation can be defined as follows

$$\Delta \tilde{\boldsymbol{S}}^{ne} = \mathbb{C}^{ne}_{\text{algo}} : \Delta \boldsymbol{C}^e_{tr} \quad \text{where} \quad \mathbb{C}^{ne}_{\text{algo}} = 2\partial_{\boldsymbol{C}^e_{tr}} \tilde{\boldsymbol{S}}^{ne} \,. \tag{3.72}$$

Next, we consider $(3.72)_2$ via exploiting $(3.71)_2$ and obtain the moduli expression as follows

$$\mathbb{C}^{ne}_{\text{algo}} = \sum_{a=1}^{3} \sum_{b=1}^{3} \frac{c_{ab} - 2\tau_a \delta_{ab}}{\lambda^{e2}_{a,\,tr} \lambda^{e2}_{b,\,tr}} \boldsymbol{N}^a \otimes \boldsymbol{N}^a \otimes \partial_{\boldsymbol{C}^e_{tr}} (\lambda^{e2}_{b,\,tr}) \tag{3.73}$$

$$+ \sum_{a=1}^{3} \frac{2\tau_a}{\lambda^{e2}_{a,\,tr}} \partial_{\boldsymbol{C}^e_{tr}} (\boldsymbol{N}^a \otimes \boldsymbol{N}^a) \,, \tag{3.74}$$

47

along with the respective partial derivatives with respect to the trial elastic right Cauchy-Green tensor,

$$\partial_{\boldsymbol{C}^e_{tr}}(\lambda^{e^2}_{b,tr}) = \boldsymbol{N}^b \otimes \boldsymbol{N}^b$$

$$\partial_{\boldsymbol{C}^e_{tr}}(\boldsymbol{N}^a \otimes \boldsymbol{N}^a) = \sum_{b \neq a}^{3} \frac{1}{2(\lambda^{e^2}_{a,tr} - \lambda^{e^2}_{b,tr})}(\mathbb{G}^{ab} + \mathbb{G}^{ba}), \qquad (3.75)$$

where we have introduced $\mathbb{G}^{ab}_{IJKL} := M^a_{IK} M^b_{JL} + M^a_{IL} + M^a_{JK}$. This expression in its turn consists of the following

$$\boldsymbol{M}^a := \boldsymbol{N}^a \otimes \boldsymbol{N}^a \qquad \text{where} \qquad M^a_{IJ} := N^a_I N^a_J. \qquad (3.76)$$

Upon replacing the derivatives in (3.74) by $(3.75)_1$ and $(3.75)_2$, we finally obtain the compact definition of the moduli expression in the fictitious intermediate configuration

$$\begin{aligned}
\mathbb{C}^{ne}_{\text{algo}} &= \sum_{a=1}^{3} \sum_{b=1}^{3} \frac{c_{ab} - 2\tau_a \delta_{ab}}{\lambda^{e^2}_{a,tr} \lambda^{e^2}_{b,tr}} \boldsymbol{M}^a \otimes \boldsymbol{M}^b \\
&+ \sum_{a \neq b}^{3} \sum_{b=1}^{3} \frac{\tilde{s}_a - \tilde{s}_b}{2(\lambda^{e^2}_{a,tr} - \lambda^{e^2}_{b,tr})}(\mathbb{G}^{ab} + \mathbb{G}^{ba}). \qquad (3.77)
\end{aligned}$$

CHAPTER 4

FUNDAMENTALS OF THE MULTIPHYSICS PROBLEM

In this chapter we layed out the primary field variables for phase-field modeling of fracture phenomenon and introduced the multi-field problem. First we describe a 1D motivation for phase-field approach, then a 3D extension is achieved. During the chapter, we introduced the idea of separate degradation functions for distortional and dilatational parts of the extended eight-chain model. Next, a Hermitian polynomial based extension for generating suitable degradation functions is discussed. Finally, we have given several simulation results that demonstrates a gradually decreasing Poisson's ratio during the degradation, i.e., showcasing the loss of incompressibility during the fracture.

4.1 Kinematics of the phase–field problem

The problem at hand involves a domain that can change shape, which is represented by the deformation field shown in Figure 4.1(a). If the domain does not change shape, the gradient operator can be represented simply as $\nabla_x(\bullet) = \nabla_X(\bullet) = \nabla(\bullet)$. At a fixed time t, a sharp crack surface topology is defined by a surface integral $\Gamma(d) = \int_\Gamma \mathrm{d}A$ over a two-dimensional solid $\mathcal{B}$, which is denoted by $\Gamma(d) \subset \mathbb{R}^2$. The crack phase-field approach simplifies the task of tracking these discontinuities by approximating the surface integral using a volume integral. This results in a regularized crack surface denoted by $\Gamma_l(d)$, as shown in Figure 4.1(b), such that

$$\Gamma_l(d) = \int_\mathcal{B} \gamma(d, \nabla d)\mathrm{d}V \quad \text{where} \quad \gamma(d, \nabla d) = \frac{1}{2l}(d^2 + l^2 \nabla d \cdot \nabla d), \qquad (4.1)$$

where, the *isotropic crack surface density* function, represented here by $\gamma(d, \nabla d)$, is defined in a way that it satisfies the condition $\gamma(d, \mathbf{Q}\nabla d) = \gamma(d, \nabla d)$, for all possible

49
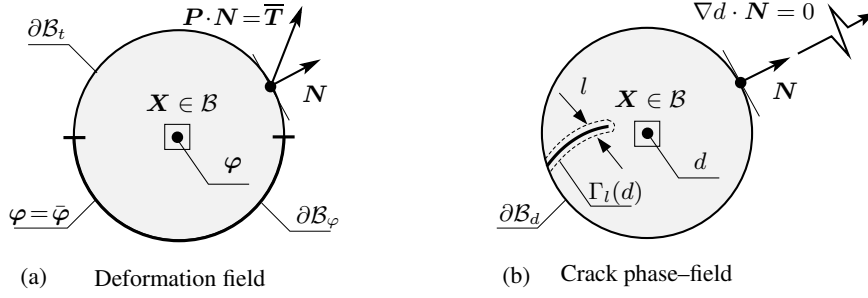
Figure 4.1: Multi-field problem: (a) mechanical problem of deformation along with Dirichlet and Neumann-type boundary conditions, that is $\varphi = \overline{\varphi}$ and $\boldsymbol{P} \cdot \boldsymbol{N} = \overline{\boldsymbol{T}}$, respectively; (b) evolution of the crack phase–field problem with the Neumann-type boundary condition $\nabla d \cdot \boldsymbol{N} = 0$.

rotations and reflections denoted by the tensor variable $\boldsymbol{Q}$ in the orthogonal group $\mathcal{O}(3)$. The parameter l controls the width of the crack. This approximation can be expanded to apply to a range of anisotropic materials as well.

$$\Gamma_l(d) = \int_{\mathcal{B}} \gamma(d, \nabla d) \mathrm{d}V, \quad \text{where} \quad \gamma(d, \nabla d) = \frac{1}{2l}(d^2 + l^2 \nabla d \cdot \nabla d), \qquad (4.2)$$

is the *anisotropic crack surface density* function with the condition $\gamma(d, \boldsymbol{Q}\nabla d) = \gamma(d, \nabla d)$, $\forall \boldsymbol{Q} \in \mathcal{G} \subset \mathcal{O}(3)$, where $\mathcal{G}$ designates a symmetry group as a subset of $\mathcal{O}(3)$.

4.1.1 Euler–Lagrange equations of the phase–field problem

From a purely geometrical perspective, the boundary of the domain under interest can be decomposed into Dirichlet and Neumann-type boundaries such that $\partial\mathcal{B} = \partial\mathcal{B}^d \cup \partial\mathcal{B}^q$ and $\partial\mathcal{B}^d \cap \partial\mathcal{B}^q = \emptyset$. By considering (4.2), we can state the minimization principle as

$$d(\boldsymbol{X}) = \mathrm{Arg} \left\{ \inf_{d \in \mathcal{W}} \Gamma_l(d) \right\}, \qquad (4.3)$$

along with the Dirichlet–type boundary constraint

$$\mathcal{W} = \{ d \mid d(\boldsymbol{X}) \in \mathcal{B} \quad \wedge \quad d = \hat{d} \quad \text{on} \quad \partial\mathcal{B}^d \}. \qquad (4.4)$$

Whilst an already existing crack is given by $\hat{d} = 1$, the intact state is described by $\hat{d} = 0$. Although the boundary value problem admits any meta-states $\hat{d} \in [0,1]$ on

$\partial \mathcal{B}^d$, we confine ourselves for the two ideal states. The principle of minimization is used to derive the Euler-Lagrange equations, which can be expressed as:

$$\frac{1}{l}[d - l^2 \Delta d)] = 0 \quad \text{in } \mathcal{B}, \qquad \nabla d \cdot \boldsymbol{N} = 0 \quad \text{on } \partial \mathcal{B}^q, \tag{4.5}$$

Here, the divergence term serves to interpolate between the intact and ruptured states of the material, and $\boldsymbol{N}$ represents the unit surface normal oriented outward in the reference configuration.

4.2 A framework of diffusive fracture at large strains

In this section the phase-field theory for application of different degradation functions for volumetric and entropic parts are considered. To this end, Hermitian polynomial based degradation functions are proposed. Finally the field equations of the coupled problem are given.

4.2.1 Stored energy functional for the hyperelastic solid

Our focus is on finite elasticity for isotropic solids, which involves the global energy storage functional:

$$E(\boldsymbol{\varphi}, d) = \int_{\mathcal{B}} \Psi(\boldsymbol{F}, d) dV \tag{4.6}$$

This functional is dependent on the deformation field $\boldsymbol{\varphi}$ and the fracture phase field d. The energy storage function Ψ represents the energy stored in the bulk of the solid per unit volume. Assuming fully isotropic constitutive behavior for the degradation of energy due to fracture, the energy storage function can be written as:

$$\boxed{\psi(\boldsymbol{F}, d, \nabla d) = g_v(d)\, \Psi_v(J) + g_f(d)\, \Psi_f(\lambda_n) + g_f(d)\, \Psi_c(\nu_n)\,.} \tag{4.7}$$

Here, the *degradation function* g monotonically decreases with evolving fracture and satisfies the following properties:

$$g'(d) \leq 0 \quad \text{with} \quad g(0) = 1 \,, \quad g(1) = 0 \,, \quad g'(1) = 0 \,. \tag{4.8}$$

The first two conditions correspond to the unbroken and fully-broken states, respectively. The third condition ensures that the energetic fracture force converges to a

51
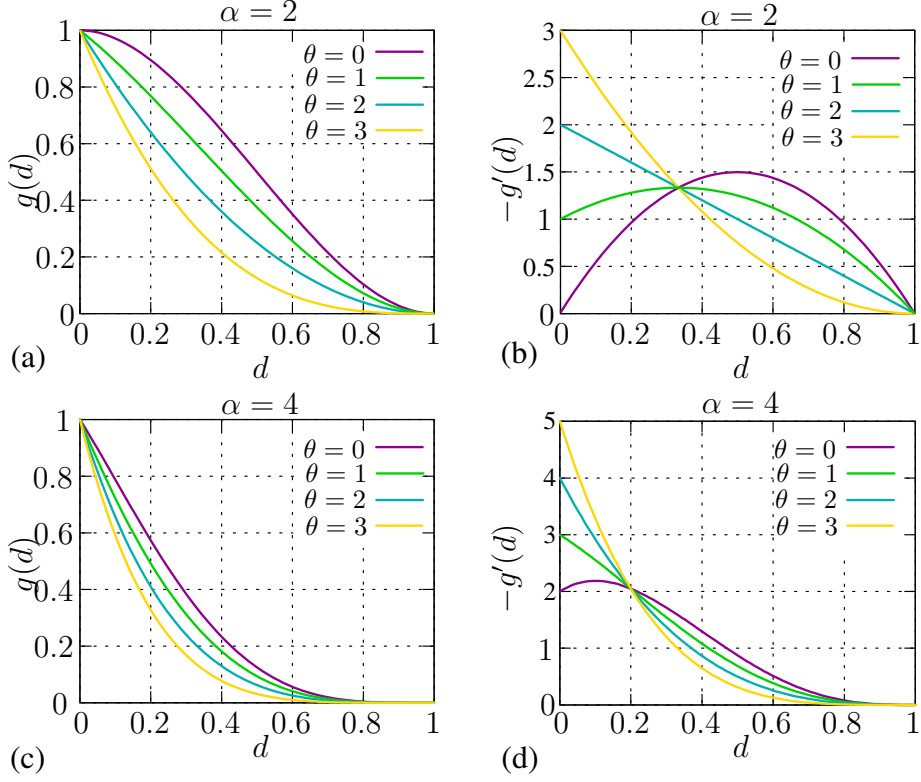
Figure 4.2: (a,c) The proposed degradation function $g(d)$ and (b) its negative derivative $-g'(d)$ for $\alpha = 2$ and various values of θ: (i) [magenta] $\theta = 0$, $g(d) = (1 + 2d)(1 - d)^2$ (ii) [green] $\theta = 1$, $g(d) = (1 + d)(1 - d)^2$, (iii) [blue] $\theta = 2$: $g(d) = (1 - d)^2$, (iv) [golden] $\theta = 3$, $g(d) = (1 - d)^3$; and (d) its negative derivative $-g'(d)$ for $\alpha = 4$ and various values of θ.

finite value if the damage reaches the fully-broken state $d = 1$. A family of admissible functions satisfying these conditions is given by:

$$g(d) = H_1(d) - \theta H_2(d) \tag{4.9}$$

where H_1 and H_2 are defined as:

$$H_1(d) = (1 + 2d)(1 - d)^\alpha \quad \text{and} \quad H_2(d) = d(1 - d)^\alpha \tag{4.10}$$

These expressions describe the degradation function g in terms of two terms, H_1 and H_2, which depend on the damage variable d and constants α and θ.

Therein, $\alpha \geq 2$ and $0 < \theta \leq 3$ is material parameters responsible for (i) the form of the stress degradation upon crack initiation and (ii) transition of the material response

from quasi-incompressible state to compressible state as long as different α and θ values assigned to bulk and shear responses, see Fig. 4.2. Recall that for $\theta = 0$ crack cannot initiate under isochoric/volumetric deformations. The proposed ansatz recovers the original quadratic degration function of MIEHE ET AL. [122] $g(d) = (1-d)^2$ for $\alpha = 2$ and $\theta = 2$, whereas the cubic form $g(d) = (1-d)^2$ in the sense of KUHN ET AL. [123] for $\alpha = 2$ and $\theta = 3$. The proposed functions $H_1(d)$ and $H_2(d)$ are the first two elements of the cubic Hermite splines for $\alpha = 2$, see also BORDEN ET AL. [124]. The power form in the sense of GÜLTEKIN ET AL. [125] is recovered for $\alpha \geq 2$ and $\theta = 2$.

The rate of change of stored energy for a given state of deformation field $\boldsymbol{\varphi}$ and fracture phase field d is defined as the time derivative of the energy storage functional (4.6), which is denoted by $\mathcal{E}(\dot{\boldsymbol{\varphi}}, \dot{d}; \boldsymbol{\varphi}, d)$, that is

$$\mathcal{E}(\dot{\boldsymbol{\varphi}}, \dot{d}; \boldsymbol{\varphi}, d) := \frac{d}{dt} E = \int_{\mathcal{B}} [\boldsymbol{P} : \dot{\boldsymbol{F}} - f \dot{d}] \, dV \qquad (4.11)$$

The stress tensor $\boldsymbol{P}$ is introduced as the derivative of the energy storage function with respect to the deformation field,

$$\boldsymbol{P} := \partial_{\boldsymbol{F}} \psi(\boldsymbol{F}, d) = g_v(d) \boldsymbol{P}_v + g_f(d) \boldsymbol{P}_f + g_c(d) \boldsymbol{P}_c \qquad (4.12)$$

and the energetic force is introduced as the derivative of the energy storage function with respect to the fracture phase field, i.e.,

$$f := -\partial_d \Psi(\boldsymbol{F}, d, \nabla d) = -g_v'(d) \, \Psi_v(J) - g_f'(d) \, \Psi_f(\lambda_n) - g_c'(d) \, \Psi_c(\nu_n) \geq 0 \,. \quad (4.13)$$

The crack evolution is driven by the reference energy $\psi_0(\boldsymbol{F})$, which describes the local intensity of the deformation. The external mechanical loading is defined by the external load power functional $\mathcal{P}(\dot{\boldsymbol{\varphi}})$, which depends on the volume specific body force $\tilde{\boldsymbol{\gamma}}$ and the prescribed surface tractions $\tilde{\boldsymbol{t}}$, and can be written as

$$\mathcal{P}(\dot{\boldsymbol{\varphi}}) = \int_{\mathcal{B}} \tilde{\boldsymbol{\gamma}} \cdot \dot{\boldsymbol{\varphi}} \, dV + \int_{\partial \mathcal{B}_t} \tilde{\boldsymbol{t}} \cdot \dot{\boldsymbol{\varphi}} \, dA \,., \qquad (4.14)$$

4.2.2 Rate-dependent dissipation functional

In order to consider the energy lost in the continuum, the dissipation functional $\mathcal{D}$ is introduced. It is represented as:

$$\mathcal{D}(\dot{d}) = \int_{\mathcal{B}} \mathcal{G}_c [\delta_d \gamma(d, \nabla d)] \, \dot{d} \, dV, \qquad (4.15)$$

Here, $\delta_d\gamma$ represents the variational derivative of the anisotropic volume-specific crack surface γ, and $\mathcal{G}_c$ is referred to as the critical fracture energy. This is consistent with the work of MIEHE ET AL. [122] and GÜLTEKIN ET AL. [126]. The second law of thermodynamics requires that the dissipation functional be non-negative for all possible deformation processes. This means that $\mathcal{D} \geq 0$. This thermodynamic inequality is met by a constitutive dissipation function Φ, which has a positive and convex propensity. This function can be expressed using the principle of maximum dissipation through the following constrained optimization problem:

$$\Phi(\dot{d}; d, \nabla d) = \sup_{\beta \in \mathbb{E}} \beta\dot{d}, \tag{4.16}$$

which can be solved by a Lagrange method that leads to

$$\Phi(\dot{d}; d, \nabla d) = \sup_{\beta, \lambda \geq 0} [\beta\dot{d} - \lambda t_{\mathrm{c}}(\beta; d, \nabla d)], \tag{4.17}$$

Here, β is the local driving force that is dual to $\dot{d}$, and λ is the Lagrange multiplier that enforces the constraint. This has been described in the works of MIEHE AND SCHÄNZEL [96]. Additionally, we have defined the threshold function t_{c} delineating a reversible domain $\mathbb{E}$ such that

$$\mathbb{E}(\beta) = \{\beta \in \mathbb{R} \mid t_{\mathrm{c}}(\beta; d, \nabla d) = \beta - \mathcal{G}_c[\delta_d\gamma(d, \nabla d)] \leq \Psi_{cr}\}. \tag{4.18}$$

The viscous regularization of the rate-independent modality provides stability to the algorithmic setting, which is purely related to numerical calculations. With the aim of achieving this specific goal, a Perzyna-type viscous dissipation functional is presented.

$$\mathcal{D}_\eta(\dot{d}, \beta; d) = \int_{\mathcal{B}} [\beta\dot{d} - \frac{1}{2\eta}\langle t_{\mathrm{c}}(\beta; d, \nabla d)\rangle^2] \mathrm{d}V, \tag{4.19}$$

This functional, denoted by $\mathcal{D}_\eta(\dot{d}, \beta; d)$, incorporates the viscosity parameter η that determines the influence of viscous forces on the rate of change of $\dot{d}$. The functional involves the integral of a combination of terms, including a threshold function t_{c} that filters out positive values, and a ramp function $\langle x \rangle = (x + |x|)/2$. The threshold function defines a reversible domain $\mathbb{E}$, and the functional is expressed as $\Pi_\eta = \mathcal{E} + \mathcal{D}_\eta - \mathcal{P}$, where $\mathcal{E}$ is the elastic energy and $\mathcal{P}$ is the power input. On the basis of the rate-type potential, we propose a viscous extended saddle point principle for the quasi-static process, i.e.

$$\{\dot{\boldsymbol{\varphi}}, \dot{d}, \beta\} = \mathrm{Arg}\left\{\inf_{\dot{\boldsymbol{\varphi}} \in \mathcal{W}_{\dot{\boldsymbol{\varphi}}}} \inf_{\dot{d} \in \mathcal{W}_{\dot{d}}} \sup_{\beta \geq 0} \Pi_\eta\right\}, \tag{4.20}$$

with the admissible domains for the primary state variables

$$\mathcal{W}_{\dot{\varphi}} = \{\dot{\varphi} \mid \dot{\varphi} = \mathbf{0} \quad \text{on} \quad \partial\mathcal{B}_{\varphi}\}, \qquad \mathcal{W}_{\dot{d}} = \{\dot{d} \mid \dot{d} = 0 \quad \text{on} \quad \partial\mathcal{B}_d\}. \qquad (4.21)$$

Evaluating the variation of the potential Π_η we obtain the coupled set of Euler-Lagrange equations for the rate-dependent fracture of an anisotropic hyperelastic solid as

$$\boxed{\begin{aligned} &1\text{: } \text{Div}(\boldsymbol{P}) + \tilde{\boldsymbol{\gamma}} = \boldsymbol{O}, \\ &2\text{: } \beta - f = 0, \\ &3\text{: } \dot{d} - \frac{1}{\eta}\langle t_c(\beta; d, \nabla d)\rangle = 0. \end{aligned}} \qquad (4.22)$$

Substituting f into β, the explicit form of the threshold function t_c recasts the equality $(4.22)_3$ in such a form

$$f = \eta\dot{d} + \mathcal{G}_c\delta_d\gamma(d, \nabla d). \qquad (4.23)$$

When the viscosity parameter η approaches zero, the rate-independent case is obtained. Introducing the Perzyna-type viscous extension causes the local driving force β to become unbounded, allowing it to take values outside the reversible domain $\mathbb{E}$ in Equation (4.18). This is explained in the work of MIEHE & SCHÄNZEL [96]. In the rate-independent setting, the free energy in Equation (4.7) leads to the crack driving force expressed in Equation (4.13),

$$f = \mathcal{G}_c\delta_d\gamma_l := \frac{\mathcal{G}_c}{l}[d - l^2\Delta d] = -g_v'(d)\Psi_v(J) - g_f'(d)\,\Psi_f(\lambda_n) - g_c'(d)\,\Psi_c(\nu_n) > 0 . \qquad (4.24)$$

By defining the functions $h_v(d) = -g_v'(d)$, $h_f(d) = -g_f'(d)$, and $h_c(d) = -g_c'(d)$, the crack driving force can be rewritten as

$$f = h_v(d)\Psi_v(J) + h_f(d)\,\Psi_f(\lambda_n) + h_c(d)\,\Psi_c(\nu_n) . \qquad (4.25)$$

4.2.3 History-field based representation of crack driving force

Replacing $\psi_{cr} = g_c/l$ in (4.18) by this field, we obtain the equation

$$\boxed{[d - l^2\Delta d] = h_v(d)\overline{\mathcal{H}}_v + h_f(d)\overline{\mathcal{H}}_f + h_c(d)\overline{\mathcal{H}}_c ,} \qquad (4.26)$$

for the evolution of the phase field in the case of loading *and* unloading. Note that this equation equips the crack topology by the local *crack source* on the right hand

side. We introduce the *local history field* of a maximum positive reference energy of
the polymer network

$$\overline{\mathcal{H}}_v := \max_{s\in[0,t]}\langle\frac{\psi_v(J,s)}{\psi_{cr}^v}-1\rangle \quad \overline{\mathcal{H}}_f := \max_{s\in[0,t]}\langle\frac{\psi_f(\lambda_n,s)}{\psi_{cr}^f}-1\rangle \quad \overline{\mathcal{H}}_c := \max_{s\in[0,t]}\langle\frac{\psi_c(\nu_n,s)}{\psi_{cr}^c}-1\rangle$$
(4.27)

obtained in a typical multiaxial loading scenario. The variational formulation requires
$\psi_{cr}^v = \psi_{cr}^f = \psi_{cr}^c = \mathcal{G}_c/l$. Herein, distinct local evolution is foreseen for the ener-
getic and entropic response of the material. In order to (i) enforce irreversiblity, e.g.
to prevent crack healing, and (ii) to describe a distinct elastic surface, the specific
form (4.27) suppresses damage evolution below the critical energy threshold ψ_{cr} and
uses the maximum value of local crack source throughout the loading history. In
this respect, the Macaulay brackets filter out the positive values for $(\psi_i/\psi_{cr}^i - 1)$ for
$i = \{v, f, c\}$ and keeps the solid intact until the failure surface is reached. In the
above expression, free-chain and topological constraint parts of entropic response is
considered. This scenario is the most general case for the crack initiation and prop-
agation. Such an ansatz allows distinct cavitation and shear-type rupture modes. A
more specific form can be obtained if the degradation functions for the free-chain and
constraint response are identical $g_f(d) = g_c(d)$ such that

$$\boxed{[d - l^2\Delta d] = h_v(d)\overline{\mathcal{H}}_v + h_f(d)\overline{\mathcal{H}}_e}$$
(4.28)

and a specific choice of local crack driving forces in the sense

$$\overline{\mathcal{H}}_v := \max_{s\in[0,t]}\langle\frac{\psi_v(J,s)}{\psi_{cr}^v} - 1\rangle \quad \text{and} \quad \overline{\mathcal{H}}_e := \max_{s\in[0,t]}\langle\frac{\psi_f(\lambda_n,s)}{\psi_{cr}^f} + \frac{\psi_c(\nu_n,s)}{\psi_{cr}^c} - 1\rangle .$$ (4.29)

The latter expression can be recast into a more elegant form

$$\overline{\mathcal{H}}_e := \max_{s\in[0,t]}\langle\frac{\psi_f(\lambda_n,s) + \alpha_c\psi_c(\nu_n,s)}{\psi_{cr}^e} - 1\rangle , \quad \text{where} \quad \alpha_c = \frac{\psi_{cr}^f}{\psi_{cr}^c} \quad \text{and} \quad \psi_{cr}^e = \psi_{cr}^f$$
(4.30)

With this notion at hand, the proposed fracture phase field model may be reduced to
the compact two-field coupled problem.

$$\begin{array}{|l|}
\hline
1: \text{Div}\boldsymbol{P} + \rho_0\overline{\boldsymbol{\gamma}} = \boldsymbol{0}, \\
\\
2: d - l^2\Delta d = h_v(d)\overline{\mathcal{H}}_v + h_f(d)\overline{\mathcal{H}}_e . \\
\hline
\end{array}$$
(4.31)

which determine the current deformation and phase fields φ and d in terms of the
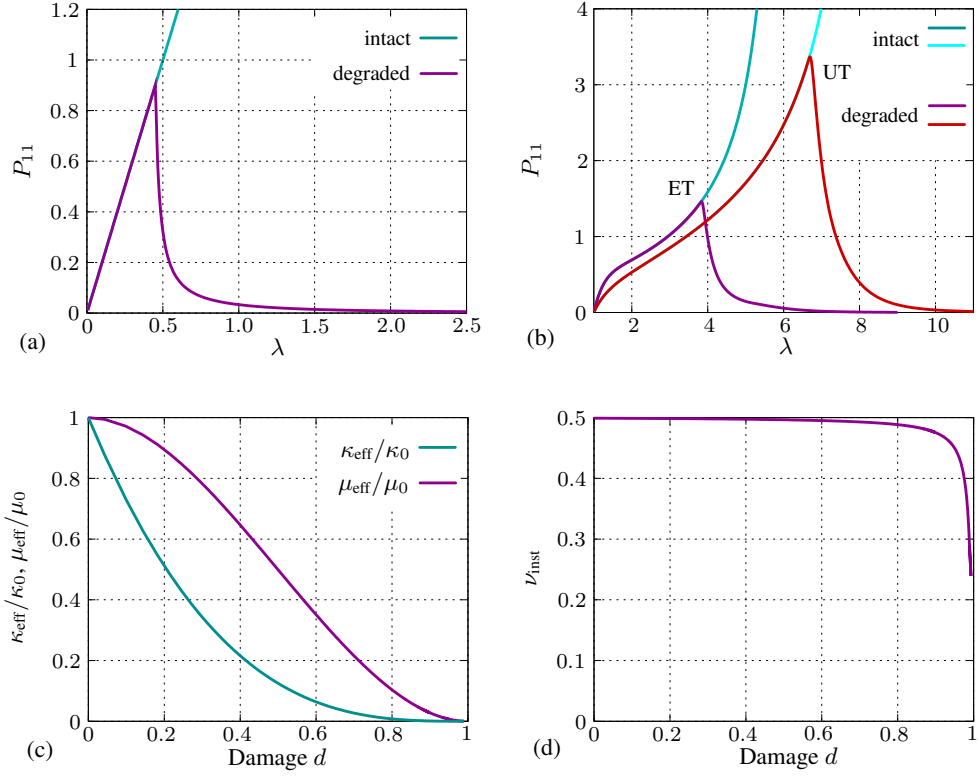
Figure 4.3: (a) The intact and the degraded first Piola Kirchhoff stress P_{11} versus strain $\epsilon = \lambda_{11} - 1$ for pancake tension deformation, (b) the intact and the degraded first Piola Kirchhoff stress P_{11} versus stretch λ_{11} under uniaxial (UT) and equibiaxial (BT) tension deformations, respectively. (c) variation of the normalized bulk and shear moduli and (d) the instantaneous Poisson's with respect to damage, respectively. The results (c,d) are identical irrespective of deformation state.

definitions (4.12), (4.28), and (4.29) This form can considered to be the most general representation of rate-independent diffusive fracture in rubbery polymers, having distinct energy thresholds for hydrostatic and and incompressible-entropic deformations exhibiting distinct damage degradation for each deformation mode. The rate–dependent formulation with the definition of $\overline{\mathcal{H}}_e$ can be stated as a two–field problem with $\beta = f$

$$
\begin{aligned}
&1: \ \mathrm{Div}\boldsymbol{P} + \rho_0\overline{\boldsymbol{\gamma}} = \boldsymbol{0}, \\
&2: \ d - l^2\Delta d + \eta\dot{d} = h_v(d)\overline{\mathcal{H}}_v + h_f(d)\overline{\mathcal{H}}_e \ .
\end{aligned}
\tag{4.32}
$$

The overall behavior of the presented phase-field formalism can be demonstrated on

a material point simulation in pancake, uniaxial, and equibiaxial tension type loading scenarios, where the results are shared in Fig. 4.3. The degradation characteristics for these simulations is set to be, $\{\theta = 0.01, \alpha = 2\}$ for entropic degradation and $\{\theta = 2, \alpha = 3\}$ for volumetric degradation. This sets a big difference in degradation rates for entropic and volumetric parts (see Fig. 4.3(c)) which manifests itself in the degradation of instantaneous Poisson's ratio ν_{inst} as in Fig. 4.3(d). Since the behaviors in Fig. 4.3(c,d) are manifested only due to the degradation characteristics, they are independent of the deformation state.

CHAPTER 5

DISTORTIONAL AND DILATATIONAL FAILURE SURFACES FOR RUBBER-LIKE MATERIALS

5.1 Dilatational and distortional failure modes: Comparison with literature and stretch based failure criteria

In order to demonstrate the capabilities of the proposed model, uniaxial tension, biaxial tension, pure shear, and pancake test simulations are carried out. The ultimate stretches for each test are plotted in a modified principal strain space. In the logarithmic principal strain space $\varepsilon_i = \ln(\lambda_i)$ (for $i = 1, 2, 3$), $\varepsilon_1 = \varepsilon_2 = \varepsilon_3$ line describes the hydrostatic axis, where only volumetric deformation can take place. Any deformation in a perpendicular plane to the hydrostatic axis is distortional in nature. Hence, a useful coordinate transformation proposed by HAMDI & MAHJOUBI [127] and used by ROSENDAHL ET AL. [107] in their studies of strain based failure criteria, can also be utilized in the context of this study to aid the visualization of different failure modes with the definition

$$\begin{bmatrix} \varepsilon_1 \\ \varepsilon_2 \\ \varepsilon_3 \end{bmatrix} = \frac{1}{\sqrt{6}} \begin{bmatrix} \sqrt{2} & \sqrt{3} & -1 \\ \sqrt{2} & 0 & 2 \\ \sqrt{2} & -\sqrt{3} & -1 \end{bmatrix} \begin{bmatrix} \xi_1 \\ \xi_2 \\ \xi_3 \end{bmatrix} \tag{5.1}$$

where ξ_i ($i = 1, 2, 3$) are modified strains. $\xi_1 = const.$ describes what is called the Π plane. In parallel to the discussion here, the incompressibility condition $J = 1$ and the critical volumetric deformation $J = J_c$ describe two surfaces in the principal stretch space, see Fig. 5.1(a). The compressible or nearly-incompressible rubber-like materials are bounded below with $J = 1$ surface for the tensile volumetric deformation region and above with $J = J_c$, which describes the maximum attainable volumetric deformations up to the onset of cavitation for the given material. The same condi-
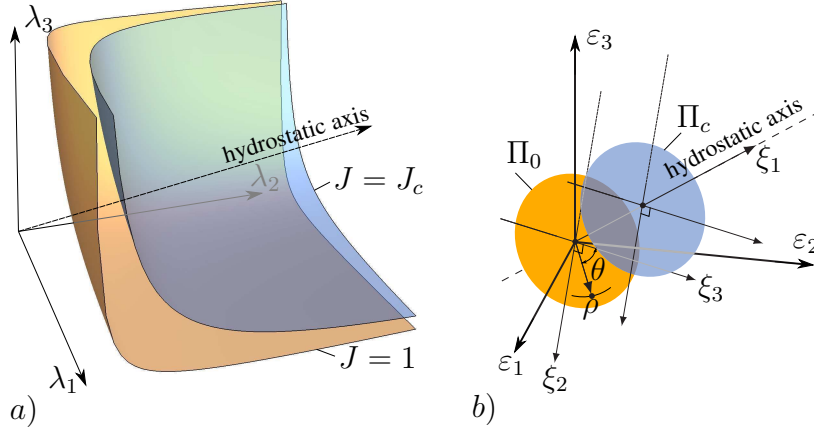
Figure 5.1: Incompressibility ($J = 1$) and critical volumetric deformation ($J = J_c$) surfaces in (a) principal stretch space, and corresponding planes in (b) logarithmic principal strain space. Note that J_c is taken non-realistically large in both figures for visualization purposes.

tions are described between two bounding planes, i.e. $\xi_1 = 0$ and $\xi_1 = \ln(J_c)$ in the modified strain space (denoted by Π_0 and Π_c in Fig. 5.1(b), respectively).

Referring to Fig. 5.1(b), on a $\xi_1 = const.$ plane, two coordinates ρ and θ can be defined to describe any distortional deformation. These coordinates, along with ξ_1, i.e. (ξ_1, ρ, θ), are known as Haigh-Westegaard coordinates (θ is also called Lode angle). They are expressed in terms of the first invariant of the Hencky strain tensor $\boldsymbol{H}$ and second and third invariants of the deviatoric part of Hencky strain tensor $\boldsymbol{H}$,

$$\xi_1 = \frac{1}{2}I_1, \tag{5.2}$$

$$\rho = \sqrt{2I_2'}, \tag{5.3}$$

$$\theta = \frac{1}{3}\cos^{-1}\left(\frac{3\sqrt{3}}{2}\frac{I_3'}{\left(I_2'\right)^{3/2}}\right). \tag{5.4}$$

The definition of the first invariant of $\boldsymbol{H}$ and second and third invariants of the deviatoric part of $\boldsymbol{H}$ (i.e., $\boldsymbol{H}' = \text{dev}\boldsymbol{H}$) read

$$I_{1,\boldsymbol{H}} = I_1 = \varepsilon_1 + \varepsilon_2 + \varepsilon_3, \tag{5.5}$$

$$I_{2,\boldsymbol{H}'} = I_2' = \frac{1}{6}\left((\varepsilon_1 - \varepsilon_2)^2 + (\varepsilon_1 - \varepsilon_3)^2 + (\varepsilon_2 - \varepsilon_3)^2\right), \tag{5.6}$$

$$I_{3,\boldsymbol{H}'} = I_3' = \left(\varepsilon_1 - \frac{1}{3}I_1\right)\left(\varepsilon_2 - \frac{1}{3}I_1\right)\left(\varepsilon_3 - \frac{1}{3}I_1\right), \tag{5.7}$$

respectively.
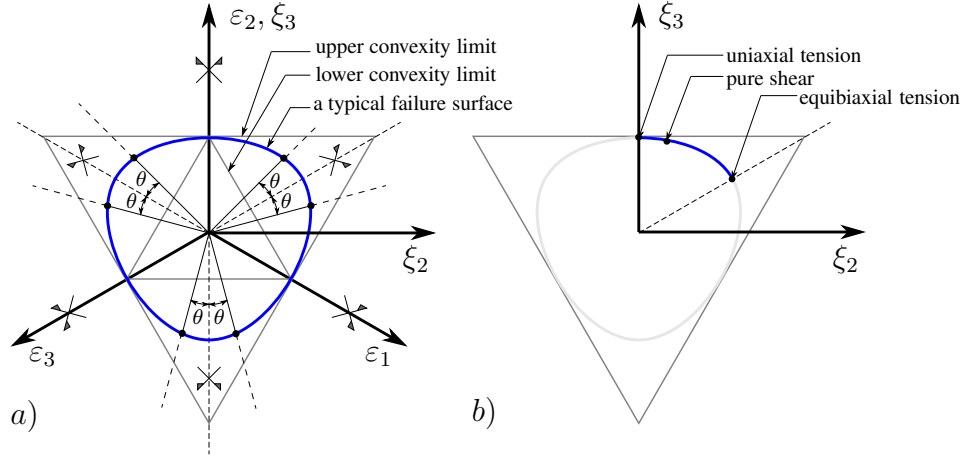
Figure 5.2: A typical failure surface in $\xi_2 - \xi_3$-plane and (a) the associated symmetries of the experiments due to the arbitrariness of the eigenvalues of deformation tensor and material isotropy, (b) the corresponding ultimate stretch points on the failure surface for uniaxial, equibiaxial, and pure shear experiments.

5.1.1 Failure data

The uniaxial tension, (equi)biaxial tension, and pure shear experiments are well-known (or classical) experiment types for mechanical characterization of rubber-like materials [37]. In these experiments, the point where the failure starts can readily be accessed in terms of strains with the help of modern extensometers (e.g., video extensometers). However, it is much more challenging to obtain the corresponding true stresses. Therefore, two datasets, both reporting ultimate stretch values, are utilized in this paper to assess the proposed failure concept. KAWABATA [128] used a special biaxial test device where two perpendicular directions on a thin square rubber specimen are stretched at prescribed values to obtain different biaxiality ratios. On the other hand, HAMDI ET AL. [129, 130] utilized an inflation-type test apparatus, where a thin circular rubber specimen is fixed on top of a circular (or elliptical) hole. A prescribed amount of pressure is applied through the hole, and the rubber specimen is inflated while recording the amount of displacement at the apex point through an LVDT sensor. Kawabata reported the ultimate stretch data for unfilled natural (NR) and styrene-butadiene rubber (SBR) specimens, while HAMDI ET AL. [129] worked with filled NR and SBR. The ultimate failure points are presented in
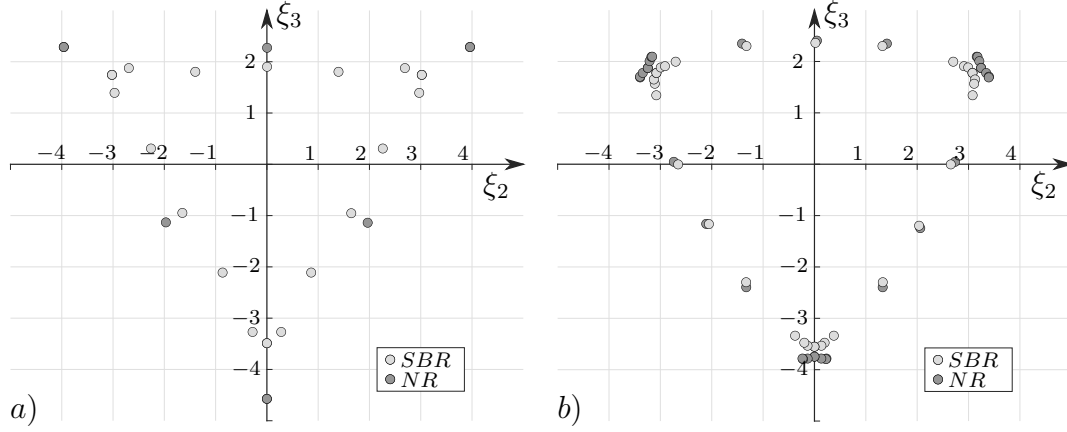
Figure 5.3: Ultimate stretches projected onto the $\xi_2 - \xi_3$-plane for (a) unfilled NR and SBR experiments of KAWABATA [128], and (b) filled NR and SBR experiments of HAMDI ET AL. [129, 130]

modified principal strain space in Fig. 5.3, where the data is reflected with respect to the line corresponding to the equibiaxial deformations and symmetrically repeated at $2\pi/3$ intervals and plotted on Π_0 plane, i.e. $\xi_1 = 0$. On the figure (cf. Fig. 5.2 and Fig. 5.3), the arbitrariness of the eigenvalues of a tensor leads the symmetries with respect to the equibiaxial lines, and the material isotropy leads the symmetries across the principal directions.

5.1.2 Equivalent strain failure criteria

A review of classical and modern equivalent stress based failure criteria is provided in KOLUPAEV [105]. The idea of equivalent strain failure criteria (see ROSENDAHL ET AL. [107]) is adopted from the well known stress based counterpart with the phenomenological description of the failure surface $\phi(\varepsilon)$, that is

$$\phi(\varepsilon_1, \varepsilon_2, \varepsilon_3) = \varepsilon_{eq}(\varepsilon_1, \varepsilon_2, \varepsilon_3) - \varepsilon_c = 0, \tag{5.8}$$

where, ε_c is the critical strain. Material withstands the given deformations for the region $\phi(\varepsilon) < 0$, and fails if $\phi(\varepsilon) \geq 0$. In Table 5.1, 5 classical and 1 modern strain failure criteria are listed and their equivalent strain expressions are provided. Notice that, Rankine-like and Mariotte-like criteria are pressure sensitive, i.e., the failure surface varies on the hydrostatic axis. However, these models' volumetric failure predictions

Table 5.1: List of the definitions for the classical and modern failure criteria [107]. In the expressions, $\varepsilon_1 \geq \varepsilon_2 \geq \varepsilon_3$ is assumed, i.e., $\{\varepsilon_1, \varepsilon_2, \varepsilon_3\}$ is an ordered tuple of principal (true) strains.

Classical criteria	expression	pressure sensitivity
Rankine-like (the maximum normal stress hypothesis)	$\varepsilon_{eq} = \max\limits_{i=1,2,3} \varepsilon_i$	+
Tresca-like (the maximum shear stress hypothesis)	$\varepsilon_{eq} = \varepsilon_1 - \varepsilon_3$	−
von Mises-like	$\varepsilon_{eq} = \sqrt{3I_2'}$	−
Mariotte-like	$\varepsilon_{eq} = \dfrac{3}{2}\left(\varepsilon_1 - \dfrac{1}{2}I_1\right)$	+
Ivlev-like	$\varepsilon_{eq} = I_1 - 3\varepsilon_3$	−

Modern criteria	expression	pressure sensitivity
Podgorski-Bigoni-Piccolroaz	$\varepsilon_{eq} = \rho \cos\left(\beta\dfrac{\pi}{6} - \dfrac{1}{3}\cos^{-1}\left(\alpha\cos 3\theta\right)\right)$	−

were not meant to be utilized and should be used for shear type failure predictions restricted to the Π_0 plane. The phenomenological *Podgorski-Bigoni-Piccolroaz (PBP)* criterion has two parameters which can be adjusted to obtain convex and mathematically accurate predictions. The parameters $\alpha \in [0,1]$ and $\beta \in [0,2]$ are restricted in order to preserve the convexity of the model. Furthermore, it can be reduced to criteria; Mariotte-like for $\{\alpha = 1, \beta = 0\}$, Tresca-like for $\{\alpha = 1, \beta = 1\}$, Ivlev-like for $\{\alpha = 1, \beta = 2\}$, and von-Mises like for $\{\alpha = 0, \beta \in [0,2]\}$. The failure surface predictions of the classical and *PBP* criteria are listed in Fig. 5.4. Notice that, in the figures, Mariotte-like and Rankine-like criteria have similar ∇ shapes with different ε_c values, and denote the upper-convexity limit for any convex failure criteria. Likewise, Ivlev-like criterion takes on a Δ shape and provides the lower-convexity limit.
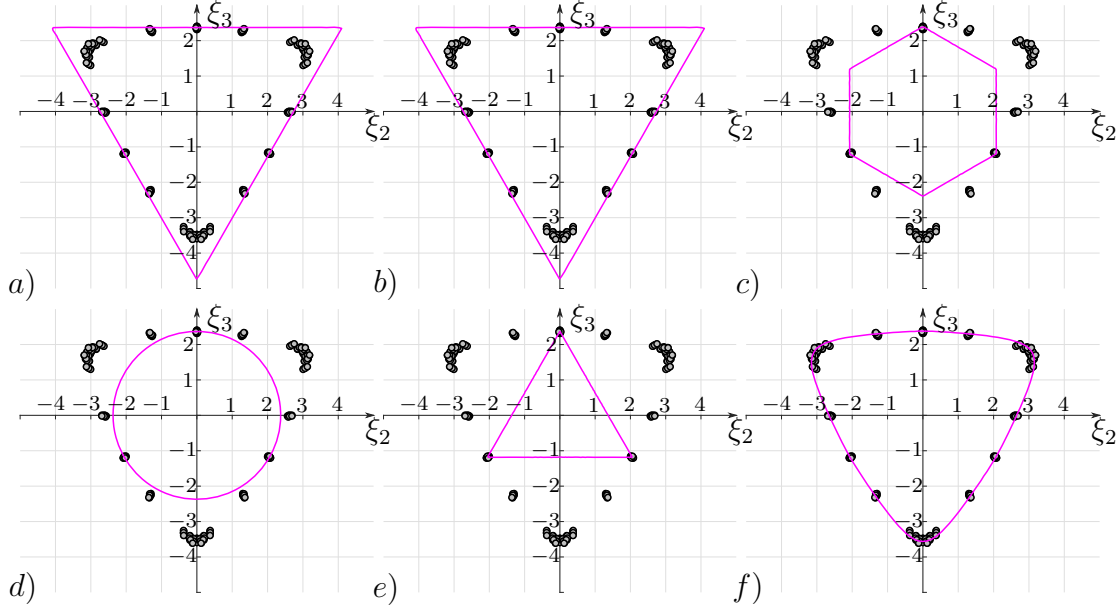
Figure 5.4: Classical and modern failure criteria predictions on HAMDI ET AL. [129, 130]. a) Rankine-like with $\varepsilon_c = 1.95$, b) Mariotte-like with $\varepsilon_c = 2.92$, c) Tresca-like with $\varepsilon_c = 2.95$, d) von-Mises like with $\varepsilon_c = 2.92$, e) Ivlev-like with $\varepsilon_c = 2.92$, and f) Podgorski-Bigoni-Piccolroaz with $\varepsilon_c = 2.38$, $\alpha = 0.9$, $\beta = 0.1$.

5.1.3 Failure criterion fits

In this section, we demonstrate the capabilities of this contribution's disctinct critical reference energies in the context of failure surface predictions. Let the volumetric free energy expression be separated as,

$$\psi_v := \begin{cases} \psi_v^+ & \text{for} \quad J \geq 1 \\ \psi_v^- & \text{for} \quad 0 < J < 1 \end{cases} \tag{5.9}$$

where $J \geq 1$ corresponds to volumetric tension. With this separation, the local driving forces $(4.29)_1$ and (4.30) constitute an energetic-entropic decoupled failure surface for their values,

$$\text{Distinct}: \begin{cases} \dfrac{\psi_v^+}{\psi_{cr}^v} - 1 = 0, \\ \dfrac{\psi_f + \alpha_c \psi_c}{\psi_{cr}^e} - 1 = 0. \end{cases} \tag{5.10}$$

64
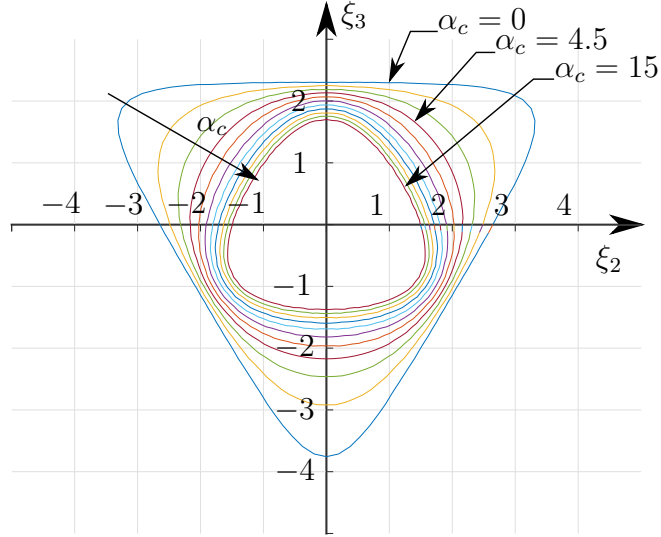
Figure 5.5: The parametric study of the constraint critical energy ratio α_c for fixed ψ^e_{cr}. Increase in α_c reduces the ultimate stretches for equibiaxial deformations more prominently compared to the reduction of ultimate stretches for uniaxial deformations. The increase in α_c changes the Mariotte-like (upper-convexity limit) initial shape towards von-Mises (circular failure surface) to the Ivlev-like (lower-convexity limit) failure surfaces (cf. Fig. 5.2).

On the other hand a failure criterion in the sense that

$$\text{Unified}: \quad \frac{\psi^+_v}{\psi^v_{cr}} + \frac{\psi_f + \alpha_c \psi_c}{\psi^e_{cr}} - 1 = 0, \tag{5.11}$$

can be defined for a coupled (unified) energetic-entropic failure surface.

The entropic part of the failure criteria contains constraint critical energy ratio α_c to control the contribution of the I_2 term on the failure surface. Notice that if $\alpha_c = 0$, then the entropic part of the failure criteria reduces to the free-chain response. A parametric study on the effect of constraint critical energy ratio is given in Fig.5.5. The shape of the failure surface for different α_c values between upper and lower convexity limits passes through von-Mises like surface. For large values of α_c, a Δ shaped surface is obtained. In this case, the failure is determined mostly by equibiaxial deformations. For multiaxial deformations, both (5.10) and (5.11) define a 3D failure surface. The effect of using (5.11) as the failure criterion is a shrinking distortional envelope along hydrostatic axis. This approach is inline with the CUNTZE's
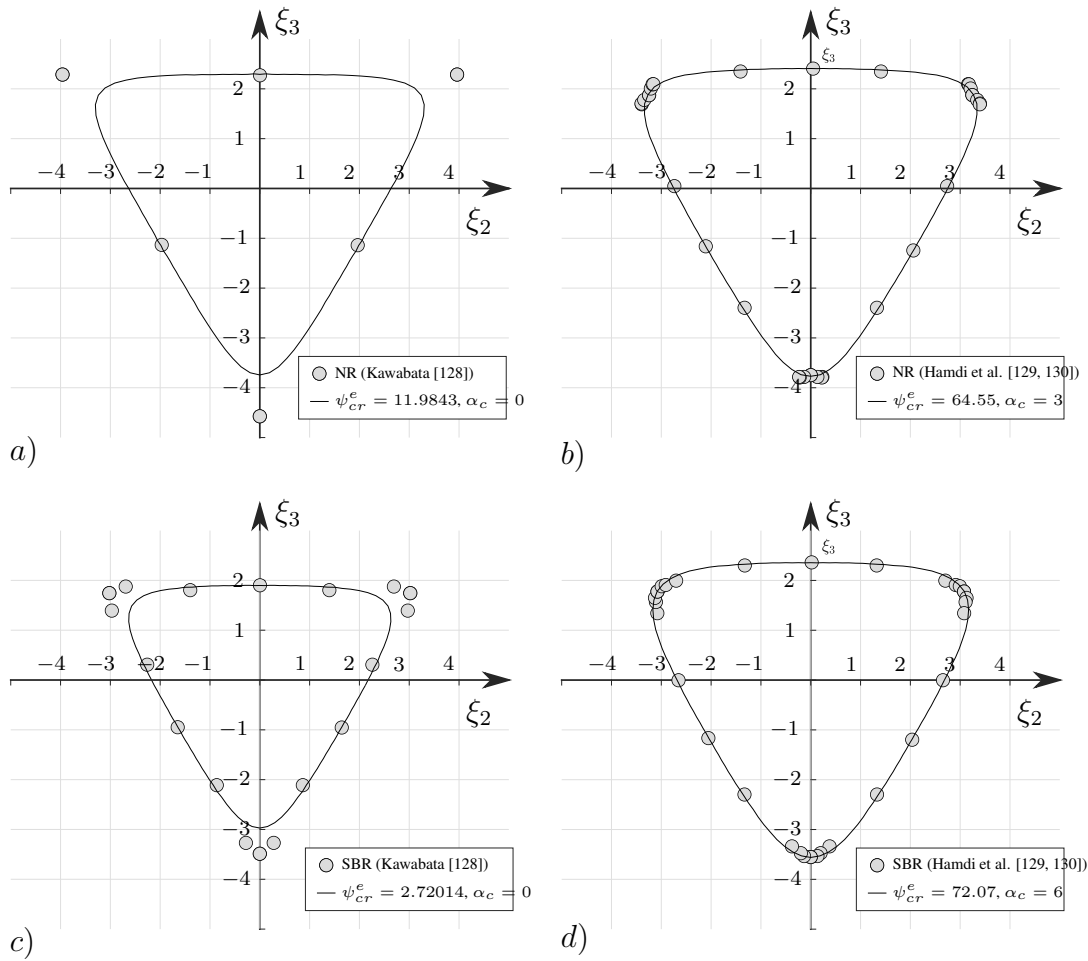
Figure 5.6: Failure surface fits for the (a,c) unfilled NR and SBR experiments of Kawabata [128] and (b,d) filled NR and SBR experiments of HAMDI ET AL. [129, 130]. The entropic critical energies (ψ_{cr}^e) and the constraint critical energy ratios ($\alpha_c = \psi_{cr}^e/\psi_{cr}^c$) for the associated fits are given in the legends.

Table 5.2: Extended eight-chain parameters for the failure surface fits for Hamdi et al. [129]

	$\mu\,[MPa]$	$N\,[-]$	$\mu_c\,[MPa]$	$\chi\,[MPa]$
Filled NR	0.885	15	0.74	280
Filled SBR	1.75	18.4	0.54	500

[131, 107] failure modes concept, which can be re-stated in the context of this study with the failure surface definition

$$\left[\left(\frac{\psi_e(\lambda_r, \nu_n)}{\psi_{cr}^e}\right)^m + \left(\frac{\psi_v^+(J)}{\psi_{cr}^v}\right)^m\right]^{1/m} = 1 \qquad (5.12)$$

where, the constant m controls the coupling between entropic and volumetric contributions. Since there is no experimental evidence on the coupling term m and (5.10) is more convenient in the phase-field theory, distinct failure criterion is chosen as the final failure criterion which corresponds to $m = \infty$. Notice that, in (5.11) $m = 1$. In both (5.10) and (5.11), after reaching failure surface, i.e. after the crack initiation, the crack propagates in a way that the poisson's ratio along the crack path reduces due to the utilization of separate degradation functions $g_v(d)$ and $g_f(d)$.

We utilize HAMDI ET AL. [129] datasets and show the failure surface predictions on Π_0 plane. Then, a multiaxial extension is demonstrated on the modified logarithmic principal strain space. The parameters for both filled NR and filled SBR fits are provided in Table 8.1. The results are shown in Fig. 5.6 on Π_0 fits, and Fig. 5.7 for volumetric extension.
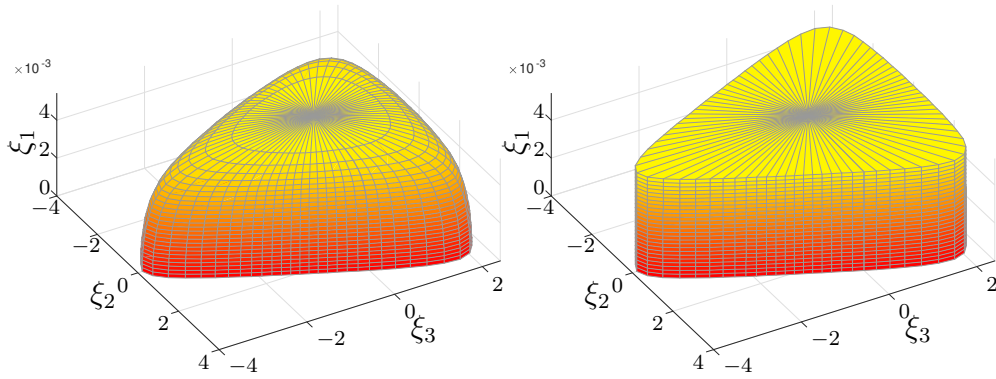
Figure 5.7: Failure surface fits for filled SBR and NR data of HAMDI ET AL. [129] in modified principal strains space with (a) unified and (b) distinct failure criteria, respectively. The ξ_1 axis is scaled and the volumetric critical energy for SBR is $\psi_{cr}^v = 0.02$ [MPa/m^3].

In Fig.5.6, the ultimate stretch points for equibiaxial experiments of HAMDI ET AL. [129] are captured by setting appropriate α_c values. On the other hand, the ultimate

stretches for equibiaxial points of Kawabata [128] dataset fall outside of upper convexity limit of the model, thus α_c's are set to 0 for both experiments of [128].

CHAPTER 6

INTERPLAY BETWEEN VISCOELASTICITY OF THE BULK AND PHASE-FIELD APPROACH TO FRACTURE

Rubber-like materials are strongly rate-dependent in both their mechanical response and fracture properties. The key constitutive relations are established in the previous chapters for hyperelastic and viscoelastic responses of rubber-like materials, and a generalized phase-field approach is provided in detail. In this chapter, we couple these theories to represent rate-dependent characteristics of fracture. Beside this coupling, the afforementioned phase-field theory brings about the idea of degrading Poisson's ratio. In this chapter, the interplay between the extended eight-chain model and the nonlinearly viscous theory is of concern for the present phase-field approach. The most fundamental characteristics, relevant to the presented phase-field theory, is the fracture toughness or the critical energy release rate $\mathcal{G}_c$, as a material parameter. Therefore, one can, naturally, start with a phenomenological expression for a rate dependent critical energy release rate. In [93], YIN ET AL proposed a rate-dependent fracture toughness with a degradation characteristic given in the context of phase-field fracture, i.e., in small-strain rates (in terms of $\dot{\varepsilon}$)

$$\mathcal{G}_c = \mathcal{G}_c^0 \left(1 + \alpha\, g(d)\dot{\boldsymbol{\varepsilon}} : \dot{\boldsymbol{\varepsilon}} \right). \tag{6.1}$$

In this expression, $\mathcal{G}_c^0$ is base or undegraded critical energy release rate, α is a parameter to scale the contribution of strain-rates to the expression and $g(d)$ is utilized as to penalize the effects of rates for already fractured (large values of d) regions and to focus the expression on the regions where crack may propagate. This is an excellent modification for the critical energy release rate $\mathcal{G}_c$ for varying strain-rates. However, the theory is in small-strains setting and focuses on the evolution of fracture. Furthermore, [93] attributed this to the difference in chain strength and strength

of entanglements and cross-links. For the loads applied in high strain-rates, the relaxation kinetics transfers the loads towards equilibrium, however the chains' relaxation is not infinitely fast and they become main carriers of the load, which require more energy to break. This theory does not require tracking the crack propagation velocity $\dot{a}$ (as in the case of [94]), since it utilizes a phase-field framework. LOEW ET AL. [95] directly extended the numerical stabilization parameter (also present in our theory) of MIEHE & SCHAENZEL [96] and gave a viscoelastic response to the bulk, and obtained the first finite theory. The damage growth is regularized and a rate-dependent driving force expression is obtained. This theory incorporates the finite strains linearly viscous theory of HOLZAPFEL [97] and avoids local history field (of [81]) altoghether. With the history variable expression, they observed an unbounded growth of phase-field even though $\mathcal{H}$ stays constant. Therefore, they used an active set method to stop the growth of d. The provided experiments on EPDM rubber for SENT as well as DENT specimens validates their theory. Since the degradation functions are an integral part of the phase-field approach, they discussed the several known degradation functions and their effects as well. Also, the calibration of the phase-field length scale parameter l through DIC renders physically accurate results. Although we follow the same line of thinking (see [95, 132, 133, 134, 135]), our approach defines a generic multi-axial failure surface and fully express the critical energy expressions, i.e., $\psi_{cr} = \mathcal{G}_c/l$ without splitting $\mathcal{G}_c$ and l. Further investigation for a decoupling of these as separate material parameters is required and not addressed in the present dissertation. In [98], YIN & KALISKE proposed another approach, where they tracked the intact total free energy consisting of the summation of equilibrium and non-equilibrium responses as the history variable in the phase-field expressions, i.e.,

$$\mathcal{H} = \underset{\tau \leq t_{n+1}}{\text{Max}}\, \psi_0^+(\boldsymbol{F}, \tau) \tag{6.2}$$

where, ψ_0^+ with a volumetric-isochoric split, was given in the form,

$$\psi_0^+ = \psi_{vol}^+ + \psi_{iso}^{eq,+} + \psi_{iso}^{ne,+} \tag{6.3}$$

with $+$ sign denoting tensile part of the respective energy components, i.e., volumetric (ψ_{vol}^+), isochoric equilibrium ($\psi_{iso}^{eq,+}$), and isochoric non-equilibrium ($\psi_{iso}^{ne,+}$) energies, respectively. Their viscoelastic expressions are based on REESE & GOVINDJEE's nonlinearly viscous theory [60], and utilize neo-Hookean Maxwell branches for equi-

70

librium as well as non-equilibrium responses. This theory correctly captures the increase in reaction force at fracture on a load-displacement curve at increasing rates for the SENT and DENT experiments on EPDM rubber of LOEW ET AL. [95]. However, we encountered an increase in displacement at fracture (see Fig. 6.4) for increasing loading rates in our v-shape DENT (vDENT) experiments (similar to ones given in [136]) of unfilled SBR. SHEN ET AL. [99] took a different approach to incorporate rate-dependent effects into the fracture process. They included a portion of the dissipated energy into the dissipation inequality expression and used this to derive the rate-dependent partial differential equations (PDEs) for the multi-field problem. The contribution of the dissipated energy is controlled using a parameter, and they suggested a mental picture of the fracture process zone, shown in Fig. 6.1. They focused on the highly non-linear region (region III) and the mainly viscous-driven dissipative region (region II) in the process zone. In our work, we also focused on region III, where we observed a degrading incompressibility of the bulk. However, SHEN ET AL. [99] considered region II to be the main factor connecting the phase-field fracture and viscous response in the bulk. They suggested that this dissipative region generates self-heating, which promotes both the nucleation and propagation of fractures and alters the evolution of crack growth rate. Although the temperature increase is evident, further research is needed to quantify this increase with a thermo-mechanical coupling in the phase-field approach. Finally, note that the theory proposed by SHEN ET AL. [99] is linear in both the elastic and viscous branches.

6.1 A direct coupling of viscous stored energy into the disctinct failure criterion

In light of the afforementioned works, we can favor the approach by [98] (also see DAMMASS ET AL. [137, 138]) in the following sense within our distinct failure criterion 5.10,

$$
\text{distinct viscous :} \quad
\begin{cases}
\dfrac{\psi_v^+}{\psi_{cr}^v} - 1 = 0, \\[2ex]
\dfrac{\psi_f + \alpha_c \psi_c + \beta_v \psi_f^{ne}}{\psi_{cr}^e} - 1 = 0,
\end{cases}
\tag{6.4}
$$

and omitted the volumetric-viscoelastic effects altogether. In this expression, ψ_f^{ne} refers to the total free-chain part of non-equilibrium. As in the SHEN ET AL. [99]

71
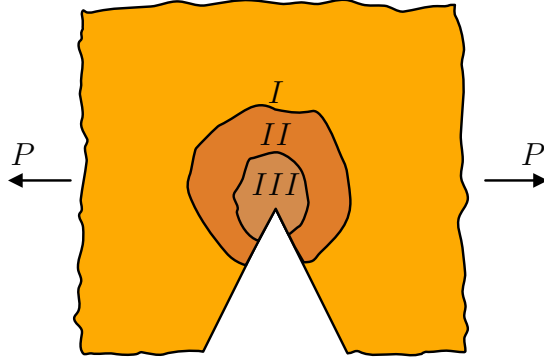
Figure 6.1: A representative schematic view of the process zone around the crack tip [99]. I denotes the uneffected (and undamaged) region, II represents the region where viscoelastic dissipative effects take place, finally, III shows the region where nonlinear inelastic and irreversible processes occur, these can be counted as cavity formation, bond or cross-link rupture.

we included a control parameter β_v, but for the viscous stored part to be able to adjust the viscous contribution. The effect of incorporating the viscous stored energies into the entropic driving expression will be discussed next. Note that, different from [98], this expression provides a direct alteration of the entropic failure surface with respect to the amount of activations of the viscous branches. The modified total free energy expression then becomes

$$\Psi = (g_v(d) + k)\psi_v^e + (g_e(d) + k)\psi_e^e + g_e(d)\psi_f^{ne}. \tag{6.5}$$

This expression leads to the thermodynamical force expression,

$$f := -\partial_d \Psi = -g_v'(d)\psi_v^e - g_e'(d)\psi_e^e - g_e'(d)\psi_f^{ne} \tag{6.6}$$

where, using 6.4, the entropic history field can be rewritten as,

$$\overline{\mathcal{H}}_e := \max_{s\in[0,t]} \left\langle \frac{\psi_f(\lambda_n, s) + \alpha_c \psi_c(\nu_n, s) + \beta_v \psi_f^{ne}(I_1^e, s)}{\psi_{cr}^e} - 1 \right\rangle , \tag{6.7}$$

which ensures the irreversibility, and protects the thermodynamical consistency because of the use of the Macaulay brackets.

Consider a generic rubber material with a single Maxwell branch, whose parameters provided in Table 6.1. With this material, the effect of 6.4 can be demonstrated

Table 6.1: A generic rubber specimen with a single Maxwell branch for demonstration. Simulation parameters as well as degradation functions are listed.

Equilibrium part			
χ [MPa]	μ [MPa]	N [-]	μ_c [MPa]
462	0.34	90	0.9

Non-equilibrium part				
χ^v [MPa]	μ^v [MPa]	N^v [-]	$\dot{\gamma}_0/\hat{\tau}_m$ [MPa^{-m}s^{-1}]	m [-]
462	0.34	90	1	1

Phase-field related					
ψ_{cr}^e [MPa/m^3]	ψ_{cr}^v [MPa/m^3]	$l \sim$ [mm]	α_c [-]	η [-]	k [-]
1	∞	1	1	0	0

Degradation behavior	α	θ
Volumetric degradation	2	3
Entropic degradation	2	10^{-2}

with single element simulations on a unit cube (1mm $\times$ 1mm $\times$ 1mm) in uniaxial deformation mode at different strain-rates. Since the length scale parameter is also taken as $l = 1$ [mm], i.e., unity, we can consider this study as material point simulation. Before giving the associated results, we would like to mention that numerical viscosity η terms from the rate-dependent formulation 4.19 is ignored and artificial stiffness k is taken 0 (all in all, these parameters were only conceived for quasi-static phase-field simulations). Thus their effects are not present. This is firstly due to preventing adulteration of the results and to show stable behavior of the simulation with bulk viscoelasticity, i.e., it shows numerically improved results. However, with the inclusion of viscoelasticity, Δt becomes important and we observed a limiting stable value for it, for instance, in these simulations, for $\dot{u} = 100$ [mm/min], Δt should be equal or below 10^{-3} [s]. Finally note that, ψ_{cr}^v is also taken a large value, where 1 [MPa/mm^3] in this case corresponds to no volumetric fracture, the range of change in J is extremely small in this simulation, therefore ψ_{cr}^v is shown as ∞ in Table 6.1,

thus we concentrated only on the entropic fracture and rate-effects related to it.
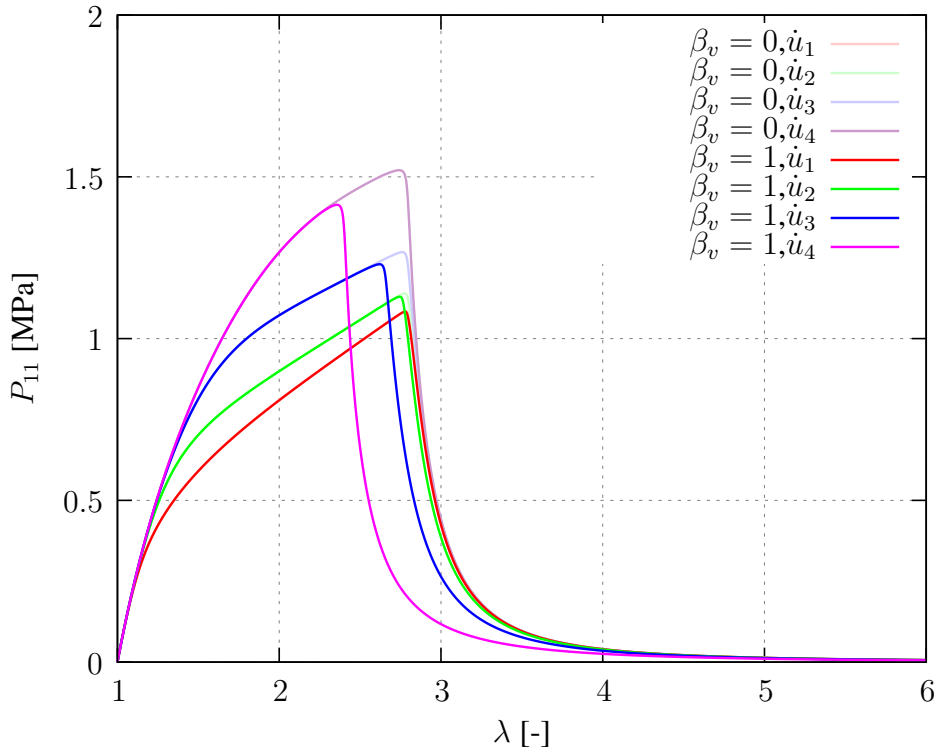
Figure 6.2: Varying rates of $\dot{u}_i = \{0.1, 1, 10, 100\}$ [mm/min] on material point simulations for the parameters listed in Table 6.1, comparing $\beta_v = 0$ and $\beta_v = 1$.

First, we changed the strain-rate in a uniaxial tension setting for fracture simulation and observed the behavior of the model, with $\beta_v = 1$ against the original distinct failure criterion 5.10 (which can be obtained by setting $\beta_v = 0$). Considered rates are $\dot{u} = \{0.1, 1, 10, 100\}$ [mm/min] in a displacement driven regime. These results are given in Fig 6.2. A quick glance over the results reveals an increased stress and decreased stretch at failure for increased strain rates. Similar behavior was also reported in [98, 94, 95, 99]. Finally, we provided a parametric study for varying β_v for the values $\beta_v = \{\pm 1, \pm 0.75, \pm 0.5, \pm 0.25, 0\}$, and shown the results in Fig. 6.3. Negative β_v values seem to cause proportional resistance to the crack nucleation, an interesting result, where the viscous effects can also be negatively contributing to the fracture through dissipation of the energy normally going into the fracture in viscous processes. This can further be explained by the relaxation taking precedence over fracture; instead of rupturing the chains of stretched molecules (which requires larger energies compared to slip the chains through entanglements), a forced and rapid re-

laxation might be happening.
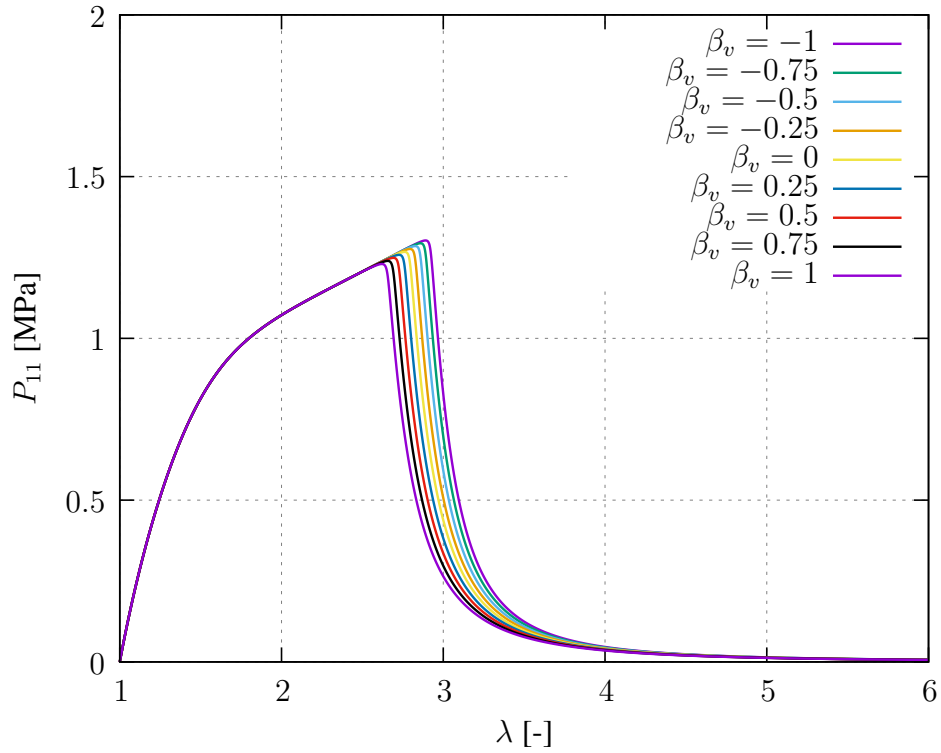
Figure 6.3: Effect of varying beta values at $\dot{u} = 10$ [mm/min] constant speed on material point simulations for the parameters listed in Table 6.1, exhibiting stable behavior for negative values of β_v.

One of the main advantages of such a modification is the unaltered degradation of rubber's incompressibility. Therefore, this approach preserves the region II behavior depicted schematically in Fig. 6.1. Bulk viscous effects in region III is directly contributing to the critical energy release rate. Therefore, both region II and region III are covered. Note that, the μ^v value is equal to the μ of the ground-state behavior in Table 6.1, which is rather a large value. This causes the viscous effects to be more pronounced on the point of fracture.

We chose explicitly to degrade the viscous contribution to the free-energy with the entropic degradation function. However, a further study would allow a separate degradation of the viscous part as well, which we haven't pursued in this dissertation work. For instance, a faster or slower degradation of the viscous part would allow alteration of the crack propagation behavior as well. This has the potential utilization in fatigue
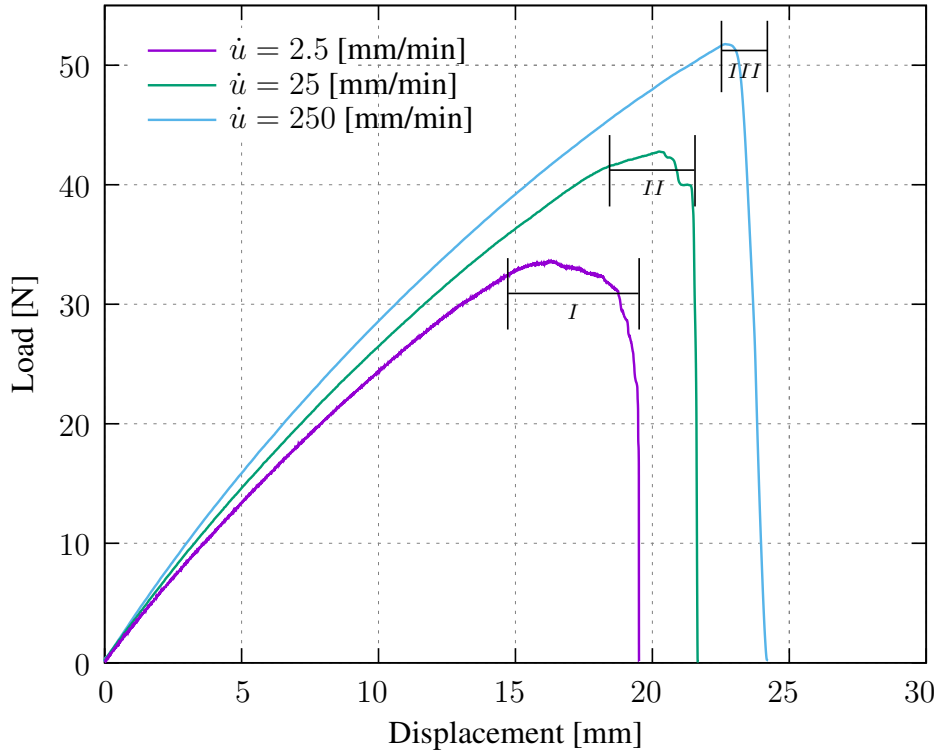
Figure 6.4: Load-displacement curves for the fracture experiments at different rates on die cut unfilled SBR specimens with the symmetric vDENT geometry given in Fig 8.2. The increased rates postpones the fracture. I, II, and III show the shrinking span in displacement axis with increased rates.

crack growth studies. The inclusions as well as inhomogeneous constituents due to rubber production process causes varying critical energy release rates within the samples, which has the utmost importance to the fatigue crack growth. On this regard see the excellent work of WU ET AL. [139]. This variations cause a more smeared fracture for slow loading rates compared to more abrubt failure at high strain rates. We provided a supporting evidence in Fig. 6.4 here from our experimental work (discussed in the next section) on unfilled SBR rubber fracture specimens cut with sharp dies to the symmetric vDENT geometry given in Fig. 8.2a). The span of the fracture process (shown as I, II, and III in Fig. 6.4 for $\dot{u}_i = \{2.5, 25, 250\}$ [mm/min] load rates, respectively) in displacement axis on the given load-displacement curves show this behavior clearly. Also, we noted much smoother crack surfaces in higher rates (cf. [136]). As the loading rates gets smaller, the fracture process takes much longer.

We conducted several laser cut experiments as well and observed much delayed behavior, and extremeley fast and abrubt failures. This can be attributed to an artificial increase of $\mathcal{G}_c$ for the laser-cut lines on the specimens (see the results section for details). Furthermore, also notice a slope in the propagation regime on $\dot{u} = 250$ [mm/min] curve in Fig 6.4. This is evidently supporting a variable propagation characteristic for this rubber specimen in this rate. The effect is almost not present in $\dot{u}_i = \{2.5, 25\}$ [mm/min] experiments. We conclude that, this slope is not related to the inhomogeneous character of the specimens, but due to viscous effects.

CHAPTER 7

VALIDATION EXPERIMENTS ON UNFILLED STYRENE-BUTADIENE RUBBER

In order to validate the theory presented in this thesis, we must explicitly avoid rubber specimens exhibiting strong Mullin's effect [140] or strain crystallization [141]. Both can be mitigated by the choice of unfilled styrene butadiene rubber (SBR) in the experiments. We first characterized the specimens by uniaxial and equibiaxial experiments in quasi-static regime. Furthermore, volumetric compression tests are also conducted to identify bulk modulus. Then, we conducted several relaxation and creep experiments to identify nonlinear viscous model parameters. These conclude the set of experiments required to mechanically identify the specimens. Then, a series of fracture experiments with custom notch geometries are arranged both in quasi-static and high strain rate settings. Notch length is varied in a set of geometrically symmetric fracture specimens, and used for proving the consistencies of criticial energies. Finally, these critical energies are validated on an asymmetric notched specimen geometry in Chapter 8. The fracture specimens utilize a v-type notch as outlined in HEYDARI-MEYBODI ET AL. [136] in a symmetric and asymmetric double edge arrangement. Hence, we named these specimens vDENT. V-type notch increases (due to blunting) the fracture loads and creates a uniaxial stress state at the notch tip for Mode-I type loading. The SBR specimens are provided by *Bayrak Lastik Sanayi ve Ticaret A.Ş.* company in $240 \times 140 \times 2$ [mm$\times$mm$\times$mm] batches produced from the same mold. Furthermore, these geometries are cut using both a punch type *die-cutter* and a *laser-cutter*. Since the fracture loads significantly change due to these cutting types, we reported both results. The variability of the results and the fracture loads are much higher for *laser-cut* specimens. The data of both cutting methods are reported in this work since the author is not aware of a similar experimental work in

literature taking the type of geometry preparation into account. Rupture tests for SBR comprised of three boundary velocities for each geometry and two cutting methods just discussed. Using SONY ZV-E10 video camera with 100 FPS capture settings, we managed to capture the rupture behaviour of asymmetrical and symmetrical specimens for 2.5 mm/min boundary velocity. These snapshots are reported in Chapter 8 for side-by-side comparison to the analyses.

These experimental studies are conducted on a modular *Zwick/Roell Z010* universal testing machine with two video extensometers dedicated specifically to uniaxial and equibiaxial tests. The *TestXpert III* software associated with the test machine is used in implementing experimental protocols, measurements, and control of the testing machine. In the tests, pneumatic grips are utilized and they are mounted between the *Zwick/Roell XForceP* series load cell with 10 [kN] nominal force capacity.

Basic parameters for the compressible extended eight-chain model and the nonlinearly viscous theory are given in this section for the experiments. Fracture related analyses will be discussed and elaborated in Chapter 8.

7.1   Mechanical characterization

In this section, uniaxial tension, equibiaxial tension, and volumetric compression results of in-house experiments on unfilled SBR rubber are given. The experimental procedures are explained in detail.

In the uniaxial tests (Fig.7.2a)), three ISO37 Type 2 [142] geometries are prepared from SBR sheets with 2 [mm] thickness and loaded until rupture. For the equibiaxial tests (Fig.7.2b)), from the same batch, three flower shaped specimens with 2 [mm] thickness are prepared according to the geometry by *Axel Physical Testing Services* [142]. Dimensions and the geometries are given in Fig. 7.3. Both uniaxial and equibiaxial geometries are cut using die-cutters. For both uniaxial and equibiaxial tests 2.5 [mm/min] position controlled test speed is utilized with video extensometer based strain measurements. The value of speed utilized here corresponds to quasi-static behavior (see [43]) for the studied rubber specimens. The experiment results are averaged for uniaxial tension tests. On the other hand, experiment corresponding to the
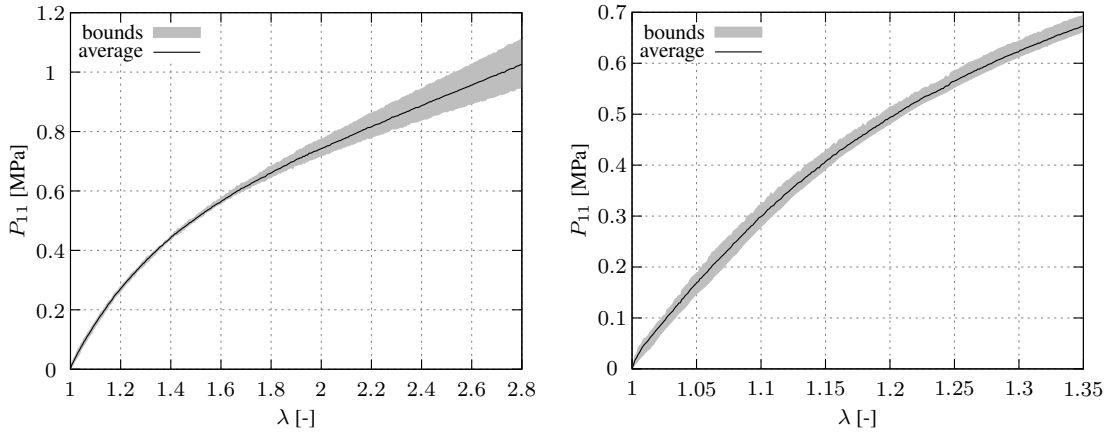
Figure 7.1: (Left) uniaxial and (right) equibiaxial tension experiments at 2.5 [mm/min] speed and their average values.

largest stretch value for the equibiaxial test is considered for the fits, this is for simultaneous fits where the uniaxial and equibiaxial tests are fitted together as in DAL ET AL. [37]. Fig. 7.1 contains the raw data of the (left) UT experiments and (right) ET experiments with confidence bounds and the averages. In the figures, result of the experiments are documented in the sense of stress (first Piola-Kirchhoff stress) versus stretch values.
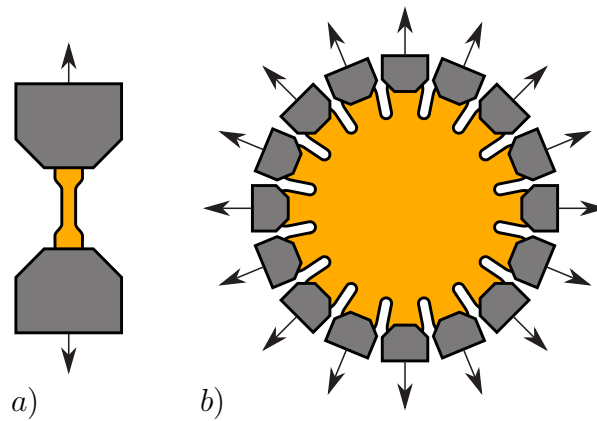
Figure 7.2: Loading for the specimens at $a)$ uniaxial and $b)$ equibiaxial arrangements.

The volumetric compression tests utilizes small $\phi = 6.5$ [mm] cylindrical specimens with 2 [mm] thicknesses. With this geometry, three specimens from the same batch of SBR sheet are cut with a punch cutter. A diagram showing the custom apparatus used in the experiments is given in Fig. 7.5 a). The apparatus, specimen, and slid-
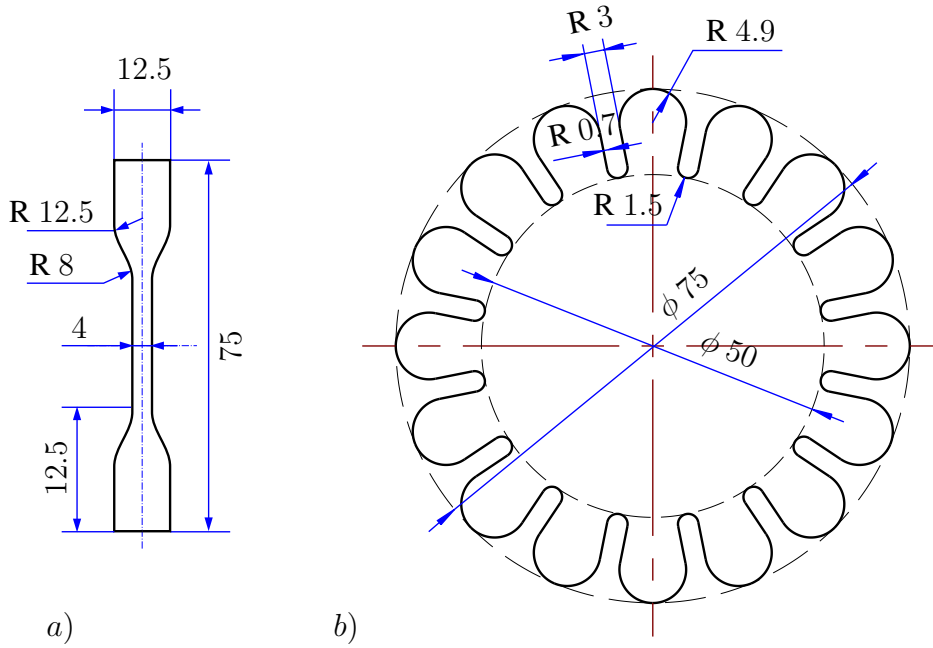
Figure 7.3: The geometries for $a)$ ISO37 Type 2, and $b)$ equibiaxial tests [142]. Thickness of the specimens are 2 [mm].
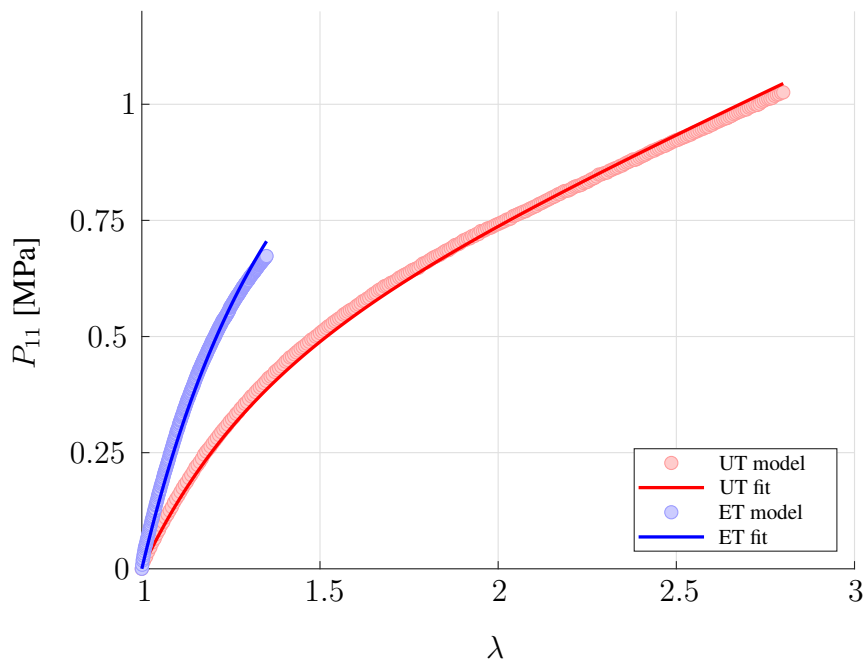
Figure 7.4: Extended eight-chain model fits for uniaxial and equibiaxial tests.

Table 7.1: Extended eight-chain parameters for the experiments on unfilled SBR.

	$\mu\,[MPa]$	$N\,[-]$	$\mu_c\,[MPa]$	$\chi\,[MPa]$
Unfilled SBR	0.34	90.14	0.91	462

ing pin are placed in between fixed and moving cross-heads of the test device. The applied force squeshes the specimens while the amount of stretch and the load are recorded. This loading arrangement forces the material to change volume by restricting the side expansion of the specimens. Since the diameter of the specimens cannot be exactly matching the diameter of the apparatus hole, side expansion on the specimens occur which result in an initial shear-like deformations until the specimen is loaded sufficiently high. After the initial shape-change, the specimens can no longer expand sideways and start to deform volumetrically. The experiment results are provided in Fig. 7.5 b). The measurements result in a steep slope after initial shear-like deformations due to material's near incompressible behavior. Since we expect higher-and-higher loads for increased compression, we ended the experiments at 200 [N] by setting an upper force limit from *TestXpert III* software. This region of the experiments are averaged and fitted with extended eight-chain model. Finally the extended eight-chain model parameters are given in Table 7.1 and the fit results are shown in Fig. 7.4.

7.2   Creep and relaxation tests

The viscous characteristics of the SBR material can be obtained by a series of creep and relaxation tests. In these experiments, uniaxial test specimens are used complying to, again, the ISO37 Type 2 [142] geometry. In the experiments, we utilized the video extensometer of the test machine. In the creep and relaxation experiments, a sharp step like loading is applied until the set stress or stretch values reached, respectively. However, in the physical experiments, the test machine has a speed and acceleration/deceleration limit. In our case, cross-head speed limit is approximately 600 [mm/min], to stay in the safe limit, we utilized a 450 [mm/min] cross-head speed in the tests. For each experiment, the specimen is slowly loaded at 2.5 [mm/min] until
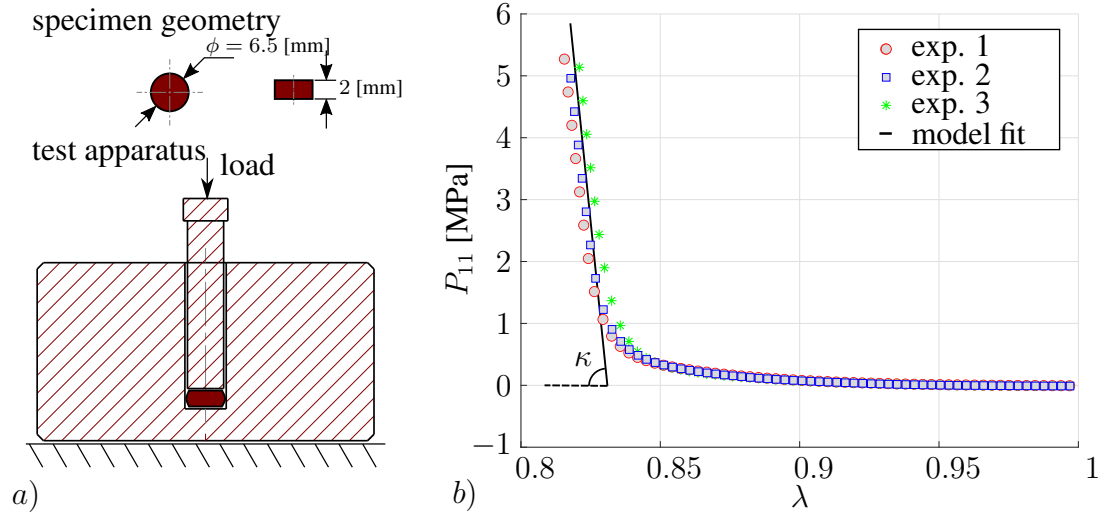
Figure 7.5: a) Specimen geometry and test apparatus, b) the volumetric compression experiment results and extended eight-chain model fit with $\kappa = 463$ [MPa] for unfilled SBR.

the 75 % of the ultimate sresses or stretches according to the test type. This is mainly to cancel the Mullin's effect that could alter the results. Then the 450 [mm/min] step input is applied for the given set value of the experiments.

Creep experiments: For the creep experiments, $P_{11} = \{0.3, 0.6, 0.9, 1.2\}$ [MPa] stress set values are adjusted. After the first slow loading, each set stress is achieved with 450 [mm/min] position controlled speed, and the material holded at the set stress for 10 [min]. Between each test we waited for 15 [min]. A set of 3 experiments are conducted in total for each set value.

Relaxation experiments: For the relaxation experiments, $\lambda = \{1.5, 2, 2.5, 3\}$ [-] stretch set values are adjusted. After the first slow loading, each set stretch is achieved with 450 [mm/min] position controlled speed, and the material holded at the set stretch for 10 [min]. Between each test we waited for 15 [min]. A set of 3 experiments are conducted in total for each set value.

The results of the experiments and the fits are given in Fig 7.6 and Fig 7.7 for relaxation and creep respectively. For parameter optimization, the ground state behavior is fixed from UT and ET experiments as given in Table 7.1. Then, the viscous parameters are fitted manually over the creep and relaxation data. In order to carry out

Table 7.2: Viscous parameters for the unfilled SBR material. These parameters simultaneously fit 4 creep and 4 relaxation set values.

	Parameters for the Maxwell branches.				
	χ^v [MPa]	μ^v [MPa]	N^v [-]	$\dot{\gamma}_0/\hat{\tau}_m$ [MPa^{-m}s^{-1}]	m [-]
1st Maxwell branch	462	0.12	90	150	1
2nd Maxwell branch	462	0.05	90	1	3

the fits, a script file has been generated where the set viscous parameters are tested over 4 creep and 4 relaxation set levels simultaneously. A single Maxwell branch was not enough, therefore, we utilized two Maxwell branches. The number of segments are taken equal to the ground state number of segments to reduce the number of parameters. The optimized parameters are given in Table 7.2.
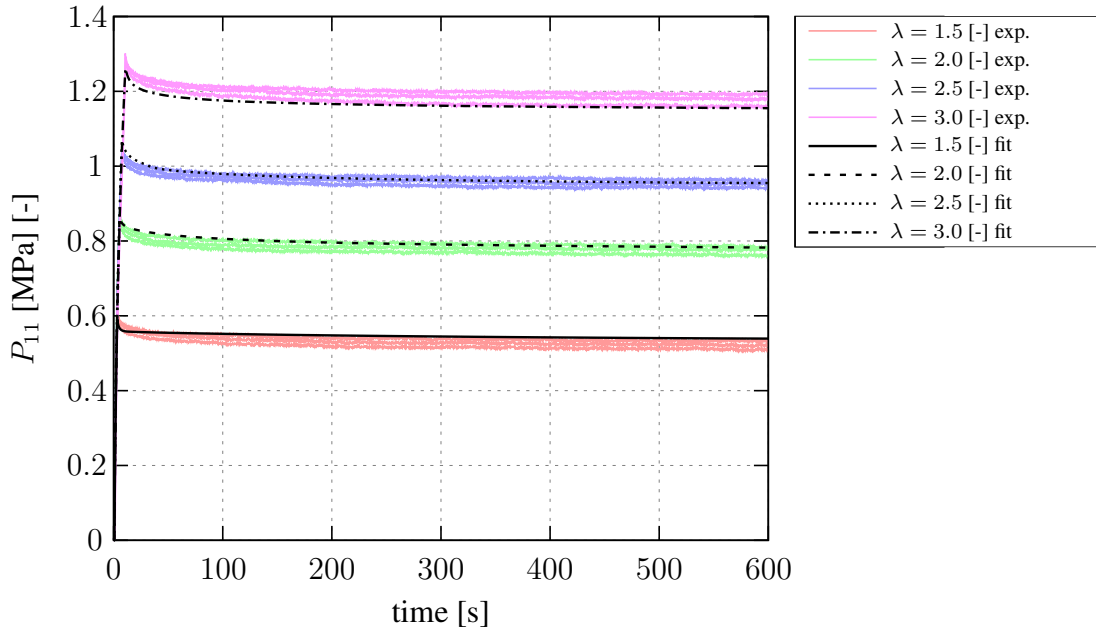
Figure 7.6: Relaxation tests at set stretch values of $\lambda = \{1.5, 2.0, 2.5, 3.0\}$ [-] and the simultaneous fit results for the parameters given in Table 7.2.
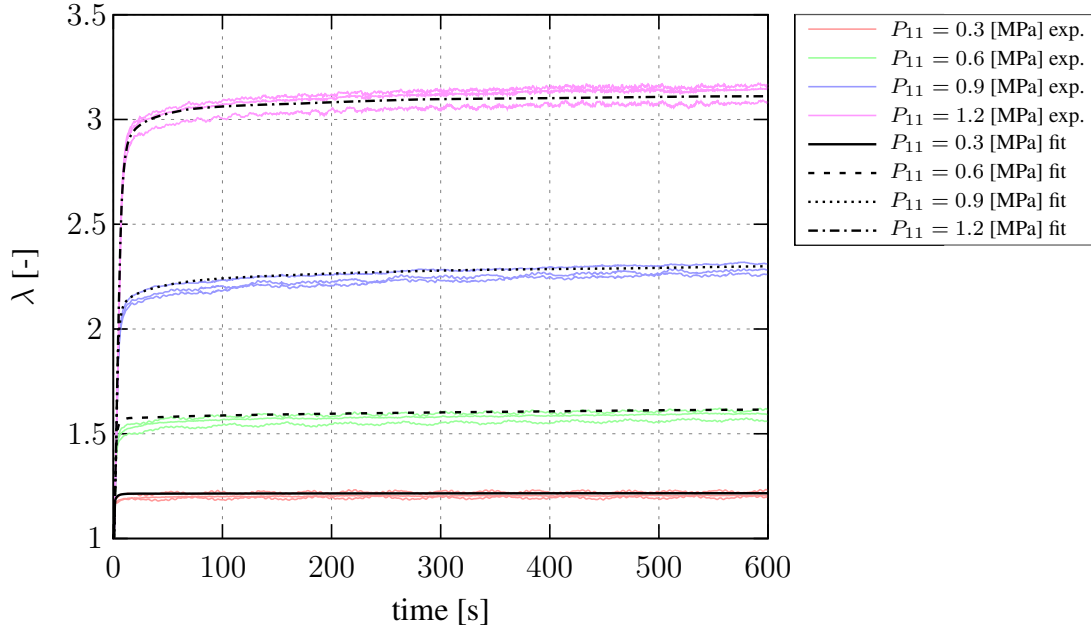
Figure 7.7: Creep tests at set stress values of $P_{11} = \{0.3, 0.6, 0.9, 1.2\}$ [MPa] and the simultaneous fit results for the parameters given in Table 7.2.

7.3 Fracture tests for symmetric and asymmetric geometries

As we would like to calibrate Ψ_{cr}^{e} values, we have conducted fracture experiments on two different geometries. The symmetric geometry, see Fig. 7.8 a), serves as the calibration tests where the notch length is varied. The asymmetric geometry, see Fig. 7.8 b), on the other hand, is tested for validation. In these experiments, 2.5 [mm/min] test speed is applied to obtain quasi-static condition. The geometries are obtained through both laser-cutting and die-cutting. The *laser-cut* geometries are obtained in 3 cycles at 80% load with 100 [mm/min] speed in an 80 [Watt] CO_2-laser. Special press type dies are used for die-cutting. The experiment results for both cutting methods are given in this section. Furthermore, to validate the viscous failure criterion given in 6.4, two different clamp velocities (or cross-head speeds) are used for symmetric specimen geometry given in Fig. 7.8 a). These set values are taken as 10 times, and 100 times of the quasi-static case, i.e., $\dot{u} = \{25, 250\}$ [mm/min] and repeated three times. These high strain rate tests are conducted only on specimens obtained by *die-cutting*.
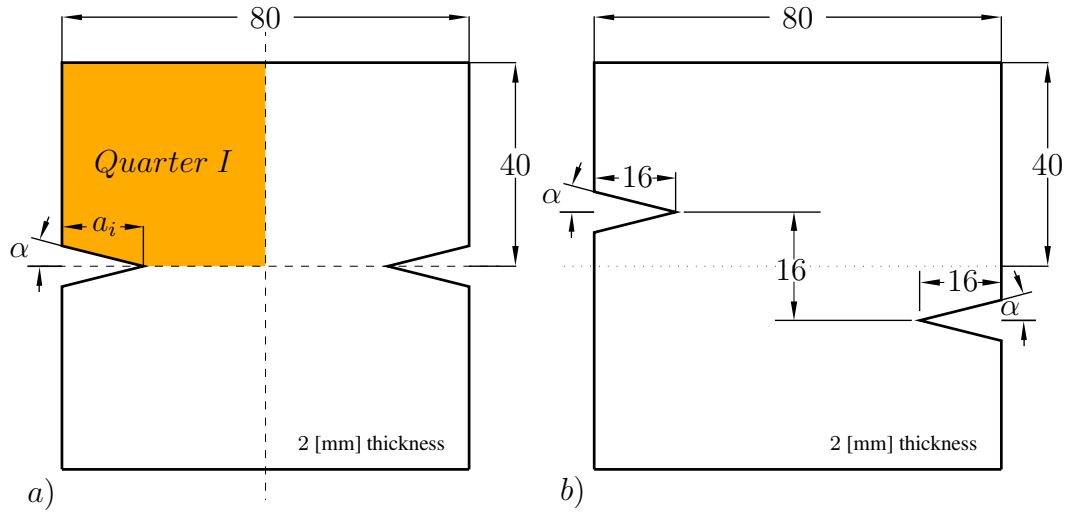
Figure 7.8: a) Symmetric simple notched test specimen dimensions. Dashed lines are symmetry axes. The notch lengths are taken to be $a_i = \{16, 20, 24\}$. In the simulations only the half the thickness of the first quarter is considered by utilizing symmetries. b) The same sized specimen with asymmetrically placed notches. All units are in $[mm]$. The angle α is kept constant at $\tan^{-1}(1/4)$.

Symmetric geometry obtained by *laser* For these experiments, 2.5 [mm/min] clamp velocity is utilized. The results encompasses 3 notch lengths $a_i = \{16, 20, 24\}$ [mm] as given in Fig. 7.8 a), each repeated 3 times. The load-displacement curves for these experiments are given in Fig. 7.9(a).

Asymmetric geometry obtained by *laser*: For these experiments, 2.5 [mm/min] clamp velocity is utilized. The geometry is as given in Fig. 7.8 b). These are repeated 3 times. The load-displacement curves for these experiments are given in Fig. 7.9(c).

Symmetric geometry obtained by *die-cutting*: For these experiments, 2.5 [mm/min] clamp velocity is utilized. The results encompasses 3 notch lengths $a_i = \{16, 20, 24\}$ [mm] as given in Fig. 7.8 a), each repeated 3 times. The load-displacement curves for these experiments are given in Fig. 7.9(b).

Asymmetric geometry obtained by *die-cutting*: For these experiments, 2.5 [mm/min] clamp velocity is utilized. The geometry is as given in Fig. 7.8 b). These are repeated 3 times. The load-displacement curves for these experiments are given in Fig. 7.9(d).
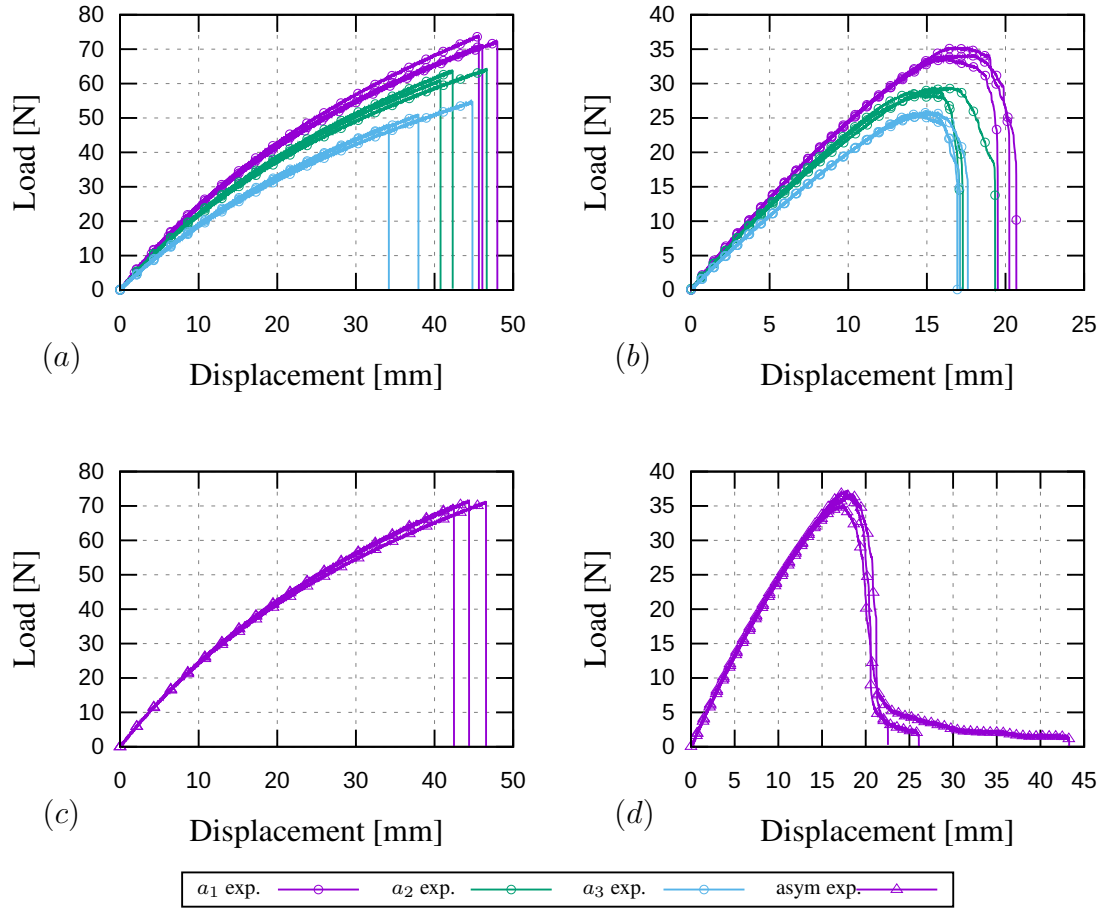
Figure 7.9: Load-displacement curves of fracture experiments for (a) symmetric *laser-cut* specimens with notch lengths $a_i = \{16, 20, 24\}$, (b) symmetric *die-cut* speciments with notch lengths $a_i = \{16, 20, 24\}$, (c) asymmetric *laser-cut*, and (d) asymmetric *die-cut* specimens. Each experiment type is repeated three times.

High strain rate tests with *die-cut* symmetric geometries: For these experiments, $\dot{u} = \{25, 250\}$ [mm/min] clamp velocities are utilized. Each repeated three times. The load-displacement curves for these experiments are given in Fig. 7.10.

REMARKS: These conclude the set of experiments for the study. The following remarks are experimental observations and encountered phenomena.

- The *laser-cut* specimens exhibit much larger fracture toughness, as can be seen from both symmetric and asymmetric test results Fig. 7.9(a, c) compared to Fig. 7.9(b, d), respectively.
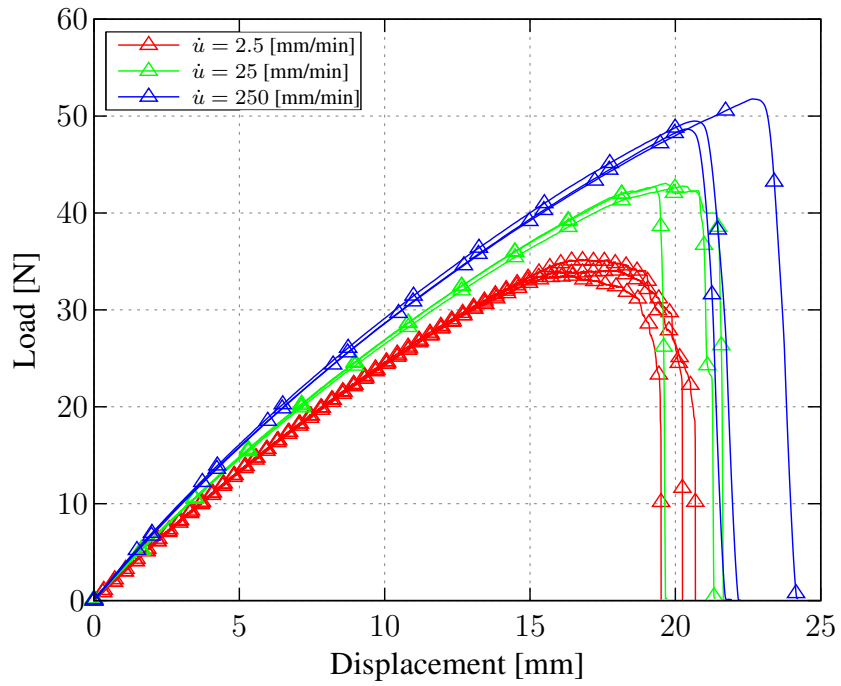
Figure 7.10: Load displacement curves for *die-cut* symmetric specimens at $\dot{u} = \{2.5, 25, 250\}$ [mm/min] clamp speed.
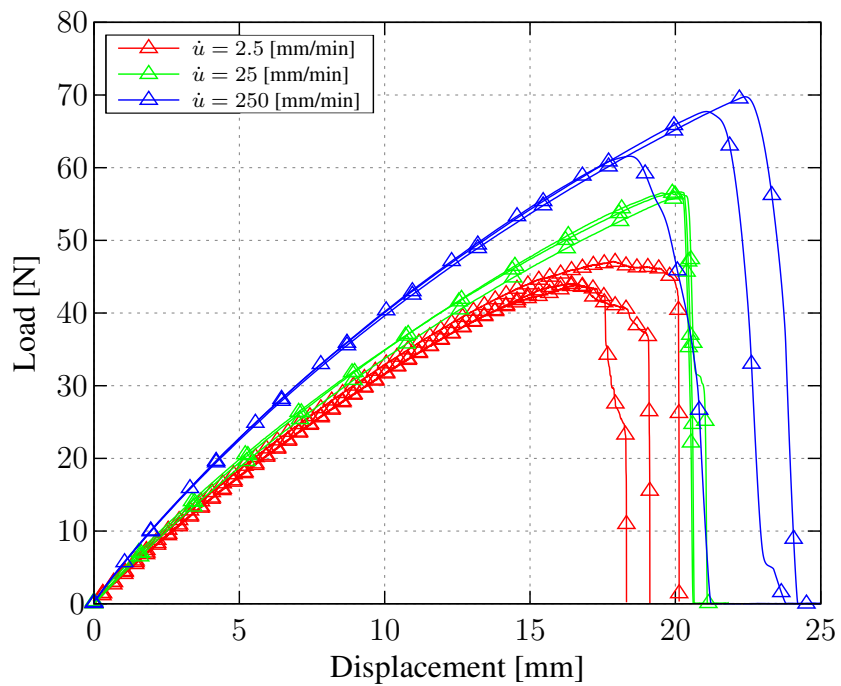
Figure 7.11: Load displacement curves for *die-cut* symmetric unfilled NBR specimens at $\dot{u} = \{2.5, 25, 250\}$ [mm/min] clamp speed.

- The *laser-cut* specimens exhibit extremely abrubt failure. The fracture initiates at one of the notches and suddenly proceeds to around the other notch without allowing failure at the other notch. The failure is catastrophic and almost instantaneous.

- In the *die-cut* experiments fracture initiates at one of the notches, proceeds considerably slowly and sometimes stagnant for a while. Before complete failure, fracture also initiates at the other notch. In both symmetric and asymmetric geometries, late initiation of fracture at one of the notches results in complex crack paths. The secondary crack initiation is more evident in *die-cut* asymmetric specimens and exhibits itself in load-displacement curves Fig. 7.9(*d*) with a late long-lasting ductile behavior before complete failure.

- The crack paths observed in *die-cut* symmetric specimens are jagged and do not follow a straight path. This indiciates a non-homogeneous distribution of energy release rate within the specimen, yet these specimens are high quality and the material is unfilled. We can observe such behavior in HOCINE ET AL. [143]. Material does not catastrophically fail instantly, shows a behavior similar to ductile fracture. This behavior is extremely important for fatigue crack growth simulations with phase-field approach.

- We note that, v-type double edge notch geometries (vDENT) provide quite the opposite results of double edge straight notch specimens of LOEW ET AL. [95]. vDENT specimens show significant increase in displacement at fracture as the clamp-velocity increases. In a double edge straight notch geometry, the crack tip blunting effects won't be significant to alter the viscous behavior. However, vDENT geometries have significant blunting before the crack propagation and this effect seems to be pronounced as the clamp-velocity increases and results in a delayed crack formation. In order to make sure that this effect is only about the geometry and not related to material, we conducted $\dot{u} = \{2.5, 25, 250\}$ [mm/min] experiments on unfilled NBR as well, whose load-displacement curves are give in Fig.7.11. The vDENT geometry seems to be the main reason. However, for this very reason the blunting takes effect at material level in our theory, as it is not resolved in geometry for simulations, and forces the theory to utilize negative β_v values in 6.4. With positive β_v

values, the theory can capture the experimental results of Loew Et Al. [95].

CHAPTER 8

REPRESENTATIVE BOUNDARY VALUE PROBLEMS AND RESULTS

In this section, we demonstrate the utility of the proposed phase-field approach by solving several boundary value problems (BVP). The contribution's performance is assessed through comparison with not only the in-house experiments, but also the experiments from literature. The experiments themselves are considered as BVPs since the geometries of the specimens in the experiments are representative enough for this assessment. The following cases are considered as simulations in that regard,

- experiments on symmetrically notched specimens by HOCINE ET AL. [143] to validate the theory on an established dataset from literature,

- in-house fracture experiments on symmetrically notched *die-cut* and *laser-cut* specimens with varying notch lengths,

- in-house fracture experiments on asymmetrically notched *die-cut* and *laser-cut* specimens,

- in-house fracture experiments on varying strain rates for symmetrically notched *die-cut* specimens.

In the simulations of these boundary value problems, an academic **F**inite **E**lement **A**nalysis **P**rogram (FEAP) [144] is utilized. A material routine for compressible extended eight-chain model along with the nonlinearly finite viscoelastic theory DAL ET AL. [43] has been implemented. For the phase-field part, a Q1 ([145]) based formulation has been implemented as element routine and coupled with the material routine through stress and tangent modulus degradation. The ease of use and extendability of FEAP allowed faster theory implementation in this thesis, for instance, that would

be otherwise as compared to commercial alternatives, e.g., ABAQUS ([146]). We utilized the toolbox presented in DAL ET AL. [37] to identify the material parameters in compressible extended eight-chain model.

8.1 Double edge notched specimens by HOCINE ET AL. [143]

The critical fracture energies for a double edge notched specimens (DENT) for SBR were reported by HOCINE ET AL. [143]. In their work, symmetric DENT specimens' load-displacement curves are provided for tensile experiments at different notch lengths. These experiments can be used as a benchmark for the behavior of the generalized phase field model under entropic fracture conditions. In the experiments, they considered $w = 80$ [mm] width by $h = 200$ [mm] length specimens with 3 [mm] thicknesses.

In the simulations the geometry is modeled by considering symmetries and only 1/8th of the total geometry is meshed. For this material, in the extended eight-chain model $\mu = 0.175$ [MPa], $N = 500$, and $\mu_c = 0.465$ [MPa] are taken. κ is set to 150μ during the simulations to prevent volumetric locking. The degradation function for the entropic part is taken as $\theta = 0.01$, and $\alpha = 2$ while the volumetric part is set to $\alpha = 3$, and $\theta = 2$. The overall geometry is meshed with 1400 elements in 3D for 1/8th (quarter of the surface and half the thickness) of the geometry, where in the critical fracture area, the average mesh size $h = 0.03$ [mm] is obtained. The length scale parameter l is set to 0.1 which corresponds to approximately 3 elements in the direction perpendicular to crack path. The critical entropic energy is fitted as $\psi_{cr}^e = 2.15$ [MPa/m³]. The load displacement curves and the generalized phase-field model fits are shown in Fig. 8.1 for all notch lengths.

In these experiments, the notch geometry is different in comparison to the ones we utilized. In their set of experiments, the notches were created by hand using a scalpel. We can see a platau before catastrophic failure in the load-displacement curves given in Fig. 8.1. This is much to our surprise, as investigated further in the next sections, due to varying critical energy release rate over the specimen,i.e., due to inhomogeneities. We conducted our set of experiments similar to HOCINE ET AL. [143]

94

using specially designed die cutters with the geometries given in Fig. 8.2. For the experiments, in order to punctuate the robustness of the theory presented in this thesis, we utilized a laser cutter to obtain the same geometries. Therefore, we present two sets of data, one for *die-cut* geometries, and one for *laser-cut*. The laser-cut specimens exhibit considerably larger ψ^e_{cr} values when fitted. Therefore, they present larger displacements before rupture and can be used to show the effectiveness of the theory. We utilized $l = 1$ [mm] for the length scale in the rest of the simulations. Thus, we use ψ^e_{cr} as material parameter instead of $\mathcal{G}^e_c$ throughout this section.
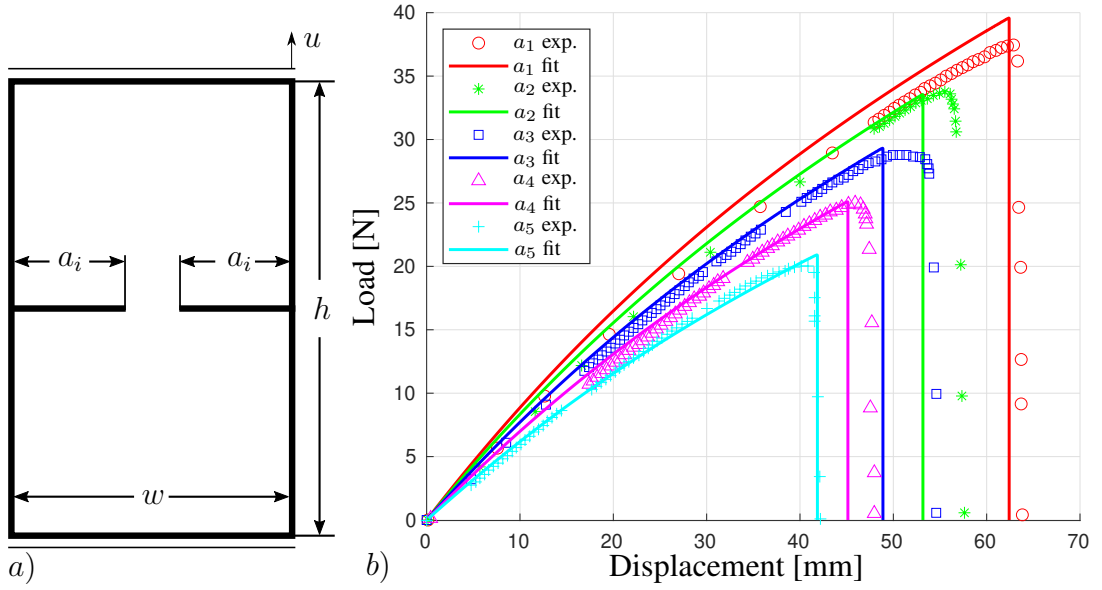
Figure 8.1: Symmetric DENT specimen geometry for [143] experiments where $w = 80$ [mm] and $h = 200$ [mm]. The notch lengths are $a_i = \{12, 16, 20, 24, 28\}$. In the simulations only the half the thickness of the first quarter is considered by utilizing symmetries.

8.2 Simulation results for custom vDENT experiments

In this section, we analyzed a set of simulations on both *die-cut* and *laser-cut* specimens and compared the results to the corresponding experiments. The striking difference on the cricital entropic energy values for these two types of experiments show that, the generalized phase-field model can capture the varying notch-length simula-

tion results once we fit one of the notch lengths through simulations for both cases. The considered custom geometries are given in Fig. 8.2. The symmetric geometry has three different notch lengths, i.e., $a_i = \{16, 20, 24\}$ [mm]. Asymmetrically notched vDENT geometry has only one notch length and it is used to provide a further condition of proving the theory.
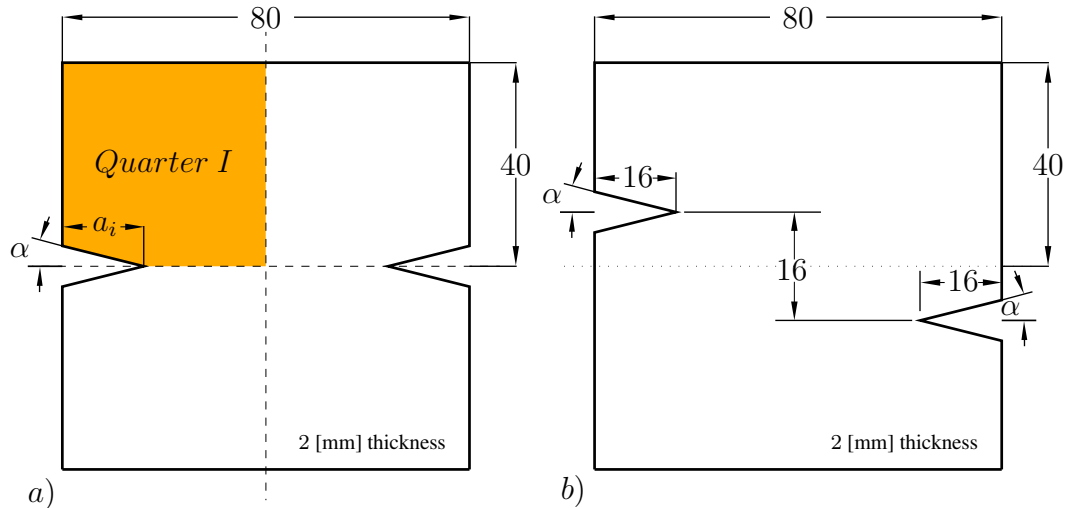
Figure 8.2: a) Symmetric simple notched test specimen dimensions. Dashed lines are symmetry axes. The notch lengths are taken to be $a_i = \{16, 20, 24\}$. In the simulations only the half the thickness of the first quarter is considered by utilizing symmetries. b) The same sized specimen with asymmetrically placed notches. All units are in $[mm]$. The angle α is kept constant at $\tan^{-1}(1/4)$.

We named these experiments vDENT (v-shape double edge notched tensile) and preferred the v-shape notches (see [136]) since they provide a more homogeneous response around the notch tip or the process zone, compared to a straight edge notch (as in [143]). Also note that we used special cutting dies for each notch length and asymmetric geometry and a press to have consistent notches across all the specimens. The *laser-cut* geometries are obtained in 3 cycles at 80% load with 100 [mm/min] speed in an 80 [Watt] CO_2-laser. The extended eight-chain model parameters for the rest of the simulations are summarized in Table 8.1. Note that, these values are fitted from UT and ET experiments simultaneously using the framework provided in [37]. The simultaneous fits have the advantage of exhibiting meaningful (or non-diverging) stretch-stress responses under both UT and ET loading conditions, which is a prereq-

uisite for this theory to work in multiaxial loading conditions.

Table 8.1: Extended eight-chain parameters for the experiments on unfilled SBR.

	$\mu\,[MPa]$	$N\,[-]$	$\mu_c\,[MPa]$	$\chi\,[MPa]$
Unfilled SBR	0.34	90.14	0.91	462 (50)

Also note that all the geometries in Fig. 8.2 have 10 [mm] additional space at top and bottom to create holding surfaces for the pneumatic grips of the test machine.

Rupture tests for SBR comprised of three boundary velocities (clamp velocities) for each geometry and two cutting methods for specimen preperation. Using SONY ZV-E10 video camera with 100 FPS capture settings, we managed to capture the rupture behaviour of asymmetrical and symmetrical specimens under 2.5 mm/min boundary velocity. For the symmetrical geometry, we observed that crack propagated at $t = 1284.93[s]$. Propagation of the crack occured under a second, as shown in Fig. 8.3(e). Post-mortem state of the specimen exhibited a straight line pattern, in agreement with the simulation results shown in Fig. 8.7. For the asymmetrical *laser-cut* specimen, propagation began at $t = 1372.71[s]$ (Fig. 8.4). Similar to the symmetrical geometry, crack propagated almost instantly and advanced in 3 miliseconds, eventuating catasthropic failure. Due to the difference in critical entropy between sides, we observed that the crack propagated from one side to the other. Since the failure is catasthropic, it is not within reach to conceive the propagation of the crack from the other side. According to Fig. 8.5 and Fig. 8.6, *die-cut* specimens differed from the *laser-cut* specimens both in terms of propagation pattern and duration. Crack propagation of the symmetrical *die-cut* specimen began at $t = 381.09$ [s], which is significantly earlier than the *laser-cut* counterpart. A reason for the difference can be due to the boundary acting as a barrier because of the cauterizing effect of heat provided by the laser. Another reason can be the irregularities created by the die blade, resulting in microcracks rendering the specimens susceptible to early failure. After crack propagation starts, it is seen that cracks at both notches propagate from their respective sides, although not equal in size and shape because of the difference between critical entropies. Crack propagation took remarkably longer, since catas-
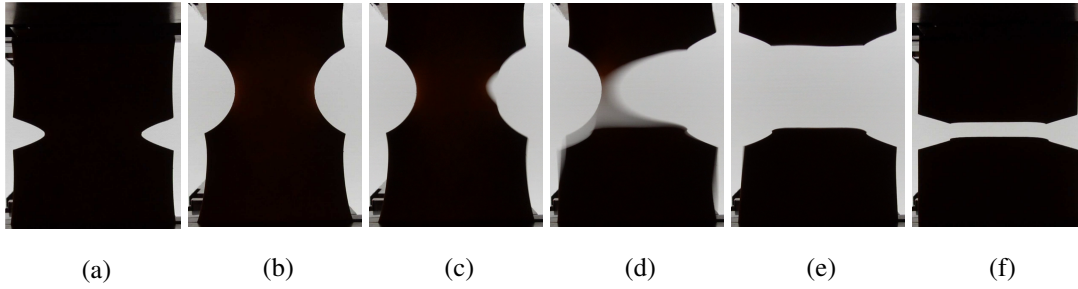
Figure 8.3: The snapshots for the crack propagation of *laser-cut* symmetric specimen under tensile rupture test at 2.5 mm/min boundary velocity, showing specimen (a) at undeformed state $t = 0$, (b) just before rupture $t = 1284.93$ [s], (c) at $t = 1284.94$ [s], (d) at $t = 1284.95$ [s], (e) at $t = 1284.96$ [s], and (f) post-mortem picture.
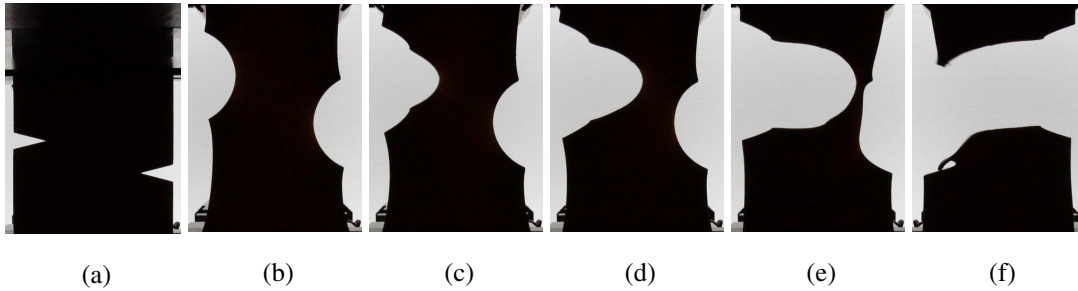
Figure 8.4: The snapshots for the crack propagation of *laser-cut* asymmetric specimen under tensile rupture test at 2.5 mm/min boundary velocity, showing specimen (a) at undeformed state $t = 0$, (b) just before rupture $t = 1372.71$ [s], (c) at $t = 1372.72$ [s], (d) at $t = 1372.73$ [s], (e) at $t = 1372.74$ [s], and (f) post-mortem picture.

trophic failure occured in later stages. As the propagation in the *die-cut* specimens occured continuously, it is also observed that the crack sometimes acted in such a way that it did not propagate for relatively long durations. Propagation patterns were different from that of *laser-cut* specimens. Due to inclusions present in the SBR, crack occured in comparatively irregular patterns. In our point of view, this phenomenon must be investigated as it stands extremely important to fatigue crack growth. One way of approaching such a problem would be an elaborate extension of the present

theory (see [139]) with a stochastically defiend ψ_{cr}^e field. However, such an endeavor has not been pursued in this study.
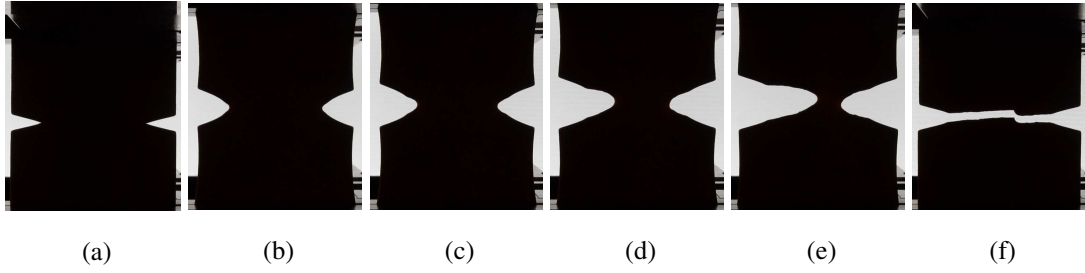
Figure 8.5: The snapshots for the crack propagation of *die-cut* symmetric specimen under tensile rupture test at 2.5 mm/min boundary velocity, showing specimen (a) at undeformed state $t = 0$, (b) just before rupture $t = 381.09$ [s], (c) at $t = 423.05$ [s], (d) at $t = 478.06$ [s], (e) at $t = 486.95$ [s], and (f) post-mortem picture.
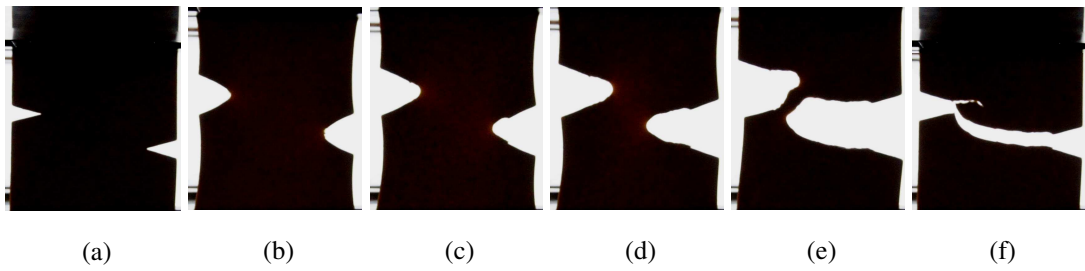
Figure 8.6: The snapshots for the crack propagation of *die-cut* asymmetric specimen under tensile rupture test at 2.5 mm/min boundary velocity, showing specimen (a) at undeformed state $t = 0$, (b) just before rupture $t = 418.82$ [s], (c) at $t = 469.94$ [s], (d) at $t = 499.49$ [s], (e) at $t = 530.42$ [s], and (f) post-mortem picture.

8.2.1 Symmetric vDENT specimens with varying notch lengths

In this simulation, the custom notch geometry given in 8.2 where $a_1 = 16$ [mm] is simulated and crack is propagated up to complete rupture. In the simulations, the unfilled SBR material parameters are utilized as given in Table 8.1.However, the bulk

modulus is taken roughly as $\kappa = 150\mu$ to prevent volumetric locking of the elements. Half of the thickness of the quarter of the geometry is meshed with 1400 elements, where in the critical fracture area, the average mesh size $h = 0.15$ [mm] is obtained. The length scale parameter is adjusted to be $l = 1$ corresponding to approximately 7 elements in the direction perpendicular to crack path. For the simulation, a proportional displacement is applied at the top surface and the bottom surface is fixed utilizing symmetry conditions. We relaxed the mesh at top and bottom surfaces in thickness direction to avoid finer mesh quality around load application surface. In this simulation, entropic critical energies $\psi_{cr}^e = 2.3$ [MPa/m^3] for *laser-cut* specimens and $\psi_{cr}^e = 0.32$ [MPa/m^3] for *die-cut* specimens are fitted based on the experiments of varying notch lengths (16, 20 and 24 [mm]). The degradation function for the entropic part is taken as $\theta = 0.01$, and $\alpha = 2$ while the volumetric part is set to $\alpha = 3$, and $\theta = 2$. The crack path evolution in Lagrangian and Eulerian meshes are provided in Fig. 8.7. The corresponding load displacement curve for the simulation is given in Fig. 8.8(a).
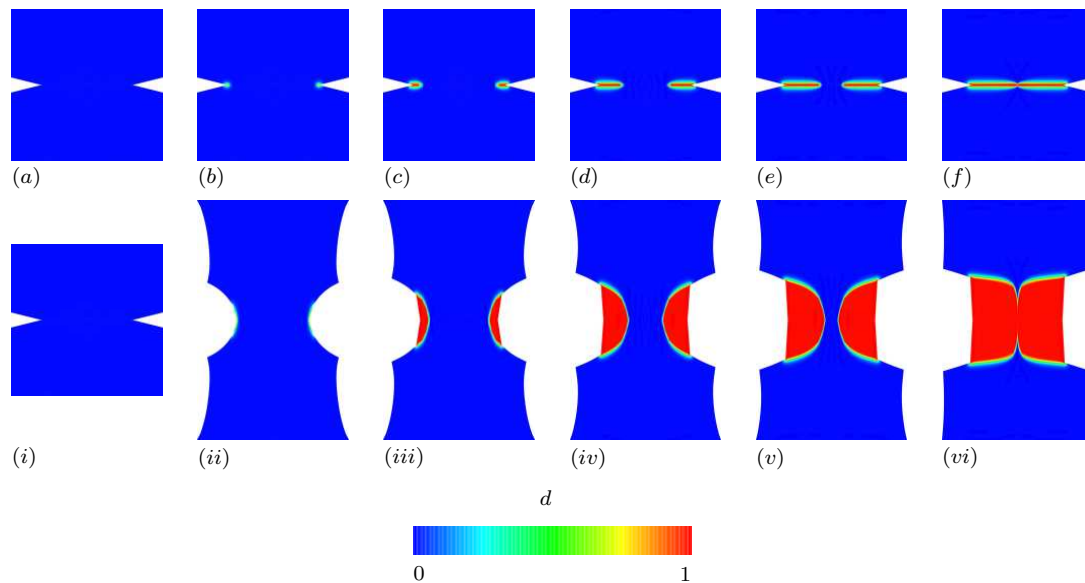
Figure 8.7: Snapshots of rupture simulation results for symmetric *laser-cut* specimens $(a - f)$ in Lagrangian, and $(i - vi)$ in Eulerian configurations.

Since the equibiaxial experiments with the in-house universal testing machine cannot provide accurate conditions for rupture, the true ultimate stretches by our equibiaxial
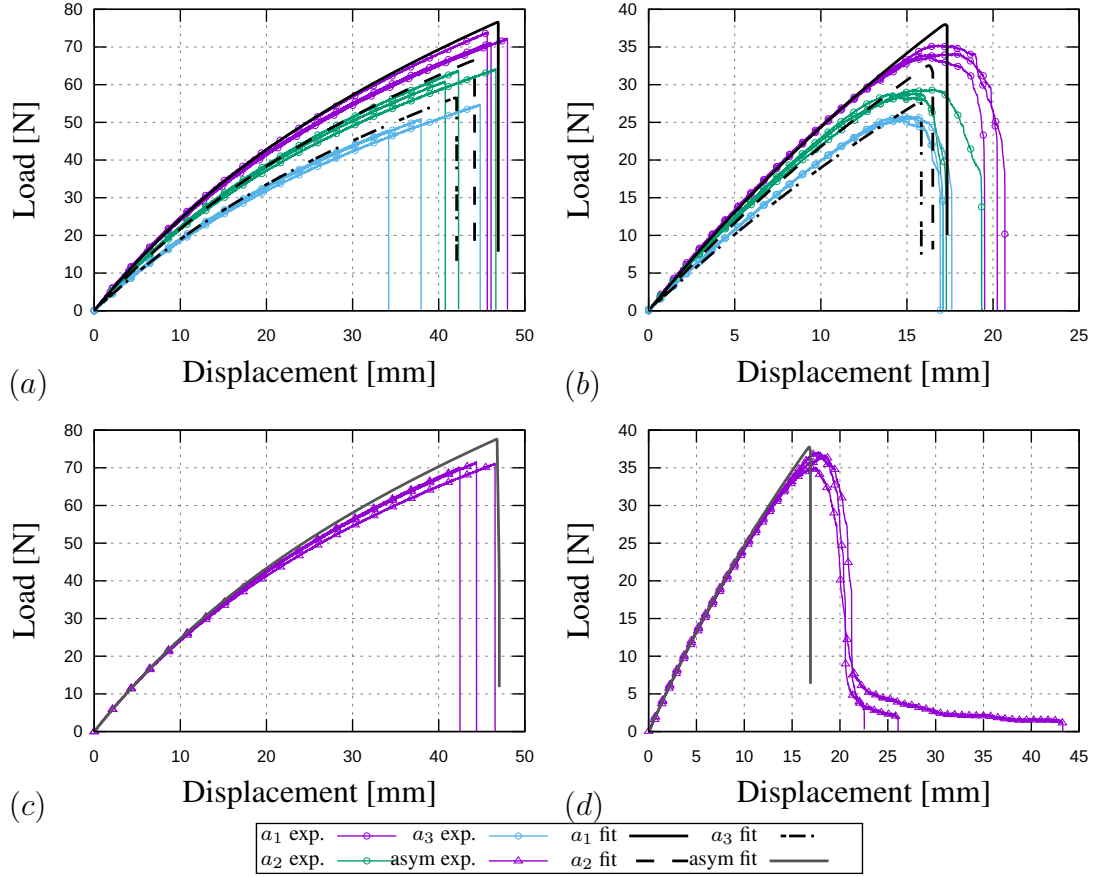
Figure 8.8: Model predictions for (a) symmetric *laser-cut* specimens with notch lengths $a_i = \{16, 20, 24\}$, (b) symmetric *die-cut* speciments with notch lengths $a_i = \{16, 20, 24\}$, (c) asymmetric *laser-cut*, and (d) asymmetric *die-cut* specimens.

test device cannot be obtained and α_c parameter cannot be determined. In order to obtain accurate ultimate stretches in equibiaxial loading, an inflation type test apparatus is needed (see [130] and [128]). The equibiaxial tests, in this study, therefore, are utilized only for material parameter optimization for extended eight-chain model. With this in mind, an α_c value of 1 is chosen for the phase-field part, which represents equal amount of contributions of free-chain and constraint parts to the total entropic free energy. In the simulations, an artificial stiffness of $k = 10^{-4}$ is used to provide better convergence after crack initiation. The artificial viscosity parameter is set to $\eta = 10^{-6}$. The test speed for the corresponding experiments meant to be quasi-static and chosen as low as possible, i.e., 2.5 [mm/min]. Thus, the viscoelastic part in the simulation code is negligible. Note that the overall geometry is recovered in Fig. 8.7

by symmetry through postprocessing. The fits as load-displacement curves for the rest of the notch lengths are given in Fig. 8.8(a) for *laser-cut* specimens and in Fig 8.8(b) for *die-cut* specimens along with this simulation for comparison. All parameters are taken equal for varying notch length simulations. We note the difference of ψ_{cr}^e values of aforementioned HOCINE ET AL. [143] simulation and our die-cut simulation. This is mainly due to taking $l = 0.1$ [mm] in the previous simulation. In comparison to [143], this is expected also as we factor in the specimens' notch shapes, heights, and thickness differences.

In our *laser-cut* experiments, we observe more abrubt (or brittle) fractures in load-displacement curves (cf. Fig. 8.1 to Fig. 8.8(a) and Fig. 8.8(b)). We can attribute this to laser cutting, which makes the notches artificially more stiff (compared to a *die-cut* geometry where micro notches and grooves can be introduced which would make it easier to initiate fracture) and offsets the crack initiation point further on the displacement axis which results in more energy storage until rupture, in turn we can see more abrubt ruptures in our *laser-cut* experiments.

8.2.2   Asymmetric vDENT specimens

In this part, the custom asymmetrically notched geometry given in Fig. 8.2 b) is simulated and crack is propagated up to complete rupture. In the simulations, the unfilled SBR material parameters are utilized as given in Table 8.1 and κ is similarly set to 150μ. In the simulations $k = 10^{-3}$ is used to provide numerical stability during crack propagation. As in the previous section, $\eta = 10^{-6}$ is taken. In this simulation, half of the thickness of full geometry is meshed with 2950 elements. Around the crack path average mesh size of $h = 0.13$ [mm] is obtained. Length scale parameter is taken as $l = 1$ [mm]. Since we conducted experiments of this simulation at 2.5 [mm/min], the effect of viscoelastic part on the simulations is negligible.

Here, we considered two scenarios; (i) in the first scenario, ψ_{cr}^e is taken 2.3 [MPa/m^3] based on the symmetric calibration tests given in the previous section and same everywhere throughout the entire geometry, and (ii) in the second scenario, we applied a different ψ_{cr}^e (twice as large, i.e., as 4.6 [MPa/m^3]) value at around one of the notches as shown in Fig. 8.9. Based on the experiments, it can be deduced that the fracture
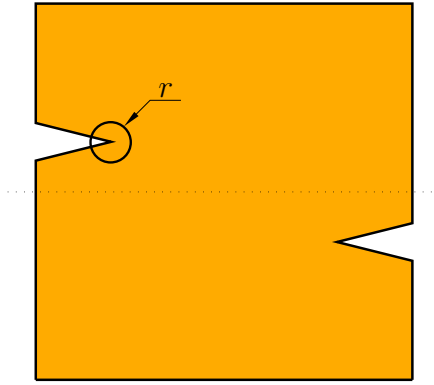
Figure 8.9: The asymmetric geometry where a different ψ_{cr}^e is applied within the marked region of radius $r = 1$ [mm].

characteristics at both notch tips are not equal. Therefore, crack initiates from one of the notches earlier and prevents rupture from the other notch as the rupture is quite sudden due to the effect of cutting the geometry by laser, an interesting phenomenon, which we explored in the second scenario. Note that, in the following two examples, we utilized the same mesh. For both simulations, the load-displacement characteristics are the same and as shown in Fig. 8.8(c). However, the crack path changes drastically. Interestingly, we observed the same crack path as in 2$^{\text{nd}}$ scenario in experiments for laser cut geometry. The crack paths for blade cut geometry is more representative for 1$^{\text{st}}$ scenario and we can see in the snapshots that cracks are initiated at both notches, however, it seems there still exists a difference for ψ_{cr}^e on the notches, thus fracture instantiates at one of the notches earlier. These scenarios are aggreable to experiments both in terms of crack path and load-displacement curves. Finally, we provided the blade cut experiment data and its fits for comparison in Fig. 8.8(d).

(i) homogeneous ψ_{cr}^e for entire geometry The *die-cut* geometries exhibit close (with respect to laser cut geometries) notch tip ψ_{cr}^e values according to the experiments. The cracks are initiated at both notches throughout the experiments. The base behavior of the theory presented in this thesis is tested in this simulation. The simulation results for these are shown in Fig. 8.10 where the cracks emerges from both sides simultaneously and meets at the geometric center of the specimen. The load-displacement curve is as given in Fig.8.8(c), the snapshots of one of the experiments is given in Fig. 8.6.

103
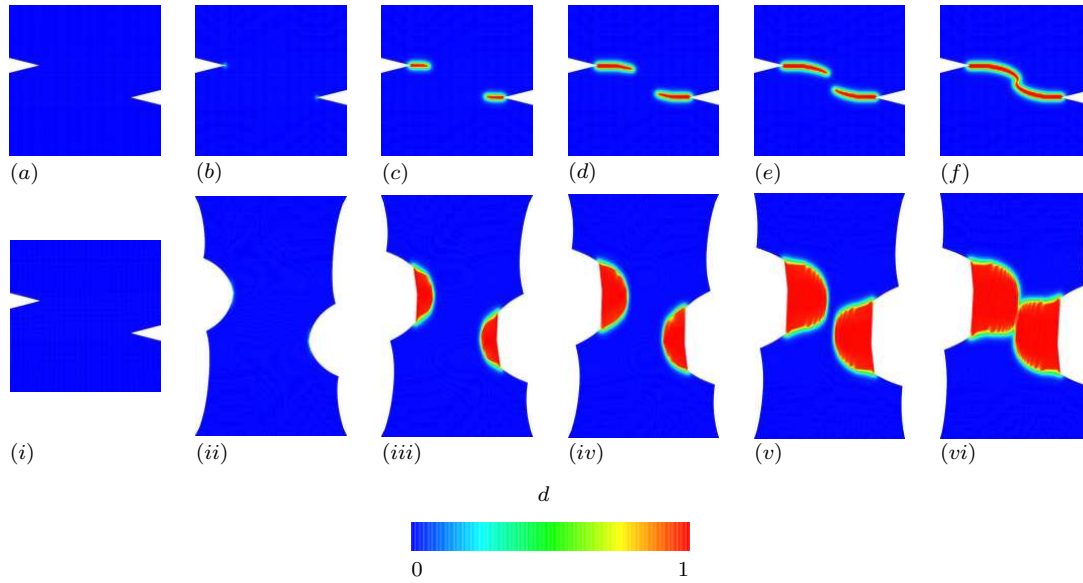
Figure 8.10: Snapshots of rupture simulation results for asymmetric *laser-cut* specimens for homogeneous ψ^e_{cr} distribution $(a-f)$ in Lagrangian, and $(i-vi)$ in Eulerian configurations.
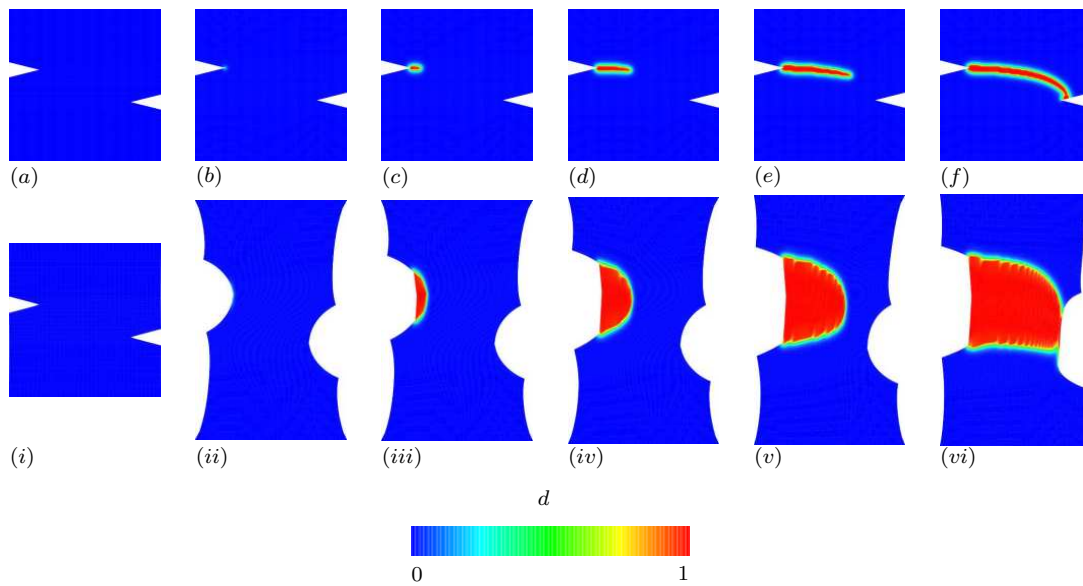
Figure 8.11: Snapshots of rupture simulation results for asymmetric *laser-cut* specimens for twice as large ψ^e_{cr} at right notch $(a-f)$ in Lagrangian, and $(i-vi)$ in Eulerian configurations.

104
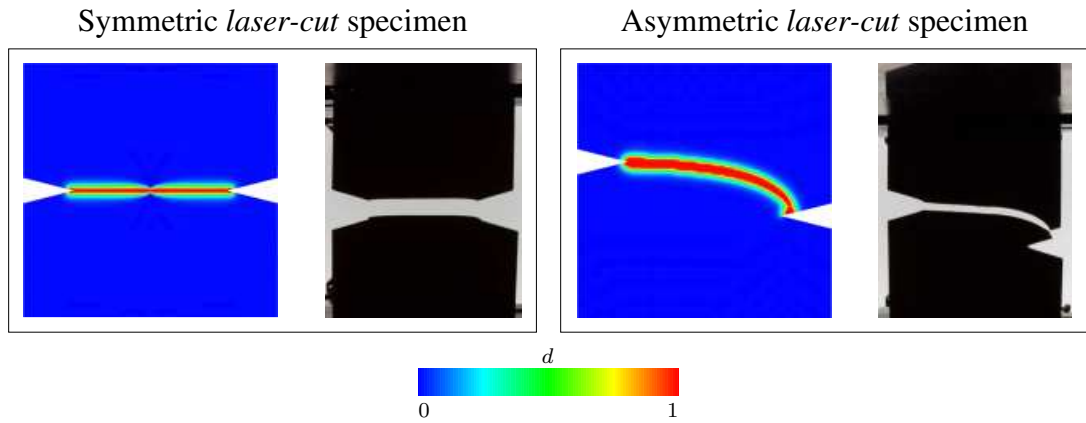
Figure 8.12: Simulation results and post mortem pictures for symmetric (left) and asymmetric (right) specimens.

(ii) different ψ_{cr}^e at around one of the notches In the experiments of laser cut specimens for the asymmetric geometry, we observed a crack forming at one of the notches and follow a catastrophic path without crack initiation at the other notch. This behavior is expected since the critical energies at the notches are higher compared to *die-cut* geometries and also the difference (as crack resistance) between the notches is significantly large. The following simulation is aiming at capturing this behavior. In order to simulate this behavior, a large difference of ψ_{cr}^e is given to the neighborhood of one of the notches as in Fig. 8.9. The simulation results are given in Fig. 8.11 in Lagrangian and Eulerian configurations, clearly showing the crack path starting from one of the notches. Since the critical energy is the same at the other notch with the 1st scenario, we observe the same load-displacement curve as in Fig. 8.8(c). Here, the post-mortem picture of the laser cut specimen is added in Fig. 8.12 for comparison of the crack path.

8.3 Assesment of rate effects

The parameters for ground-state and viscous branches are summarized in Table 8.1 and Table 8.2, respectively. These were obtained in experimental validation chapter (Chapter 7). In this section, we present the simulations for $\dot{u} = 25, 250$ [mm/min] clamp velocities. The load-displacement curves and the associated fits are given in

Table 8.2: Viscous parameters for the unfilled SBR material. These parameters simultaneously fit 4 creep and 4 relaxation set values.

Parameters for the Maxwell branches.				
	χ^v [MPa]	μ^v [MPa]	N^v [-]	$\dot{\gamma}_0/\hat{\tau}_m$ [MPa^{-m}s^{-1}]	m [-]
1st Maxwell branch	462(50)	0.12	90	150	1
2nd Maxwell branch	462(50)	0.05	90	1	3
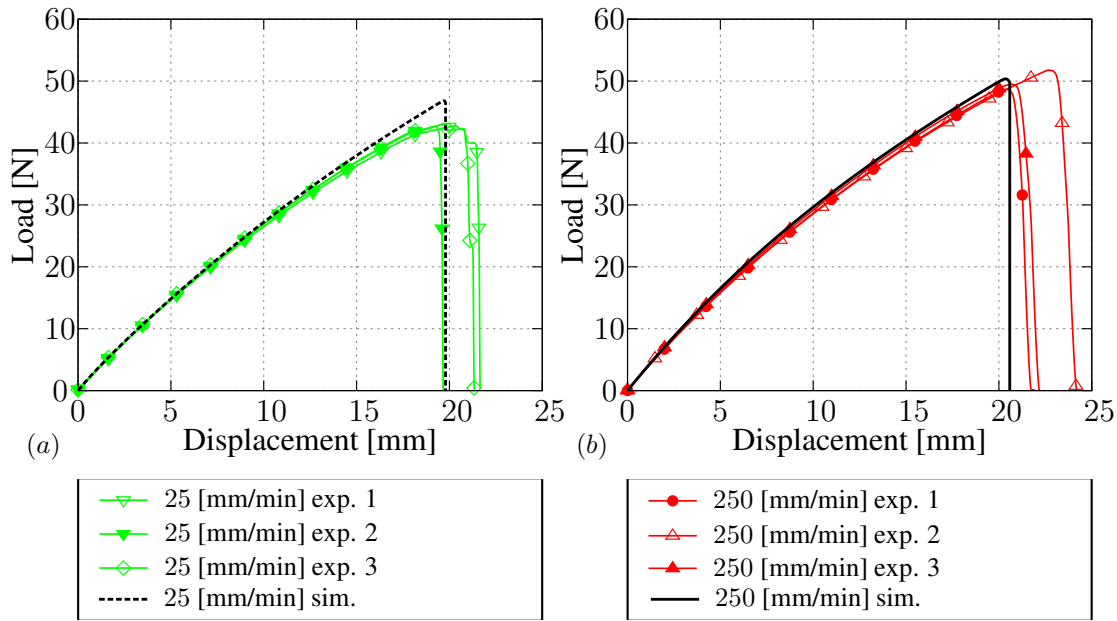
Figure 8.13: Load displacement curves for symmetric 16 [mm] notch length specimen simulation results for (a) $\dot{u} = \{25\}$ [mm/min] and (b) $\dot{u} = \{250\}$ [mm/min] loading rates on *die-cut* geometry's experimental data.

Fig. 8.13. The degradation characteristics is as the previous simulations. These simulations are fitted using the rate experiments of *die-cut* specimens with the final critical entropic value of $\psi_{cr}^e = 0.25$ [MPa/m^3] (cf. value for quasi-static case $\psi_{cr}^e = 0.32$). We note that, v-type double edge notch geometries (vDENT) provide quite the opposite results of double edge straight notch specimens of LOEW ET AL. [95]. vDENT specimens show significant increase in displacement at fracture as the clamp-velocity increases. In a double edge straight notch geometry, the crack tip blunting effects won't be significant to alter the viscous behavior. However, vDENT geometries have

significant blunting before the crack propagation and this effect seems to be pronounced as the clamp-velocity increases and results in a delayed crack formation. As discussed in the experiments chapter, this aspect is proven with experiments on vDENT unfilled NBR specimens. The vDENT geometry seems to be the main reason. Thus, for this very reason the blunting takes effect at material level in our theory, as it is not resolved in geometry for simulations, and forces the theory to utilize negative β_v values in 6.4. Therefore, the value of β_v for these simulations is accepted as -4. As with the other simulations, we set $\kappa = 150\mu$ to prevent volumetric locking for the viscous branches as well. Over the load-displacement curves, we can clearly see the viscous overstress effects where the load at fracture increases as the rate of loading increases.

REMARKS: Experimental measurements of the cricital energy release rate highly depend on the type of the experiments and loading. One of the most accurate critical energy release rate measurements can be achieved with a pure shear type loading on a thin rubber specimen with varying notch lengths. Original investigations by RIVLIN & THOMAS [147] revieled accurate predictions for energy release rate for pure shear geometry, yet, the equation for the energy release rate for the SENT specimens predict erronous results. ROUCOU ET AL. [148, 149] investigated the different loading types and their effects on the resulting critical energy release rate calculations. According to their findings, the SENT specimens with notch lengths smaller than one fifth of the width of the geometry do not allow classical Griffith type analysis, where the unnotched geometry and notched geometries (until fracture) have almost identical load-displacement behavior. The notches larger than the one fifth of the original width of the SENT geometry allow such an analysis but causes non-uniaxial or mixed-loading state around the notch tip due to structural bending, leading to erronous calculations. There appears corrections in ROUCOU ET AL. [149] according to the determination of where the catastrophic failure starts after the initial steady crack growth using the post mortem pictures of the fracture surface of ruptured specimens. After the catastrophic failure, the fractured surfaces are mirror like, while the region where quasi-static crack growth happens exhibit jagged and un-smooth surfaces. However, the exact determination of the point of catastrophic failure is proved difficult ROUCOU ET AL. [149]. Instead, in this study, we utilized v-type notches,

107

which provide less structural bending before the failure, and creates relatively more homogeneous uniaxial tension state around the notch tip, effectively allowing larger notch lengths to determine relatively better critical energy release rates. The double edge arrangement alleviates this problem further due to symmetry, HOCINE ET AL. [143]. However, a tedious Griffith type analysis is not provided, and the physical accuracy of these rates are not assumed. Therefore, with relatively similar mesh sizes for different geometries (as in symmetric and asymmetric tests of the present study), and the length scale parameter of the phase-field model is being fixed, the energy content at fracture is utilized as critical entropic energy in the simulations. On *die-cut* vDENT specimens of the present study, the large notches creates rough propagation patterns as commented out in ROUCOU ET AL. [148]. Interestingly, the laser cut specimens showed brittle and sudden failure even with the same large notch lengths with the *die-cut* specimens. The resulted simulations with the same mesh coarseness around the propagation path, proved the theory viable in vDENT simulations. Nonetheless, a more accurate critical energy release rate calculation is still needed, and calibration of the length scale parameter has to be pursued with a DIC system [95]. Another aspect of the SENT, DENT, vDENT, and pure shear type fructure experiments is the stochasticity of the initial steady crack growth phase, which indicate the coupled nature of loss of incompressibility and material's inhomogenities. This is important for a fatigue crack growth study using phase-field approach. The cyclic loading around critical levels of a specimen does not always initiate catastrophic failure, and progressive crack growth is almost always in the beginning steady crack growth regime for each cycle. Modeling of the behavior in this regime is half-way treated in the present study by utilizing different degradation functions for volumetric and entropic degradations, and stochasticity is left for a future study. Finally, the captured behavior of *laser-cut* specimens are shown side by side with post mortems of experiments and simulations in Figure 8.12.

CHAPTER 9

CONCLUSION

In this work, we proposed several extensions to the phase-field approach based on the novel compressible extended eight-chain model. The extended eight-chain model provides distinct terms related to I_1, I_2, I_3. The non-dilatational response is decoupled and consists of free-chain and constraint responses. It is called the entropic part throughout the thesis, since it encompasses all entropic behaviors of rubber-like materials. The advantage of distinct terms of the extended eight-chain model allows separate degradation of each term. The degradation functions can be produced with the novel tunable Hermitian polynomials. The tunable nature of the Hermitian polynomials allow adjustment of the degradation of each term separately. This unique feature is then showed to capture an experimental behavior, where at the crack front, cavity like formations occur before the propagation. This phenomenon weakens the crack front and makes the rubber transition from quasi-incompressible hyperelastic behavior to a porous compressible solid state prior to macro-crack formation. Utilizing two distinct degradation functions for the volumetric and the entropic parts, the proposed generalized phase-field approach is shown to allow such transition and the degradation of the Poisson's ratio is captured. The forms of the history fields for separate terms of the extended eight-chain model allow definition of multi-axial failure surface for rubber-like materials. This approach is shown to agree with the experimental results on the Π_0-plane, where no hydrostatic deformation takes place. Furthermore, it is shown that, the proposed surface is capable of providing 3D failure bounds, also capturing the point of cavitation on the hydrostatic axis. Its capability of simultaneously fitting both the failure surfaces for entropic and volumetric failure modes is shown by comparing to data from the literature. This whole approach provides a unique multi-axial failure surface for rubber-like materials, where only the

phenomenological equivalent-strain based approaches has provided such accuracy so far. The separate I_2 term, which is related to the constraint part, is elegantly represented with an additional parameter α_c, provides tuning the failure surface for the biaxial loads. This parameter is shown to produce counterparts of the well-known stress-based failure criteria, such as von-Mises, Mariotte, and Ivlev. This unique feature comes directly from the micro-mechanical definition of I_2 term. With the proposed generalized phase-field approach, both the crack initiation in a multi-axial deformation state and crack propagation in the sense that a rubber-like material's incompressibility also degrades along the crack path can be taken into account in a simulation. Next, a nonlinearly viscous theory is coupled with the generalized phase-field approach in an ad-hoc manner, where good agreement on high strian rate fracture experiments also observed. The general tendancy of the increased stresses at fracture, and decreased strains observed as in literature. A parameter β_v is introduced in the failure criterion definition to adjust the contribution of the viscous branch's stored energies into the failure criterion. In this work, we conducted several in-house experiments on unfilled SBR material for validation. These encompasses uniaxial, equibiaxial, volumetric compression, creep, and relaxation tests for the mechanical characterization and several symmetric and asymmetric custom fracture geometries for validation. The custom vDENT geometries for the fracture experiments are obtained by laser and die cutting as separate batches. It is evident from the experiments that, the crack initiation in the *laser-cut* specimens is much more difficult than the *die-cut* specimens. Also in the symmetric experiments three different notch lengths are considered. It is shown that, by fitting the critical entropic energy to one of the notch lengths captures the behavior on the rest of the notch lengths, also on the asymmetric geometry. From the experiments, it is obvious that, the fracture is a stochastic process. The crack paths are jagged and diverges from the expected straigth-path for the *die-cut* symmetric experiments. This suggest, even for an unfilled rubber, the production method and the additives cause inhomogenities on the critical energies with the geometry. A stochastic distribution of the entropic critical energies within the geometry would allow capturing this behavior and it is extremely important for fatigue crack growth studies. This theory allows such an extension, however it is not pursued in this thesis.

REFERENCES

[1] L. R. G. Treloar, "The elasticity of a network of long-chain molecules-II," *Transactions of the Faraday Society*, vol. 39, pp. 241–246, 1943. Publisher: Royal Society of Chemistry.

[2] M. Mooney, "A theory of large elastic deformation," *Journal of Applied Physics*, vol. 11, pp. 582–592, 1940.

[3] V. Biderman, "Calculation of rubber parts," *Rascheti na prochnost*, vol. 40, 1958.

[4] O. H. Yeoh, "Characterization of elastic properties of carbon-black-filled rubber vulcanizates," *Rubber Chemistry and Technology*, vol. 63, no. 5, pp. 792–805, 1990.

[5] A. N. Gent and A. Thomas, "Forms for the stored (strain) energy function for vulcanized rubber," *Journal of Polymer Science*, vol. 28, no. 118, pp. 625–628, 1958. Publisher: Wiley Online Library.

[6] S. R. Swanson, "A constitutive model for high elongation elastic materials," *Journal of engineering materials and technology*, vol. 107, no. 2, pp. 110–114, 1985. Publisher: American Society of Mechanical Engineers.

[7] H.-G. Kilian, H. F. Enderle, and K. Unseld, "The use of the van der Waals model to elucidate universal aspects of structure-property relationships in simply extended dry and swollen rubbers," *Colloid and Polymer Science*, vol. 264, no. 10, pp. 866–876, 1986. Publisher: Springer.

[8] A. N. Gent, "A new constitutive relation for rubber," *Rubber Chemistry and Technology*, vol. 69, pp. 59–61, 1996.

[9] O. H. Yeoh and P. D. Fleming, "A new attempt to reconcile the statistical and phenomenological theories of rubber elasticity," *Journal of Polymer Science*

Part B: Polymer Physics, vol. 35, no. 12, pp. 1919–1931, 1997. Publisher: Wiley Online Library.

[10] L. J. Hart-Smith, "Elasticity parameters for finite deformations of rubber-like materials," *Zeitschrift für angewandte Mathematik und Physik ZAMP*, vol. 17, no. 5, pp. 608–626, 1966. Publisher: Springer.

[11] J. Lambert-Diani and C. Rey, "New phenomenological behavior laws for rubbers and thermoplastic elastomers," *European Journal of Mechanics-A/Solids*, vol. 18, no. 6, pp. 1027–1043, 1999. Publisher: Elsevier.

[12] E. Pucci and G. Saccomandi, "A note on the Gent model for rubber-like materials," *Rubber chemistry and technology*, vol. 75, no. 5, pp. 839–852, 2002.

[13] O. Lopez-Pamies, "A new I1-based hyperelastic model for rubber elastic materials," *Comptes Rendus Mecanique*, vol. 338, no. 1, pp. 3–11, 2010. Publisher: Elsevier.

[14] H. Khajehsaeid, J. Arghavani, and R. Naghdabadi, "A hyperelastic constitutive model for rubber-like materials," *European Journal of Mechanics-A/Solids*, vol. 38, pp. 144–151, 2013. Publisher: Elsevier.

[15] K. C. Valanis and R. F. Landel, "The strain-energy function of a hyperelastic material in terms of the extension ratios," *Journal of Applied Physics*, vol. 38, no. 7, pp. 2997–3002, 1967. Publisher: AIP.

[16] R. C. Ball, M. Doi, S. F. Edwards, and M. Warner, "Elasticity of entangled networks," *Polymer*, vol. 22, no. 8, pp. 1010–1018, 1981. Publisher: Elsevier.

[17] R. Ogden, "Large deformation isotropic elastictiy: on the correlation of theory and experiment for incompressible rubberlike solids," *Proceedings of the Royal Society London A*, vol. 326, pp. 565–584, 1972.

[18] M. H. B. M. Shariff, "Strain energy function for filled and unfilled rubberlike material," *Rubber chemistry and technology*, vol. 73, no. 1, pp. 1–18, 2000.

[19] M. M. Attard and G. W. Hunt, "Hyperelastic constitutive modeling under finite strain," *International Journal of Solids and Structures*, vol. 41, no. 18-19, pp. 5327–5350, 2004. Publisher: Elsevier.

[20] H. Bechir, L. Chevalier, M. Chaouche, and K. Boufala, "Hyperelastic constitutive model for rubber-like materials based on the first Seth strain measures invariant," *European Journal of Mechanics-A/Solids*, vol. 25, no. 1, pp. 110–124, 2006. Publisher: Elsevier.

[21] A. G. Korba and M. E. Barkey, "New model for hyper-elastic materials behavior with an application on natural rubber," in *ASME 2017 12th international manufacturing science and engineering conference collocated with the JSME/ASME 2017 6th international conference on materials and processing*, pp. V002T03A020–V002T03A020, 2017. tex.organization: American Society of Mechanical Engineers.

[22] G. Heinrich and M. Kaliske, "Theoretical and numerical formulation of a molecular based constitutive Tube–Model of rubber elasticity," *Computational and Theoretical Polymer Science*, vol. 7, pp. 227–241, 1997.

[23] M. Kaliske and G. Heinrich, "An extended Tube–Model for rubber elasticity: Statistical–Mechanical theory and finite element implementation," *Rubber Chemistry and Technology*, vol. 72, pp. 602–632, 1999.

[24] W. Kuhn, "Über die gestalt fadenförmiger moleküle in lösungen," *Kolloid-Zeitschrift*, vol. 68, pp. 2–15, 1934.

[25] W. Kuhn, "Beziehungen zwischen molekülgröße, statistischer molekülgestalt und elastischen eigenschaften hochpolymerer stoffe," *Kolloid-Zeitschrift*, vol. 76, pp. 258–271, 1936.

[26] F. T. Wall, "Statistical thermodynamics of rubber," *The Journal of Chemical Physics*, vol. 10, p. 132, 1942. Publisher: American Institute of Physics.

[27] L. R. G. Treloar, *The physics of rubber elasticity*. Clarendon Press, Oxford, 3rd ed., 1975.

[28] W. Kuhn and F. Grün, "Beziehungen zwischen elastischen konstanten und dehnungsdoppelbrechung hochelastischer stoffe," *Kolloid-Zeitschrift*, vol. 101, pp. 248–271, 1942.

[29] M. C. Wang and E. Guth, "Statistical theory of networks of Non–Gaussian flexible chains," *The Journal of Chemical Physics*, vol. 20, pp. 1144–1157, 1952.

[30] P. J. Flory and J. J. Rehner, "Statistical mechanics of Cross–Linked polymer networks: I. Rubberlike elasticity," *The Journal of Chemical Physics*, vol. 11, pp. 512–520, 1943.

[31] L. R. G. Treloar and G. Riding, "A Non–Gaussian theory of rubber in biaxial strain. I. Mechanical properties," *Proceedings of the Royal Society London A*, vol. 369, pp. 261–280, 1979.

[32] E. M. Arruda and M. C. Boyce, "A Three–Dimensional constitutive model for the large stretch behavior of rubber elastic materials," *Journal of the Mechanics and Physics of Solids*, vol. 41, pp. 389–412, 1993.

[33] C. Miehe, S. Göktepe, and F. Lulei, "A micro-macro approach to rubber-like materials. Part I: The non-affine micro-sphere model of rubber elasticity.," *Journal of the Mechanics and Physics of Solids*, vol. 52, pp. 2617–2660, 2004.

[34] V. N. Khiêm and M. Itskov, "Analytical network-averaging of the tube model:: Rubber elasticity," *Journal of the Mechanics and Physics of Solids*, vol. 95, pp. 254–269, 2016. Publisher: Elsevier.

[35] B. Erman and P. J. Flory, "Theory of Elasticity of Polymer Networks. II. The effect of geometric constraints on junctions," *The Journal of Chemical Physics*, vol. 68, pp. 5363–5369, 1978.

[36] P. J. Flory and B. Erman, "Theory of elasticity of polymer networks. 3," *Macromolecules*, vol. 15, pp. 800–806, 1982.

[37] H. Dal, K. Açıkgöz, and Y. Badienia, "On the Performance of Isotropic Hyperelastic Constitutive Models for Rubber-Like Materials: A State of the Art Review," *Applied Mechanics Reviews*, vol. 73, no. 2, p. 020802, 2021.

[38] G. Marckmann and E. Verron, "Comparison of hyperelastic models for rubberlike materials," *Rubber Chemistry and Technology*, vol. 79, pp. 835–858, 2006.

[39] P. Steinmann, M. Hossain, and G. Possart, "Hyperelastic models for rubber-like materials: consistent tangent operators and suitability for Treloar's data," *Archive of Applied Mechanics*, vol. 82, no. 9, pp. 1183–1217, 2012. Publisher: Springer.

[40] M. C. Boyce and E. M. Arruda, "Constitutive models of rubber elasticity: A review," *Rubber Chemistry and Technology*, vol. 73, pp. 504–523, 2000.

[41] R. S. Rivlin and D. W. Saunders, "Large elastic deformations of isotropic materials VII. Experiments on the deformation of rubber," *Philosophical Transactions of the Royal Society of London. Series A, Mathematical and Physical Sciences*, vol. 243, no. 865, pp. 251–288, 1951.

[42] J. D. Davidson and N. C. Goulbourne, "A nonaffine network model for elastomers undergoing finite deformations," *Journal of the Mechanics and Physics of Solids*, vol. 61, pp. 1784–1797, 2013.

[43] H. Dal, O. Gültekin, and K. Açıkgöz, "An extended eight-chain model for hyperelastic and finite viscoelastic response of rubberlike materials: Theory, experiments and numerical aspects," *Journal of the Mechanics and Physics of Solids*, vol. 145, p. 104159, 2020.

[44] J. Ferry, *Viscoelastic Properties of Polymers*. Wiley, 1980.

[45] A. Lion, "A constitutive model for carbon black filled rubber: Experimental investigations and mathematical representation," *Continuum Mechanics and Thermodynamics*, vol. 8, pp. 153–169, June 1996.

[46] C. Miehe and J. Keck, "Superimposed finite elastic–viscoelastic–plastoelastic stress response with damage in filled rubbery polymers. Experiments, modelling and algorithmic implementation," *Journal of the Mechanics and Physics of Solids*, vol. 48, pp. 323–365, Feb. 2000.

[47] C. Miehe and S. Göktepe, "A Micro–Macro approach to Rubber–Like materials. Part II: The Micro–Sphere model of finite rubber viscoelasticity," *Journal of the Mechanics and Physics of Solids*, vol. 53, pp. 2231–2258, 2005.

[48] R. Christensen, *Theory of viscoelasticity: an introduction*. Elsevier, 2012.

[49] N. Phan-Thien and N. Mai-Duy, *Understanding viscoelasticity: an introduction to rheology.* Springer, 2013.

[50] B. Coleman and W. Noll, "Foundations of linear viscoelasticity," *Reviews of Modern Physics*, vol. 33, pp. 239–249, 1961.

[51] B. D. Coleman, "On thermodynamics, strain impulses, and viscoelasticity," *Archive for Rational Mechanics and Analysis*, vol. 17, no. 3, pp. 230–254, 1964. Publisher: Springer.

[52] C. Truesdell and W. Noll, "The Non–linear field theories of mechanics," in *Encyclopedia of physics III/3* (S. Flügge, ed.), vol. III/3, Springer–Verlag, Berlin, 1965.

[53] J. Simo, "On a fully three-dimensional finite-strain viscoelastic damage model: Formulation and computational aspects," *Computer Methods in Applied Mechanics and Engineering*, vol. 60, pp. 153–173, Feb. 1987.

[54] G. A. Holzapfel and J. C. Simo, "A new viscoelastic constitutive model for continuous media at finite thermomechanical changes," *International Journal of Solids and Structures*, vol. 33, pp. 3019–3034, Aug. 1996.

[55] M. Kaliske and H. Rothert, "Formulation and implementation of three-dimensional viscoelasticity at small and finite strains," *Computational Mechanics*, vol. 19, pp. 228–239, Feb. 1997.

[56] P. Haupt and A. Lion, "On finite linear viscoelasticity of incompressible isotropic materials," *Acta Mechanica*, vol. 159, pp. 87–124, Mar. 2002.

[57] J. Lubliner, "A model of rubber viscoelasticity," *Mechanics Research Communications*, vol. 12, pp. 93–99, Mar. 1985.

[58] A. Lion, "On the large deformation behaviour of reinforced rubber at different temperatures," *Journal of the Mechanics and Physics of Solids*, vol. 45, pp. 1805–1834, Nov. 1997.

[59] J. S. Bergström and M. C. Boyce, "Constitutive modeling of the large strain Time–Dependent behavior of elastomers," *Journal of the Mechanics and Physics of Solids*, vol. 46, pp. 931–954, 1998.

[60] S. Reese and S. Govindjee, "A theory of finite viscoelasticity and numerical aspects," *International journal of solids and structures*, vol. 35, no. 26-27, pp. 3455–3482, 1998. Publisher: Elsevier.

[61] N. Koprowski-Theiss, M. Johlitz, and S. Diebels, "Characterizing the time dependence of filled EPDM," *Rubber Chemistry and Technology*, vol. 84, no. 2, pp. 147–165, 2011.

[62] H. Dal and M. Kaliske, "A micro-continuum-mechanical material model for failure of rubber-like materials: Application to ageing-induced fracturing," *Journal of the Mechanics and Physics of Solids*, vol. 57, no. 8, pp. 1340–1356, 2009.

[63] J. Simo and C. Miehe, "Associative coupled thermoplasticity at finite strains: Formulation, numerical analysis and implementation," *Computer Methods in Applied Mechanics and Engineering*, vol. 98, pp. 41–104, 1992.

[64] J. Simo, "Algorithms for static and dynamic multiplicative plasticity that preserve the classical return mapping schemes of the infinitesimal theory," *Computer Methods in Applied Mechanics and Engineering*, vol. 99, no. 1, pp. 61–112, 1992.

[65] G. Weber and L. Anand, "Finite deformation constitutive equations and a time integration procedure for isotropic, hyperelastic-viscoplastic solids," *Computer Methods in Applied Mechanics and Engineering*, vol. 79, no. 2, pp. 173–202, 1990. Publisher: Elsevier.

[66] A. Cuitino and M. Ortiz, "A material-independent method for extending stress update algorithms from small-strain plasticity to finite plasticity with multiplicative kinematics," *Engineering computations*, 1992. Publisher: MCB UP Ltd.

[67] B. Eidel, F. Stumpf, and J. Schröder, "Finite strain viscoelasticity: how to consistently couple discretizations in time and space on quadrature-point level for full order p\ge 2 and a considerable speed-up," *Computational Mechanics*, vol. 52, no. 3, pp. 463–483, 2013. Publisher: Springer.

[68] H. Dal, C. Zopf, and M. Kaliske, "Micro-sphere based viscoplastic constitutive model for uncured green rubber," *International Journal of Solids and Structures*, vol. 132-133, pp. 201–217, 2018.

[69] M. S. Green and A. V. Tobolsky, "A new approach to the theory of relaxing polymeric media," *The Journal of chemical physics*, vol. 14, no. 2, pp. 80–92, 1946. Publisher: American Institute of Physics.

[70] A. S. Lodge, "A network theory of flow birefringence and stress in concentrated polymer solutions," *Trans. Faraday Soc.*, vol. 52, no. 0, pp. 120–130, 1956. Publisher: The Royal Society of Chemistry.

[71] N. Phan–Thien, "A nonlinear network viscoelastic model," *Journal of Rheology*, vol. 22, pp. 259–283, 1978.

[72] F. Tanaka and S. F. Edwards, "Viscoelastic properties of physically crosslinked networks part 1. Non–linear stationary viscoelasticity," *Journal of Non–Newtonian Fluid Mechanics*, vol. 43, pp. 247–271, 1992.

[73] F. Tanaka and S. F. Edwards, "Viscoelastic properties of physically crosslinked networks part 2. Dynamic mechanical moduli," *Journal of Non–Newtonian Fluid Mechanics*, vol. 43, pp. 289–309, 1992.

[74] C. Linder, M. Tkachuk, and C. Miehe, "A micromechanically motivated diffusion-based transient network model and its incorporation into finite rubber viscoelasticity," *Journal of the Mechanics and Physics of Solids*, vol. 59, no. 10, pp. 2134–2156, 2011. Publisher: Elsevier.

[75] P. G. de Gennes, "Reptation of a Polymer Chain in the Presence of Fixed Obstacles," *J. Chem. Phys.*, vol. 55, pp. 572–579, July 1971. Publisher: American Institute of Physics.

[76] M. Doi and S. F. Edwards, *The theory of polymer dynamics*. Clarendon Press, Oxford, 1986.

[77] R. Raghunath, D. Juhre, and M. Klüppel, "A physically motivated model for filled elastomers including strain rate and amplitude dependency in finite viscoelasticity," *International Journal of Plasticity*, vol. 78, pp. 223–241, 2016. Publisher: Elsevier.

[78] A. A. Griffith, "The phenomena of rupture and flow in solids," *Philosophical Transactions of the Royal Society London A*, vol. 221, pp. 163–198, 1920. tex.pdf: griffith21.pdf.

[79] G. Irwin, "Elasticity and plasticity," *Encyclopaedia of physics*, vol. 6, pp. 551–590, 1958. Publisher: Springer Berlin.

[80] H. Liebowitz and G. Sih, "Mathematical theories of brittle fracture.," 1968.

[81] C. Miehe, M. Hofacker, and F. Welschinger, "A phase field model for rate-independent crack propagation: Robust algorithmic implementation based on operator splits," *Computer Methods in Applied Mechanics and Engineering*, vol. 199, no. 45, pp. 2765–2778, 2010.

[82] T. L. Anderson, *Fracture mechanics: fundamentals and applications*. CRC press, 2017.

[83] G. A. Francfort and J. J. Marigo, "Revisiting brittle fracture as an energy minimization problem," *Journal of the Mechanics and Physics of Solids*, vol. 46, pp. 1319–1342, 1998. tex.pdf: francfort+marigo98.pdf.

[84] D. Mumford and J. Shah, "Optimal approximations by piecewise smooth functions and associated variational problems," *Communications on Pure and Applied Mathematics*, vol. 42, pp. 577–685, 1989. tex.pdf: mumford+shah89.pdf.

[85] B. Bourdin, G. Francfort, and J.-J. Marigo, "Numerical experiments in revisited brittle fracture," *Journal of the Mechanics and Physics of Solids*, vol. 48, no. 4, pp. 797–826, 2000.

[86] B. Bourdin, G. A. Francfort, and J.-J. Marigo, "The Variational Approach to Fracture," *Journal of Elasticity*, vol. 91, pp. 5–148, Apr. 2008.

[87] C. Miehe, M. Hofacker, and F. Welschinger, "A phase field model for rate-independent crack propagation: Robust algorithmic implementation based on operator splits," *Computer Methods in Applied Mechanics and Engineering*, vol. 199, no. 45, pp. 2765–2778, 2010.

[88] G. Capriz, *Continua with microstructure*, vol. 35. Springer Science & Business Media, 2013.

[89] L. Schänzel, H. Dal, and C. Miehe, "On micromechanically-based approaches to failure in polymers," *PAMM*, vol. 13, no. 1, pp. 557–560, 2013.

[90] L. Schanzel, H. Dal, and C. Miehe, "Phase field modeling of fracture in rubbery polymers," *Constitutive Models for Rubber VIII*, pp. 335–341, 2013. Publisher: CRC Press.

[91] "Phase field modeling of fracture in rubbery polymers. Part I: Finite elasticity coupled with brittle failure," *Journal of the Mechanics and Physics of Solids*, vol. 65, pp. 93–113, 2014.

[92] L.-M. Schänzel, *Phase field modeling of fracture in rubbery and glassy polymers at finite thermo-viscoelastic deformations*. PhD thesis, University of Stuttgart, 2015.

[93] B. Yin, C. Steinke, and M. Kaliske, "Formulation and implementation of strain rate-dependent fracture toughness in context of the phase-field method," *International Journal for Numerical Methods in Engineering*, vol. 121, no. 2, pp. 233–255, 2020. tex.eprint: https://onlinelibrary.wiley.com/doi/pdf/10.1002/nme.6207.

[94] K. Özenç, *Approaches to model failure of structures by configurational mechanics: Theory and numerics*. PhD Dissertation, Techn. Univ., Inst. für Statik und Dynamik der Tragwerke, 2016.

[95] P. J. Loew, B. Peters, and L. A. Beex, "Rate-dependent phase-field damage modeling of rubber and its experimental parameter identification," *Journal of the Mechanics and Physics of Solids*, vol. 127, pp. 266–294, 2019.

[96] C. Miehe and L.-M. Schänzel, "Phase field modeling of fracture in rubbery polymers. Part I: Finite elasticity coupled with brittle failure," *Journal of the Mechanics and Physics of Solids*, vol. 65, pp. 93–113, 2014.

[97] G. A. Holzapfel, "On large strain viscoelasticity: Continuum formulation and finite element applications to elastomeric structures," *International Journal for Numerical Methods in Engineering*, vol. 39, no. 22, pp. 3903–3926, 1996.

[98] B. Yin and M. Kaliske, "Fracture simulation of viscoelastic polymers by the phase-field method," *Computational Mechanics*, vol. 65, pp. 293–309, Feb. 2020.

[99] R. Shen, H. Waisman, and L. Guo, "Fracture of viscoelastic solids modeled with a modified phase field method," *Computer Methods in Applied Mechanics and Engineering*, vol. 346, pp. 862–890, 2019.

[100] A. Gent and P. Lindley, "Internal rupture of bonded rubber cylinders in tension," *Proceedings of the Royal Society of London. Series A. Mathematical and Physical Sciences*, vol. 249, no. 1257, pp. 195–205, 1959. Publisher: The Royal Society London.

[101] A. Kumar and O. Lopez-Pamies, "The poker-chip experiments of Gent and Lindley (1959) explained," *Journal of the Mechanics and Physics of Solids*, vol. 150, p. 104359, 2021.

[102] J. M. Ball, "Discontinuous equilibrium solutions and cavitation in nonlinear elasticity," *Philosophical Transactions of the Royal Society of London. Series A, Mathematical and Physical Sciences*, vol. 306, no. 1496, pp. 557–611, 1982. Publisher: The Royal Society London.

[103] J. Li, D. Mayau, and F. Song, "A constitutive model for cavitation and cavity growth in rubber-like materials under arbitrary tri-axial loading," *International journal of solids and structures*, vol. 44, no. 18-19, pp. 6080–6100, 2007. Publisher: Elsevier.

[104] J. Li, D. Mayau, and V. Lagarrigue, "A constitutive model dealing with damage due to cavity growth and the Mullins effect in rubber-like materials under tri-axial loading," *Journal of the Mechanics and Physics of Solids*, vol. 56, no. 3, pp. 953–973, 2008. Publisher: Elsevier.

[105] V. A. Kolupaev, "Criteria of equivalent stress concept," in *Equivalent stress concept for limit state analysis*, pp. 13–66, Cham: Springer International Publishing, 2018.

[106] O. Gültekin, H. Dal, and G. A. Holzapfel, "Numerical aspects of anisotropic failure in soft biological tissues favor energy-based criteria: A rate-dependent

anisotropic crack phase-field model," *Computer Methods in Applied Mechanics and Engineering*, vol. 331, pp. 23–52, 2018.

[107] P. Rosendahl, M. Drass, J. Felger, J. Schneider, and W. Becker, "Equivalent strain failure criterion for multiaxially loaded incompressible hyperelastic elastomers," *International Journal of Solids and Structures*, vol. 166, pp. 32–46, 2019.

[108] K. Y. Volokh, "Review of the energy limiters approach to modeling failure of rubber," *Rubber Chemistry and Technology*, vol. 86, pp. 470–487, Sept. 2013.

[109] J.-B. Le Cam, B. Huneau, E. Verron, and L. Gornet, "Mechanism of Fatigue Crack Growth in Carbon Black Filled Natural Rubber," *Macromolecules*, vol. 37, pp. 5011–5017, June 2004. Publisher: American Chemical Society.

[110] I. Ang, N. Bouklas, and B. Li, "Stabilized formulation for phase-field fracture in nearly incompressible hyperelasticity," *International Journal for Numerical Methods in Engineering*, vol. 123, no. 19, pp. 4655–4673, 2022.

[111] B. Li and N. Bouklas, "A variational phase-field model for brittle fracture in polydisperse elastomer networks," *International Journal of Solids and Structures*, vol. 182-183, pp. 193–204, 2020.

[112] J. E. Marsden and T. J. R. Hughes, *Mathematical foundations of elasticity*. Prentice-Hall, Englewood Cliffs, New Jersey, 1983.

[113] L. E. Malvern, *Introduction to the mechanics of a continuous medium*. Prentice Hall, 1969. Type: Book.

[114] P. Haupt, "On the mathematical modelling of material behavior in continuum mechanics," *Acta Mechanica*, vol. 100, pp. 129–154, Sept. 1993.

[115] G. A. Holzapfel, "Nonlinear solid mechanics: a continuum approach for engineering science," *Meccanica*, vol. 37, no. 4, pp. 489–490, 2002. Publisher: Kluwer Academic Publishers.

[116] B. D. Coleman and W. Noll, "The thermodynamics of elastic materials with heat conduction and viscosity," *Archive for Rational Mechanics and Analysis*, vol. 13, pp. 167–178, Dec. 1963.

[117] E. Kröner, "Allgemeine Kontinuumstheorie der Versetzungen und Eigenspannungen," *Archive for Rational Mechanics and Analysis*, vol. 4, pp. 273–334, Jan. 1959.

[118] E. H. Lee, "Elastic-Plastic Deformation at Finite Strains," *Journal of Applied Mechanics*, vol. 36, pp. 1–6, Mar. 1969.

[119] C. Kadapa and M. Hossain, "A linearized consistent mixed displacement-pressure formulation for hyperelasticity," *Mechanics of Advanced Materials and Structures*, pp. 1–18, 2020. Publisher: Taylor & Francis.

[120] H. Dal, *Approaches to the modeling of inelasticity and failure of rubberlike materials*. PhD Dissertation, Technische Universit\"at Dresden, 2011.

[121] A. Cohen, "A padé approximant to the inverse langevin function," *Rheological Acta*, vol. 30, pp. 270–273, 1991.

[122] C. Miehe, F. Welschinger, and M. Hofacker, "Thermodynamically consistent phase-field models of fracture: Variational principles and multi-field FE implementations," *International Journal for Numerical Methods in Engineering*, vol. 83, pp. 1273–1311, 2010.

[123] C. Kuhn, A. Schlüter, and R. Müller, "On degradation functions in phase field fracture models," *Computational Materials Science*, vol. 108, pp. 374–384, 2015.

[124] M. J. Borden, T. J. Hughes, C. M. Landis, A. Anvari, and I. J. Lee, "A phase-field formulation for fracture in ductile materials: Finite deformation balance law derivation, plastic degradation, and stress triaxiality effects," *Computer Methods in Applied Mechanics and Engineering*, vol. 312, pp. 130–166, 2016.

[125] O. Gültekin, H. Dal, and G. A. Holzapfel, "Numerical aspects of anisotropic failure in soft biological tissues favor energy-based criteria: A rate-dependent anisotropic crack phase-field model," *Computer Methods in Applied Mechanics and Engineering*, vol. 331, pp. 23–52, 2018.

[126] O. Gültekin, H. Dal, and G. A. Holzapfel, "A phase-field approach to model fracture of arterial walls: Theory and finite element analysis," *Computer Methods in Applied Mechanics and Engineering*, vol. 312, pp. 542–566, 2016.

[127] A. Hamdi and H. Mahjoubi, "Design criterion for rubbery parts under biaxial loading," *Theoretical and Applied Fracture Mechanics*, vol. 78, pp. 51–55, 2015.

[128] Sueo Kawabata, "Fracture and mechanical behavior of rubber-like polymers under finite deformation in biaxial stress field," *Journal of Macromolecular Science, Part B*, vol. 8, no. 3-4, pp. 605–630, 1973. Publisher: Taylor & Francis.

[129] A. Hamdi, M. Abdelaziz, N. Hocine, P. Heuillet, and N. Benseddiq, "A fracture criterion of rubber-like materials under plane stress conditions," *Polymer Testing*, vol. 25, pp. 994–1005, 2006.

[130] A. Hamdi, M. N. Abdelaziz, N. A. Hocine, and P. Heuillet, "Fracture criteria of rubber-like materials under plane stress conditions.," in *Fracture of nano and engineering materials and structures - proceedings of the 16th european conference of fracture.*, 2006.

[131] R. G. Cuntze, "The failure mode concept - a new comprehensive 3D-Strength analysis concept for any brittle and ductile behaving material," *Proceedings of a European Conference held at Braunschweig*, vol. 428, pp. 269–287, 1999. ISBN: 9290927127.

[132] G. Del Piero, "A Variational Approach to Fracture and Other Inelastic Phenomena," *Journal of Elasticity*, vol. 112, pp. 3–77, June 2013.

[133] F. Freddi and G. Royer-Carfagni, "Regularized variational theories of fracture: A unified approach," *Journal of the Mechanics and Physics of Solids*, vol. 58, no. 8, pp. 1154–1174, 2010.

[134] T. T. Nguyen, J. Yvonnet, M. Bornert, C. Chateau, K. Sab, R. Romani, and R. Le Roy, "On the choice of parameters in the phase field method for simulating crack initiation with experimental validation," *International Journal of Fracture*, vol. 197, pp. 213–226, Feb. 2016.

[135] E. Tanné, T. Li, B. Bourdin, J.-J. Marigo, and C. Maurini, "Crack nucleation in variational phase-field models of brittle fracture," *Journal of the Mechanics and Physics of Solids*, vol. 110, pp. 80–99, 2018.

[136] M. Heydari-Meybodi, M. R. Ayatollahi, M. Dehghany, and F. Berto, "Fracture analysis of V-notched rubbers: An experimental and theoretical study," *Fatigue & Fracture of Engineering Materials & Structures*, vol. 42, no. 3, pp. 732–742, 2019. tex.eprint: https://onlinelibrary.wiley.com/doi/pdf/10.1111/ffe.12947.

[137] F. Dammaß, M. Ambati, and M. Kästner, "A unified phase-field model of fracture in viscoelastic materials," *Continuum Mechanics and Thermodynamics*, vol. 33, pp. 1907–1929, July 2021.

[138] F. Dammaß, K. A. Kalina, M. Ambati, and M. Kästner, "Phase-field modelling and analysis of rate-dependent fracture phenomena at finite deformation," *arXiv preprint arXiv:2206.03460*, 2022.

[139] J. Wu, C. McAuliffe, H. Waisman, and G. Deodatis, "Stochastic analysis of polymer composites rupture at large deformations modeled by a phase field method," *Computer Methods in Applied Mechanics and Engineering*, vol. 312, pp. 596–634, 2016.

[140] J. Diani, B. Fayolle, and P. Gilormini, "A review on the Mullins effect," *European Polymer Journal*, vol. 45, no. 3, pp. 601–612, 2009. Publisher: Elsevier.

[141] B. Huneau, "Strain-induced crystallization of natural rubber: a review of X-ray diffraction investigations," *Rubber chemistry and technology*, vol. 84, no. 3, pp. 425–452, 2011.

[142] "Rubber, vulcanized or thermoplastic – Determination of tensile stress-strain properties," standard – international organization for standardization,, Geneva, CH, 2017. tex.howpublished: axelproducts.com tex.key: ISO-37:2017(E).

[143] N. A. Hocine, M. N. Abdelaziz, and A. Imad, "Fracture problems of rubbers: J-integral estimation based upon eta factors and an investigation on the strain energy density distribution as a local criterion," *International Journal of Fracture*, vol. 117, pp. 1–23, 2002.

[144] R. L. Taylor, "FEAP - Finite Element Analysis Program," 2014.

[145] H. Dal, "A quasi-incompressible and quasi-inextensible element formulation for transversely isotropic materials," *International Journal for Numerical*

Methods in Engineering, vol. 117, no. 1, pp. 118–140, 2019. Publisher: Wiley Online Library.

[146] M. Smith, *ABAQUS/Standard user's manual, version 6.9.* United States: Dassault Systèmes Simulia Corp, 2009.

[147] R. Rivlin and A. Thomas, "Rupture of rubber. I. Characteristic energy for tearing," *Journal of Polymer Science*, vol. X, No. 3, pp. 291–318, 1953.

[148] D. Roucou, J. Diani, M. Brieu, J.-F. Witz, and A. Mbiakop-Ngassa, "Experimental investigation of elastomer mode I fracture: an attempt to estimate the critical strain energy release rate using SENT tests," *International Journal of Fracture*, vol. 209, no. 1-2, pp. 163 – 170, 2018. Publisher: Springer Verlag tex.hal_id: hal-01824808 tex.hal_version: v1.

[149] D. Roucou, J. Diani, M. Brieu, and A. Mbiakop-Ngassa, "Critical strain energy release rate for rubbers: single edge notch tension versus pure shear tests," *International Journal of Fracture*, vol. 216, pp. 31–39, Mar. 2019.

PERSONAL INFORMATION

Name and surname: Kemal Açıkgöz

Nationality: Turkish

Date of birth: 11.08.1988

Place of birth: Çorum

Marital status: Married

e-mail: kmlrsrch@gmail.com

EDUCATION

Degree	Institution	Year of Graduation
M.Sc.	Middle East Technical University	2015
B.Sc.	Balıkesir University	2010
High School	Çorum Anatolian High School	2006

EXPERIENCE

Years	Institution	Role
2010-present	Middle East Technical University	Research assistant

KEY PUBLICATIONS

[2] Dal, H., **Açıkgöz, K.**, & Badienia, Y. (2021). On the performance of isotropic hyperelastic constitutive models for rubber-like materials: A state of the art review. **Applied Mechanics Reviews**, 73(2).

[2] Dal, H., Gültekin, O., & **Açıkgöz, K.** (2020). An extended eight-chain model for hyperelastic and finite viscoelastic response of rubberlike materials: Theory, experiments and numerical aspects. **Journal of the Mechanics and Physics of Solids**, 145, 104159.

[3] Dal, H., Badienia, Y., **Açıkgöz, K.**, Aksu Denli, F. (2019). A comparative study on hyperelastic constitutive models on rubber: State of art after 2006. In book: Constitutive Models for Rubber XI.

[4]   Dal, H., Badienia, Y., & **Açıkgöz, K.**, Aksu Denli, F. (2017). Novel Parameter Identification Toolbox for the Selection of Hyperelastic Constitutive Models from Experimental Data, Proceedings of the 7th GACM Colloquium on Computational Mechanics for Young Scientists from Academia and Industry October 11-13, in Stuttgart, Germany.

[5]   **Açıkgöz, K.**, Hüsnü, D. (2022). A generalized phase-field approach for the failure of rubberlike materials, In book: Constitutive Models for Rubber XII.